By A.M.M.J. PIETERS

THE TUMOR MICROENVIRONMENT

A new perspective on the metastatic cascade and its therapeutic implications

THE TUMOR MICROENVIRONMENT;
A new perspective on the metastatic cascade and its therapeutic implications

Thesis, Faculty of Medicine, University Utrecht, the Netherlands, with summary in Dutch
Proefschrift, Medische faculteit, Universiteit Utrecht, Nederland, met een samenvatting in het Nederlands

The work described in this thesis was supported by personal grants from the US Department of Defense Breast Cancer Program, Stichting Jo Kolk Studiefonds, Stichting Prof. Michaël-van Vloten Fonds, onderzoeksbeurs van de Nederlandse Vereniging voor Heelkunde, Stichting van Oosterom Onderwijsfonds en de Stichting Fundatie van de Vrijvrouwe van Renswoude, onderzoeksbeurs.

Publication of this thesis was financially supported by: Afdeling Heelkunde UMC Utrecht, ChipSoft BV, Olympus Nederland BV

ISBN/EAN: 978-90-393-6251-8
Printed by: Gildeprint, Enschede

THE TUMOR MICROENVIRONMENT;

A NEW PERSPECTIVE ON THE METASTATIC CASCADE AND ITS THERAPEUTIC IMPLICATIONS

(met een samenvatting in het Nederlands)

PROEFSCHRIFT

ter verkrijging van de graad van doctor aan de Universiteit Utrecht
op gezag van de rector magnificus, prof dr. G.J. van der Zwaan,
ingevolge het besluit van het college voor promoties in het
openbaar te verdedigen op 7 januari 2015 des middags te 4.15

door

Annique Mathilde Maria Jeanne Pieters
geboren op 23 juli 1977 te Maastricht

Promotor: Prof. dr. I.H.M. Borel Rinkes

Copromotor: Dr. D.G. Duda

Aan Lieve en Britt

Content

PART I THE ROLE STROMAL CELLS IN TUMOR METASTASES

Chapter 1

General introduction and outline of the thesis

More than a hundred years ago, Stephen Paget hypothesized that metastatic cells – the seeds – only grow in secondary sites – the soil – with a permissive microenvironment [1]. Today we understand that the tumor's interplay with its environment, both at the primary and the metastatic sites, is of major importance [2-5]. This thesis provides novel insights into host-tumor interaction, unravels mechanisms of resistance to current therapies and offers potential targeting strategies to combat these mechanisms, for example in brain metastases from HER2-positive breast cancer.

Hematogenous metastasis: A highly complex and inefficient process

The majority of cancer patients ultimately succumb to metastatic disease. The process of cancer metastasis is viewed as a series of sequential, interrelated steps. Cancer cells must complete each and every one of these steps in order to successfully grow out in a distant organ [6-8]. Cancer is the result of accumulation of oncogenic events in normal cells that leads to malignant transformation. Malignant cells gain the ability to grow uncontrollably, and primary tumor growth is initiated. However, to grow beyond a size of 1-2 mm, microscopic tumors require new vessel formation for oxygen and nutrient supply. This neovascularization usually occurs as a result of tumor angiogenesis – sprouting from existing vasculature [9]. Next, *in situ* carcinomas become invasive by breaching through the basement membrane [10-12]. Thereafter, single cells or aggregates intravasate into blood microvessels, and are transported to distant organs. At these distant sites, tumor cells can actively home or become trapped in capillaries and then extravasate into the neighboring tissues [13]. Once again, cancer cell proliferation and neovascularization are critical for formation of micro– and then macroscopic metastatic nodules, which completes the process [9] Throughout their journey, the cancer cells need to evade destruction by host defense systems. It has been know for many years that this process is highly inefficient. The majority of tumor cells that are shed from the primary tumor are either destroyed within the circulation, are unable to extravasate or lack the ability to proliferate at the distant sites.

Stomal/Tumor crosstalk

For many decades, cancer research has been largely focused on cancer cells and their acquired genetic changes during the initial phases of tumor progression. These oncogenic events lead to the acquisition of constitutive mitogenic signals and the ability to resist growth-inhibiting signals, to avoid programmed cell death (apoptosis) and to induce blood-vessel growth (angiogenesis) [14]. By the end of last century, it became clear that local and distant tumor progression depend both on the cancer cell mutations as well as on the interactions with their environment. This shifted the view of cancer toward an understanding of tumors as organs, in which highly abnormal cancer cells grow in an elaborated extracellular matrix with the support of various types of host-derived stromal cells [4, 15]. Today researchers agree that these non-neoplastic cells stromal cells – which can account for more than 90% of the cells in some cancers, such as pancreatic ductal adenocarcinomas – are active and essential collaborators in tumor masses [16-18]. It has been accepted for many years that stromal cells are recruited by tumors from local tissue and from blood circulation and are then exploited by the tumor cells, but only recently it has become clear that these cells play an active and not just passive role in tumor growth [19, 20]. The localization and phenotype of tumor-associated fibroblasts, myofibroblasts and macrophages within carcinomas is an indication that tumor stroma is active (proliferation, differentiation) in parallel with the expansion of malignant epithelial cells during tumor growth [21]. Indeed, when experimentally co-implanted with cancer cells at a distant site in the form of heterotypic tumor fragments (chunks) from an original tumor source, the stromal cells proliferate and support the initial tumor growth at that site [22]. This leads to the hypothesis that stromal cells can increase the efficacy of cancer metastasis by interacting with tumor cells during the various steps of the metastatic cascade, including by co-travelling with cancer cells within circulating tumor fragments. Testing this hypothesis requires new and more sophisticated models.

Animal models of metastasis

The development of clinically relevant animal models is key to translational research. The majority of experiments studying tumor metastases are done in xenograft models, where metastatic tumor cells are implanted *in vivo* in either their orthotopic site or, subcutaneous from where they metastasize spontaneously. Alternatively, tumor cells are injected directly into the circulation and form metastases in the first organ where they mechanically get arrested, usually the lung or the liver. In order to study the role of host cells in the metastatic cascade, infusion models, where tumor cells are injected into the circulation as single cells, are not representative. Furthermore, for our studies, the use of traditional orthotopic models is ineffective since host cells are uniformly present in both the primary tumor location as well as in the distant site, and translocation of "passenger" stromal cells within metastatic nodules can not be traced. In order to detect and study these passenger stromal cells, we have set out to develop a set of three *in vivo* models that each mimic one of the steps in spontaneous metastases formation.

Tumor angiogenesis

Formation of new blood vessels plays a determinant role in tumor growth and progression [23]. Angiogenesis in physiological states – for example in embryonic and postnatal development, wound healing, and pregnancy – is a well-controlled process [24]. Expression of endogenous pro- and antiangiogenic factors is tightly regulated, resulting in fully functional vessels. In contrast, in cancer lesions there is a chronic overexpression of multiple proangiogenic growth factors – such as Vascular Endothelial Growth Factor A (VEGF-A/VEGF), basis Fibroblast Growth Factor (bFGF), and Placental Growth Factor (PlGF) – which is fueled by multiple factors such as oncogenic mutations or environmental factors (tumor hypoxia or low pH) [25, 26]. This overexpression results in new vessels that are immature and structurally and functionally abnormal, which along with cancer cell proliferation further increases hypoxia and acidosis [27]. Over the last 14 years, work from the Steele Lab has shown that antiangiogenic therapy can – at least transiently – 'normalize' these aberrant tumor vessels by restoring the balance between pro- and antiangiogenic factors. In turn, this results in improved drug delivery and

efficacy by reduction of interstitial fluid pressure and vessel leakiness, whilst improving oxygen availability within the tumor tissue [28, 29]. Building on this concept, antiangiogenic therapy would be an ideal addition to standard therapies like chemo- and radiation therapy. Multiple approaches using specific VEGF pathway blockers (bevacizumab, aflibercept, ramucirumab) in combination with standard therapy or using multi-targeted tyrosine kinase inhibitors with anti-VEGF receptor activity (sunitinib, sorafenib, vandetanib, pazopanib, cabozantinib) have proven their utility in the clinic, but the survival benefits remain small [30, 31].

Blood-brain barrier and drug delivery to brain metastases

The blood-brain-barrier (BBB) is a term used to describe the specific properties of blood vessels in the central nervous system [32, 33]. The BBB is a selective barrier between the systemic circulation and cerebrospinal fluid that constitutes of endothelial cells, pericytes and astrocytic perivascular endfeet. Tight junctions between these cells force molecules to pass through these cells instead of going around them [34]. The BBB regulates precise ionic concentrations required for proper neural function. Also, it protects the central nervous system (CNS) from injury and disease by restricting the entry of toxins, pathogens and the body's own immune system. Inadequate function of the BBB has been shown to be a critical component of edema, stroke and brain trauma, whereas an intact BBB is a major hurdle for drug delivery [35, 36]. One of the fields where the BBB might be a major obstacle for treatment is brain metastatic breast cancer.

Anti-HER2 targeted therapies for HER2+ breast cancer

Approximately 20-30% of human breast cancers express the Human epithelial growth factor receptor 2 (HER-2) [37, 38]. HER2-positive/amplified breast cancers are known for their high aggressiveness and tendency to metastasize, as well as decreased overall survival in these patients [39, 40]. HER2 is part of the ErbB family of receptor tyrosine kinases (RTKs), which includes HER1 (epidermal growth factor receptor [EGFR]), HER3, and HER4. Ligand-independent HER2-mediated signal transduction is thought to depend largely on heterodimerization with other family members [41]. In 1998, the monoclonal

anti-HER2 antibody trastuzumab (Herceptin®, Genentech, Brentford, UK) was approved for clinical use in both early stage and metastatic breast cancers that show overexpression/amplification of HER-2 [42]. This antibody targeted against the extracellular portion of HER2 shows significant benefit when combined with adjuvant chemotherapy [43]. In 2007, lapatinib (Tykerb®, GlaxoSmithKline, South San Francisco, USA), a small molecule dual HER2- and EGFR/HER1-specific tyrosine kinase inhibitor (TKI), was approved in combination with capecitabine for patients with advanced HER2+ breast cancers [44]. Despite these advances, approximately 15% of the treated women still develop metastatic disease after combination therapy [45, 46].

Trastuzumab binds to the HER-2 receptor and inhibits downstream signaling through the phosphatidylinositol-3-kinase (PI3K) and mitogen-activated protein kinase (MAPK) pathways, which results in inhibition of cellular proliferation [47, 48]. Trastuzumab also reduces Src activity by dephosphorylation and activation of PTEN leading to inhibition of Akt and mTOR signaling, resulting in reduced proliferation and enhanced apoptosis [49]. *In vivo* studies show that trastuzumab can indeed induce apoptosis in breast cancer cells. However, whether this effect is mediated by direct cytotoxicity or by indirect mechanisms, e.g., antiangiogenic activity or antibody-dependent cellular cytotoxicity (ADCC), is not well defined [50]. Indeed, in models of brain metastasis, treatment of HER2 overexpressing breast cancers with trastuzumab can inhibit angiogenesis by reducing the expression of proangiogenic factors (VEGF) as well as inducing the expression of antiangiogenic factors (Thrombospondin 1), resulting in normalization of the tumor vasculature [51]. Moreover, trastuzumab has shown to activate ADCC in breast cancers, which results in the lysis of cells to which it is bound [52-54].

With the development of lapatinib, a small molecule TKI for both EGFR and HER2 has emerged. Because of its potent and reversible inhibitor of the tyrosine kinase domains of both EGFR and HER2, lapatinib is classified as a dual TKI [55]. Lapatinib mimics ATP and binds to the ATP binding site at the tyrosine kinase domain. As a result, lapatinib blocks ATP from binding to the tyrosine kinase domain and inhibits the tyrosine kinase from using ATP as a cofactor for phosphorylation of tyrosine residues [56], leading to an increase of apoptosis and a decreased cellular proliferation [55, 57]. Despite this activity, the

efficacy of lapatinib, especially in brain metastatic breast cancer has been underwhelming (see below).

Targeting the Her2 pathway in breast to brain metastases

Over the last 15 years, HER2 inhibitors have proven their effects against systemic disease, but have failed to do so against intra-cranial metastases, which develop in up to 35 % of patients [58-63]. Molecularly targeted drugs, like trastuzumab and lapatinib have significantly benefited patients with metastatic breast cancer in combination with chemotherapy [42, 44, 64, 65]. However, the patients invariably develop, often very rapidly, resistance to these therapies and ultimately succumb to brain metastasis. Thus novel therapeutic approaches to prolong survival and/or at least increase the quality of life for metastatic breast cancer patients are desperately needed [66-68]. Unlike *HER2* amplified breast cancers in extracranial locations, brain metastases do not respond to trastuzumab [69]. This lack of response is generally attributed to the inability of trastuzumab to reach the brain lesions. However, the response to lapatinib, a low molecular weight drug, is also modest in brain metastasis despite its presumed ability to cross the BBB [44, 66, 67]. The effects of lapatinib on early brain metastases have been studied using a breast cancer cell line that ectopically over-expressed HER2 [70, 71]. While the results have been informative, this cell line was not "addicted" to oncogenic HER2 signaling and therefore, these studies ultimately did not reveal why HER2-amplified breast cancer brain metastases fail to respond to anti-HER2 therapies. The mechanism behind the differential response of brain metastases from HER2-amplified breast cancer to these agents remains unknown. In this thesis, we focuss on designing preclinical models to offer much needed insight into potential mechanisms of action of anti-HER2 based therapies of brain metastases, and to design novel strategies to more effectively treat these resistant cancers.

Tumors and vasogenic brain edema

In this thesis we also center on the interplay between tumors growing in the brain and their microenvironment. Specifically, we studied the role of brain vasogenic edema as a result of tumor growth. Edema develops as a result of both primary (glioma) and

metastatic tumor growth and is a major cause of morbidity and mortality. In this thesis, we studied the role of edema in orthotopic models of primary brain tumors (glioma). In adults, malignant glioma is the most common primary brain tumor accounting for 40% of all primary brain tumors. Prognosis is poor and 5 year survival rates of as low as <5% are reported [72]. The current standard of care for glioma is surgical resection, followed by radiotherapy and chemotherapy (temozolomide). Adjuvant therapies using temozolomide, an oral alkylating chemotherapy agent, followed by 6 – 12 monthly cycles of postradiation temozolomide, have only increased the median survival of patients with this tumor from 12 to 14.6 months [73]. Brain edema is often categorized as vasogenic or cytotoxic edema. Vasogenic edema occurs when the integrity of the normal vasculature of the blood-brain barrier is disrupted. As a result, fluid leaks out of the circulation into the intercellular space. The absence of lymphatic drainage in the brain impairs the resorption of this excess fluid. Vasogenic edema can either be generalized or localized, the latter being apparent in neoplastic disease. Cytotoxic edema is related to cellular injury, for example in hypoxic/ischemic insults. Brain edema can lead to elevated intracranial pressure – an increase in cerebral fluid pressure above 200 mm water with the patient in supine position. Most cases are associated with a mass effect, either diffuse, as in generalized brain edema, or focal as with tumors, abscesses or hemorrhages. If the expansion is severe, a herniation of the brain will occur.

Effects of antiangiogenic therapy on brain tumors

A recent phase II study of cediranib, a potent pan VEGF receptor TKI, in recurrent glioblastoma patients showed that antiangiogenic treatment can transiently normalize tumor vessels by causing rapid changes in tumor vessel structure and function and thus alleviating brain edema. In addition, cediranib reduced tumor-associated contrast enhancement to less than one half of the pretreatment value and reduced tumor bulk and mass effect in the majority of patients [74]. These encouraging findings have led to randomized phase II and III studies with anti-VEGF agents in combination with chemotherapy and as monotherapy [75, 76]. However, the underlying mechanisms responsible for these effects remain poorly understood. Although the anti-edema effects of VEGF-targeted therapy are widely accepted, its contribution to the survival benefit

remains unknown. Thus, these clinical data raise an important question: Is controlling tumor-associated edema by anti-VEGF agents sufficient to increase survival? In patients, this determination is difficult because MRI-based determinations of tumor progression are confounded by changes in vascular permeability after anti-VEGF therapy. In this thesis, we addressed this question using intravital microscopy, histology, molecular and cellular marker analyses, and functional MRI to investigate the effects of cediranib in brain tumor models in mice.

Outline and central questions in this thesis:

In the last decades it has become clear that tumor growth and metastatic dissemination of tumor cells is a complex interplay between neoplastic cells and the tumor microenvironment. As a result, research has transformed drastically by focusing not only on tumor cells, but also on the stromal compartment as well as the role of organ specific microenvironment and angiogenesis, and thereby, opening new possibilities for novel therapeutic strategies. The central goal of the work in this thesis is unraveling the role of microenvironment in primary tumors and their metastases. In the first section, this thesis focuses on the tumor stroma and its role in the various steps of the metastatic cascade. In the second section it will discuss therapies directed at the microenvironment in metastatic and primary brain tumors. The work presented in this thesis was guided by the following research questions:

Part one:

I Could we develop a set of animal models to model and study the individual steps of the metastatic cascade and track the stromal cells (Chapters 2-4)?

II Are stromal cell involved in all the steps of the metastatic cascade and how do they impact metastasis formation (Chapter 5)?

Part two:

III Does the blood-brain-barrier affect HER2-targeted therapies (Chapter 6)?

IV Does the addition of an antiangiogenic agent to anti-HER2 therapy improve treatment outcomes (chapter 6)?

V What mechanisms contribute to the improved antitumor effect of combination therapy (chapter 6)?

VI Can vascular normalization and edema alleviation in glioblastoma by antiangiogenic therapy improve outcomes (Chapter 7)?

VII Which structural and functional vascular changes induced by antiangiogenic therapy control edema (Chapter 7)?

One of the major obstacles in the field of metastasis has been the lack of representative animal models. In order to achieve the goals described in part one, we developed three novel *in vivo* metastasis models to study the role of stromal cells in various steps of hematogenous tumor metastasis. These models will enable researchers to assess the benefits of targeted therapies. First, we describe in **Chapter 2** a transient parabiosis model that can be used to detect fluorescent primary tumor-derived "passenger" stromal cells in the metastatic sites (*Nature Protocols* 2012a). Second, we report in **Chapter 3** a renal tumor perfusion model, developed to study the shedding pattern of tumor cells from primary lesions and their survival while in circulation (*Nature Protocols* 2012b). Third, we present in **Chapter 4** an animal model that could be used to evaluate the role of carcinoma-associated fibroblasts in tumor cell survival within the blood circulation and the outgrowth of micrometastases at the secondary sites (*Nature Protocols* 2012a). In **Chapter 5,** we will discuss the results of this work on elucidating the role of stromal cells in the metastatic process using these novel animal models (*PNAS* 2010). **Chapter 6** includes studies of brain metastases originating from HER2 positive breast carcinoma, and therapies targeting the Her2 pathway (*PNAS* 2012). **Chapter 7** includes our work on evaluation of treatment of primary brain tumors with angiogenic therapy (*Journal of Clinical Oncology* 2009). Finally in **chapter 8**, the main findings of the studies included in this thesis are summarized and the future directions discussed.

References

1. Paget S. The distribution of secondary growths in cancer of the breast. *Lancet.* 1889;1:571-573.

2. Condeelis J, Pollard JW. Macrophages: obligate partners for tumor cell migration, invasion, and metastasis. *Cell.* Jan 27 2006;124(2):263-266.

3. Fidler IJ. The pathogenesis of cancer metastasis: the 'seed and soil' hypothesis revisited. *Nat Rev Cancer.* Jun 2003;3(6):453-458.

4. Liotta LA, Kohn EC. The microenvironment of the tumour-host interface. *Nature.* May 17 2001;411(6835):375-379.

5. Duda DG, Ancukiewicz M, Isakoff SJ, Krop IE, Jain RK. Seeds and soil: unraveling the role of local tumor stroma in distant metastasis. *J Natl Cancer Inst.* Aug 2014;106(8).

6. Fidler IJ. Critical factors in the biology of human cancer metastasis: twenty-eighth G.H.A. Clowes memorial award lecture. *Cancer Res.* Oct 1 1990;50(19):6130-6138.

7. Talmadge JE, Fidler IJ. AACR centennial series: the biology of cancer metastasis: historical perspective. *Cancer Res.* Jul 15 2010;70(14):5649-5669.

8. Hanahan D, Weinberg RA. The hallmarks of cancer. *Cell.* Jan 7 2000;100(1):57-70.

9. Folkman J. How is blood vessel growth regulated in normal and neoplastic tissue? G.H.A. Clowes memorial Award lecture. *Cancer Res.* Feb 1986;46(2):467-473.

10. Liotta LA. Tumor invasion and metastases--role of the extracellular matrix: Rhoads Memorial Award lecture. *Cancer Res.* Jan 1986;46(1):1-7.

11. Fisher B, Fisher ER. The interrelationship of hematogenous and lymphatic tumor cell dissemination. *Surg Gynecol Obstet.* Apr 1966;122(4):791-798.

12. Fisher ER, Fisher B. Recent observations on concepts of metastasis. *Arch Pathol.* Apr 1967;83(4):321-324.

13. Nicolson GL. Cancer metastasis: tumor cell and host organ properties important in metastasis to specific secondary sites. *Biochim Biophys Acta.* Nov 15 1988;948(2):175-224.

14. Bernards R, Weinberg RA. A progression puzzle. *Nature.* Aug 22 2002;418(6900):823.

15. Ruiter DJ, van Krieken JH, van Muijen GN, de Waal RM. Tumour metastasis: is tissue an issue? *Lancet Oncol.* Feb 2001;2(2):109-112.

16. Gupta A, Deshpande CG, Badve S. Role of E-cadherins in development of lymphatic tumor emboli. *Cancer.* May 1 2003;97(9):2341-2347.

17. Ohno S, Tachibana M, Fujii T, Ueda S, Kubota H, Nagasue N. Role of stromal collagen in immunomodulation and prognosis of advanced gastric carcinoma. *Int J Cancer.* Feb 20 2002;97(6):770-774.

18. Wang-Rodriguez J, Dreilinger AD, Alsharabi GM, Rearden A. The signaling adapter protein PINCH is up-regulated in the stroma of common cancers, notably at invasive edges. *Cancer.* Sep 15 2002;95(6):1387-1395.

19. Bhowmick NA, Neilson EG, Moses HL. Stromal fibroblasts in cancer initiation and progression. *Nature.* Nov 18 2004;432(7015):332-337.

20. Elenbaas B, Weinberg RA. Heterotypic signaling between epithelial tumor cells and fibroblasts in carcinoma formation. *Experimental Cell Research.* Mar 10 2001;264(1):169-184.

21. Bingle L, Brown NJ, Lewis CE. The role of tumour-associated macrophages in tumour progression: implications for new anticancer therapies. *J Pathol.* Mar 2002;196(3):254-265.

22. Duda DG, Fukumura D, Munn LL, et al. Differential transplantability of tumor-associated stromal cells. *Cancer Res.* Sep 1 2004;64(17):5920-5924.

23. Folkman J. Tumor angiogenesis: therapeutic implications. *N Engl J Med.* Nov 18 1971;285(21):1182-1186.

24. Carmeliet P. Mechanisms of angiogenesis and arteriogenesis. *Nature Medicine.* Apr 2000;6(4):389-395.

25. Carmeliet P, Jain RK. Angiogenesis in cancer and other diseases. *Nature.* Sep 14 2000;407(6801):249-257.

26. Jain RK. Molecular regulation of vessel maturation. *Nat Med.* Jun 2003;9(6):685-693.

27. Hanahan D, Folkman J. Patterns and emerging mechanisms of the angiogenic switch during tumorigenesis. *Cell.* Aug 9 1996;86(3):353-364.

28. Jain RK. Normalizing tumor vasculature with anti-angiogenic therapy: a new paradigm for combination therapy. *Nat Med.* Sep 2001;7(9):987-989.

29. Jain RK. Normalization of tumor vasculature: an emerging concept in antiangiogenic therapy. *Science.* Jan 7 2005;307(5706):58-62.

30. Jain RK, Duda DG, Clark JW, Loeffler JS. Lessons from phase III clinical trials on anti-VEGF therapy for cancer. *Nat Clin Pract Oncol.* Jan 2006;3(1):24-40.

31. Jain RK. Normalizing tumor microenvironment to treat cancer: bench to bedside to biomarkers. *J Clin Oncol.* Jun 10 2013;31(17):2205-2218.

32. Gloor SM, Wachtel M, Bolliger MF, Ishihara H, Landmann R, Frei K. Molecular and cellular permeability control at the blood-brain barrier. *Brain Res Brain Res Rev.* Oct 2001;36(2-3):258-264.

33. Rubin LL, Staddon JM. The cell biology of the blood-brain barrier. *Annu Rev Neurosci.* 1999;22:11-28.

34. Abbott NJ, Ronnback L, Hansson E. Astrocyte-endothelial interactions at the blood-brain barrier. *Nat Rev Neurosci.* Jan 2006;7(1):41-53.

35. Alvarez JI, Cayrol R, Prat A. Disruption of central nervous system barriers in multiple sclerosis. *Biochim Biophys Acta.* Feb 2011;1812(2):252-264.

36. Sandoval KE, Witt KA. Blood-brain barrier tight junction permeability and ischemic stroke. *Neurobiol Dis.* Nov 2008;32(2):200-219.

37. Perou CM, Sorlie T, Eisen MB, et al. Molecular portraits of human breast tumours. *Nature.* Aug 17 2000;406(6797):747-752.

38. Sorlie T, Perou CM, Tibshirani R, et al. Gene expression patterns of breast carcinomas distinguish tumor subclasses with clinical implications. *Proc Natl Acad Sci U S A.* Sep 11 2001;98(19):10869-10874.

39. Slamon DJ, Clark GM, Wong SG, Levin WJ, Ullrich A, McGuire WL. Human breast cancer: correlation of relapse and survival with amplification of the HER-2/neu oncogene. *Science.* Jan 9 1987;235(4785):177-182.

40. Slamon DJ, Godolphin W, Jones LA, et al. Studies of the HER-2/neu proto-oncogene in human breast and ovarian cancer. *Science.* May 12 1989;244(4905):707-712.

41. Yarden Y, Sliwkowski MX. Untangling the ErbB signalling network. *Nat Rev Mol Cell Biol.* Feb 2001;2(2):127-137.

42. Slamon DJ, Leyland-Jones B, Shak S, et al. Use of chemotherapy plus a monoclonal antibody against HER2 for metastatic breast cancer that overexpresses HER2. *N Engl J Med.* Mar 15 2001;344(11):783-792.

43. Romond EH, Perez EA, Bryant J, et al. Trastuzumab plus adjuvant chemotherapy for operable HER2-positive breast cancer. *N Engl J Med.* Oct 20 2005;353(16):1673-1684.

44. Geyer CE, Forster J, Lindquist D, et al. Lapatinib plus capecitabine for HER2-positive advanced breast cancer. *N Engl J Med.* Dec 28 2006;355(26):2733-2743.

45. Nahta R, Esteva FJ. Herceptin: mechanisms of action and resistance. *Cancer Lett.* Feb 8 2006;232(2):123-138.

46. Nahta R, Yu D, Hung MC, Hortobagyi GN, Esteva FJ. Mechanisms of disease: understanding resistance to HER2-targeted therapy in human breast cancer. *Nat Clin Pract Oncol.* May 2006;3(5):269-280.

47. Baselga J, Albanell J, Molina MA, Arribas J. Mechanism of action of trastuzumab and scientific update. *Semin Oncol.* Oct 2001;28(5 Suppl 16):4-11.

48. Sliwkowski MX, Lofgren JA, Lewis GD, Hotaling TE, Fendly BM, Fox JA. Nonclinical studies addressing the mechanism of action of trastuzumab (Herceptin). *Semin Oncol.* Aug 1999;26(4 Suppl 12):60-70.

49. Nagata Y, Lan KH, Zhou X, et al. PTEN activation contributes to tumor inhibition by trastuzumab, and loss of PTEN predicts trastuzumab resistance in patients. *Cancer Cell.* Aug 2004;6(2):117-127.

50. Gennari R, Menard S, Fagnoni F, et al. Pilot study of the mechanism of action of preoperative trastuzumab in patients with primary operable breast tumors overexpressing HER2. *Clin Cancer Res.* Sep 1 2004;10(17):5650-5655.

51. Izumi Y, Xu L, di Tomaso E, Fukumura D, Jain RK. Tumour biology: herceptin acts as an anti-angiogenic cocktail. *Nature.* Mar 21 2002;416(6878):279-280.

52. Carter P, Presta L, Gorman CM, et al. Humanization of an anti-p185HER2 antibody for human cancer therapy. *Proc Natl Acad Sci U S A.* May 15 1992;89(10):4285-4289.

53. Cooley S, Burns LJ, Repka T, Miller JS. Natural killer cell cytotoxicity of breast cancer targets is enhanced by two distinct mechanisms of antibody-dependent cellular cytotoxicity against LFA-3 and HER2/neu. *Exp Hematol.* Oct 1999;27(10):1533-1541.

54. Lewis GD, Figari I, Fendly B, et al. Differential responses of human tumor cell lines to anti-p185HER2 monoclonal antibodies. *Cancer Immunol Immunother.* Sep 1993;37(4):255-263.

55. Xia W, Mullin RJ, Keith BR, et al. Anti-tumor activity of GW572016: a dual tyrosine kinase inhibitor blocks EGF activation of EGFR/erbB2 and downstream Erk1/2 and AKT pathways. *Oncogene.* Sep 12 2002;21(41):6255-6263.

56. Nelson MH, Dolder CR. Lapatinib: a novel dual tyrosine kinase inhibitor with activity in solid tumors. *Ann Pharmacother.* Feb 2006;40(2):261-269.

57. Medina PJ, Goodin S. Lapatinib: a dual inhibitor of human epidermal growth factor receptor tyrosine kinases. *Clin Ther.* Aug 2008;30(8):1426-1447.

58. Brufsky AM, Mayer M, Rugo HS, et al. Central nervous system metastases in patients with HER2-positive metastatic breast cancer: incidence, treatment, and survival in patients from registHER. *Clin Cancer Res.* Jul 15 2011;17(14):4834-4843.

59. Le XF, Mao W, Lu C, et al. Specific blockade of VEGF and HER2 pathways results in greater growth inhibition of breast cancer xenografts that overexpress HER2. *Cell Cycle.* Dec 2008;7(23):3747-3758.

60. Leyland-Jones B. Human epidermal growth factor receptor 2-positive breast cancer and central nervous system metastases. *J Clin Oncol.* Nov 1 2009;27(31):5278-5286.

61. Pestalozzi B. Trastuzumab does not increase the incidence of central nervous system (CNS) relapses in HER2-positive early breast cancer: the HERA trial experience. *Cancer Research.* 2011;71(24, Suppl 3):P4-17-01.

62. Kirsch DG, Loeffler JS. Brain metastases in patients with breast cancer: new horizons. *Clin Breast Cancer.* Jun 2005;6(2):115-124.

63. Patchell RA. The management of brain metastases. *Cancer Treat Rev.* Dec 2003;29(6):533-540.

64. Nielsen DL, Andersson M, Kamby C. HER2-targeted therapy in breast cancer. Monoclonal antibodies and tyrosine kinase inhibitors. *Cancer Treat Rev.* Apr 2009;35(2):121-136.

65. Cameron D, Casey M, Oliva C, Newstat B, Imwalle B, Geyer CE. Lapatinib plus capecitabine in women with HER-2-positive advanced breast cancer: final survival analysis of a phase III randomized trial. *Oncologist.* 2010;15(9):924-934.

66. Lin NU, Carey LA, Liu MC, et al. Phase II trial of lapatinib for brain metastases in patients with human epidermal growth factor receptor 2-positive breast cancer. *J Clin Oncol.* Apr 20 2008;26(12):1993-1999.

67. Lin NU, Dieras V, Paul D, et al. Multicenter phase II study of lapatinib in patients with brain metastases from HER2-positive breast cancer. *Clin Cancer Res.* Feb 15 2009;15(4):1452-1459.

68. Lin NU, Winer EP. Brain metastases: the HER2 paradigm. *Clin Cancer Res.* Mar 15 2007;13(6):1648-1655.

69. Stemmler HJ, Kahlert S, Siekiera W, Untch M, Heinrich B, Heinemann V. Characteristics of patients with brain metastases receiving trastuzumab for HER2 overexpressing metastatic breast cancer. *Breast.* Apr 2006;15(2):219-225.

70. Gril B, Palmieri D, Bronder JL, et al. Effect of lapatinib on the outgrowth of metastatic breast cancer cells to the brain. *J Natl Cancer Inst.* Aug 6 2008;100(15):1092-1103.

71. Palmieri D, Bronder JL, Herring JM, et al. Her-2 overexpression increases the metastatic outgrowth of breast cancer cells in the brain. *Cancer Res.* May 1 2007;67(9):4190-4198.

72. Clarke J, Butowski N, Chang S. Recent advances in therapy for glioblastoma. *Arch Neurol.* Mar 2010;67(3):279-283.

73. Stupp R, Mason WP, van den Bent MJ, et al. Radiotherapy plus concomitant and adjuvant temozolomide for glioblastoma. *N Engl J Med.* Mar 10 2005;352(10):987-996.

74. Batchelor TT, Sorensen AG, di Tomaso E, et al. AZD2171, a pan-VEGF receptor tyrosine kinase inhibitor, normalizes tumor vasculature and alleviates edema in glioblastoma patients. *Cancer Cell.* Jan 2007;11(1):83-95.

75. Gilbert M. Phase III double‐blind placebo‐controlled trial evaluating bevacizumab in patients with newly diagnosed glioblastoma. *2013 ASCO Annual Meeting; 2013; Chicago.* 2013.

76. Rahmathulla G, Hovey EJ, Hashemi-Sadraei N, Ahluwalia MS. Bevacizumab in high-grade gliomas: a review of its uses, toxicity assessment, and future treatment challenges. *Onco Targets Ther.* 2013;6:371-389.

Chapter 2

A transient parabiosis skin transplant model in mice

Annique MMJ Duyverman
Mitsutomo Kohno
Dan G Duda
Rakesh K Jain
Dai Fukumura

Edwin L. Steele Laboratory for tumor Biology, Department of Radiation Oncology, Massachusetts General Hospital and Harvard Medical School, Boston, USA

Nature Protocols 2012; Vol 7, No 4: p 763-770

Abstract

Parabiosis—conjoined surgery to provide a shared circulation between two mice—has been previously developed to study the hematopoietic system. this protocol describes the use of parabiosis for efficient transplantation of skin from a transgenic to a wild-type mouse. It can be used to study the role of stromal cells in a spontaneous model of distant cancer dissemination (metastasis). We have recently shown that primary tumor-derived stromal cells may facilitate metastasis by providing a provisional stroma at the secondary site. studying the role of primary tumor–derived stroma cells requires methods for distinguishing and targeting stromal cells originating from the primary tumor versus their counterparts in the metastatic site. parabiosis may also be used, taking advantage of the shared circulation between the parabiosed mice, to study tumor metastasis from one parabiont to another, or to investigate the role of circulating inflammatory cells or stem cells. Studying the role of stromal cells in metastasis using this model typically takes up to 11 weeks

Introduction

Recent reports provide strong evidence for the contribution of nonmalignant stromal cells to the development of tumors[1-5]. Tumors actively recruit stromal cells and these cells facilitate tumor growth[6-10]. A metastatic cancer cell can only grow out to be an established metastasis when it successfully completes each of the sequential and interrelated steps of the metastatic cascade. Each of these steps can be rate limiting, and the failure to complete a step can abrogate the entire process[11].

Host-derived nonmalignant stroma may increase the efficiency of this complex system[12, 13]. Metastatic cells can reside in the lungs awaiting oncogenic activation[14], or they can home to pre-existing 'niches' created by inflammation and immune cell or fibrocyte accumulation[15-18]. In addition, it has been shown that metastatic cells can proliferate intravascularly before extravasation into the lung tissue[19]. Cancer cell clumping and embolus formation in blood circulation may increase metastasis[11, 20-23]. However, the clumps may also be fragments consisting of cancer cells and 'passenger' stromal cells carried over from the primary site.

The parabiosis model, in which two mice share the same circulation, may be used for a variety of studies of metastasis, such as tumor metastasis from one parabiont to another, or the role of circulating inflammatory cells or stem cells in the process[11, 24]. However, previous parabiosis models were not ideal for the study of metastasis by large tumor–stromal cell clumps. Therefore, we have recently developed the transient parabiosis technique described in this protocol in which a large skin flap is transplanted. We have found that the host-derived cells increase cancer cell viability in circulation; they also serve as a provisional stroma in the secondary site and increase cancer's metastatic efficiency[13].

Overview of the technique

Previously, it has been shown that GFP and RFP (dsRed) could be used to color-code tumor and stroma in vivo[25, 26]. This protocol describes an experiment for studying the involvement of stromal cells in a spontaneous metastasis formation model. The experimental design is depicted in Figure 1. In the parabiosis skin transplant model, we first generate a mouse chimera by reconstituting the
bone marrow of GFP-expressing Actb-GFP/C57BL/6 mice with nonfluorescent (wild-type (WT)) bone marrow cells from C57BL/6 mice. This is necessary to exclude from the analysis GFP + hematopoietic cells, which may be in the blood circulation during parabiosis. To this end, Actb-GFP/C57BL/6 mice are lethally irradiated using a dose of 12 Gy to the whole body in two fractions of 6 Gy 24 h apart. Then, the mice are rescued with a bone marrow transplant (BMT) from a nontransgenic (WT-C57BL/6) mouse. After 1 or 2 months, the reconstitution of the bone marrow is confirmed with flow cytometric analysis (i.e., chimerism of over 95%), using cells from non-GFP mice as controls. Next, the BMT-WT-ActbGFP and WT-C57BL/6 mice are parabiosed. The parabionts are conjoined for 3 weeks to establish a shared circulation and to ensure blood supply of the transplant from the recipient. Upon surgical separation, the large Actb-GFP skin transplant in WT mice is left to heal for 1–2 weeks before the implantation of red fluorescence-labeled tumor cells. The cancer cells in the transplanted Actb-GFP skin will generate primary tumors with GFP + host-derived cells. Two to three weeks later, the GFP + passenger stromal cells can be visualized in the lungs via multiphoton or confocal microscopy. Lung tissues from mice bearing non-GFP-labeled tumors are used as control

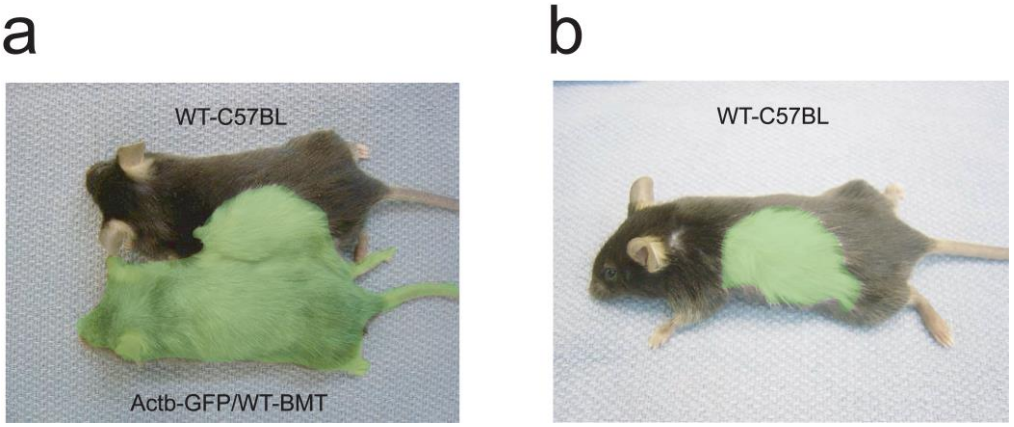

Figure 1 | Design of the experiment. (a) Transient parabiosis between a GFP-transgenic mouse and a WT mouse to ensure vascularization of a large skin transplant onto the recipient mouse. (b) A large GFP + skin transplant is created after separation of the parabionts. When tumors are grown in the transplant, GFP + stromal cells will be recruited, which can be visualized during spontaneous metastases. Reproduced with permission from ref. 13. All animal procedures were performed according to the guidelines of public health service policy on humane care of laboratory animals and in accordance with an approved protocol by the Institutional Animal Care and Use Committee of MGH.

Comparison with other techniques

Several in vitro assays have been developed to study host–tumor cell interactions related to progression and invasion, including two complementary protocols from our group[27-30]. As an alternative to growing primary tumors in previously transplanted Actb-GFP skin, one can use transplantation of tumor fragments that were originally grown in an Actb-GFP expressing mouse. In this tumor fragment graft model, tumor cells are first implanted subcutaneously in Actb-GFP–expressing mice and allowed to grow to a size of 6 mm in diameter. Then tumors are collected, fragmented into 1 × 1 mm pieces, and subsequently implanted in syngeneic WT (nontransgenic) recipient mice[31]. The advantage of this technique is the lack of circulating cell contamination in the model. The primary limitation of this technique is the discrepancy of doubling times between cancer and stromal cells, which results in rapid tumor growth with recruitment of mouse (nonfluorescent) stromal cells and depletion over time of the original GFP + stromal cells

from the transplanted fragment. This limits the ability to study the stromal cells during metastasis using GFP as a marker.

Selecting the appropriate experiment(s) for studying metastasizing stromal cells

We developed this spontaneous metastatic model to visualize passenger stromal cells that originate from the primary tumor in metastatic nodules. We have used this model—together with an isolated tumor perfusion model and a spontaneous metastases model where we can selectively deplete carcinoma-associated fibroblasts[29, 30]—to unravel the role of passenger fibroblasts in tumor metastasis to the lungs[13].

In order to select the appropriate technique for future studies, one should carefully consider which step of the metastatic process is of interest. Using the isolated tumor perfusion model, one could study tumor shedding and quantify the result of treatments or genetic manipulation in this specific step of metastasis[29]. The parabiosis skin transplantation model described here mimics the steps of spontaneous metastases from tumor shedding up to the outgrowth of micrometastases, taking advantage of the fluorescent labeling of the passenger stromal cells. Last, to facilitate depletion of the stromal compartment of the tumor microenvironment without affecting other organs, we developed a model of selective depletion of human carcinoma-associated fibroblasts[30].

The key advantage of this protocol over other existing methods is that one gains the ability to image in vivo the passenger stromal cells during various steps of metastasis by using fluorescent tumor stroma in a nontransgenic mouse. One limitation is that many of the current examples are ectopic tumor metastasis models. Another limitation is that the main focus is on mesenchymal stromal cells (over immune cells, e.g., monocyte/macrophages, which are largely excluded from analysis in the BMT model).

List of applications of the parabiosis skin transplantation model for metastasis

The parabiosis model can be used to generate a large skin transplant from a syngeneic donor that can be genetically different from the recipient. Possible modifications could be knockdown or overexpression of certain genes, or gender mismatch. In this protocol, we

focus on the role of stromal cells in metastases; however, other tumor stromal cells could potentially be studied using this protocol.

Materials

CRITICAL All reagents and equipment could be substituted with appropriate alternatives from other manufacturers.

REAGENTS

- PBS (1×; Cellgro, cat. no. 20-031-CV)
- Buprenorphine hydrochloride (0.3 mg ml − 1; MGH Pharmacy, cat. no. 716510) *caution:* It is poisonous and may cause prolonged respiratory depression. Wear protective clothing to avoid contact or inhalation. Buprenorphine is a controlled substance and should be handled according to institutional guidelines.
- Ethanol (70% (vol/vol); Pharmco, cat. no. 111000190)
- Fatal-Plus (Vortech, cat. no. NDC 298-9373-68) *caution* Fatal-Plus is a poisonous agent; caution should be exercised to avoid contact of the drug with open wounds or accidental self-inflicted injections.
- Fluorescent-labeled LLC1 cells (e.g., DsRed-labeled cells; ATTC, cat. no. CRL-1642)
- Hank's balanced salt solution (1×; Gibco, cat. no. 14170)
- Heparin sodium (1,000 USP U ml − 1; APP Pharmaceuticals, cat. no. 504011)
- Ketamine (100 mg ml − 1; Massachusetts General Hospital pharmacy) and Xylazine (10 mg ml − 1; Webster, cat. no. 200204.00) mixture per kg body weight
- Mice, Actb-GFP/C75BL/6, C57BL/6, 10 weeks of age. *caution* All animal studies must be reviewed and approved by the institutional animal care and use committees and conform all relevant ethics regulations
  critical All experiments must be performed under sterile conditions. Researchers should wear sterile hats, gowns and gloves.
- OCT compound (Allegiance, cat. no. M7148-4)
- Paraformaldehyde (10% (wt/vol); Polyscience, cat. no. 4018)

caution Hazardous when exposed to skin, inhaled or swallowed. Preparation of 4% (wt/vol) paraformaldehyde should be carried out in a chemical hood with appropriate clothing.

- dH2O

EQUIPMENT

- 5-0 Vicryl sutures (Ethicon, cat. no. X698G)
- Applicator tips (Owens minor, cat. no. 5937-W0D1002)
- Autoclip applier (plus 9-mm autoclips; Roboz Surgical Instruments, cat. no. RS-9260 + RS-9262)
- Caliper (Roboz Surgical Instruments, cat. no. RS-6466)
- Clipper (Webster, cat. no. 78997-010)
- Cryomolds (Cardinal Health, cat. no. M7144-13)
- Cryostat (Microm, cat. no. HM-560)
- Fluorescence microscope (Cambridge Research and Instrumentation)
- Forceps (Roboz Surgical Instruments, cat. nos. RS-5153, RS 5150, RS-5132)
- Heating pad (Shore Line, cat. no. 712.0000.04)
- Needle holder (14 cm; Roboz Surgical Instruments, cat. no. RS-6412)
- Permanent marker (Staedtler, cat. no. 342-9)
- Scissors (Roboz Surgical Instruments, cat. nos. RS-5840, RS-5883)
- Syringe (1 ml with a 26-G needle for anesthesia, 16-G and 30-G needles for BMT; Fisher Scientific, cat. no. 14-823-2E)
- Cotton swabs
- Blade and blade holder
- Cell strainer

REAGENT SETUP

Paraformaldehyde 4% (wt/vol): Add 180 ml of 1× PBS to 120 ml of 10% (wt/vol) formaldehyde. *Critical* This reagent has a short shelf life (< 1 week) so it must be freshly made on the day of use.
Buprenorphine, hydrochloride: Dissolve 1 ml of the 0.3 mg ml − 1 stock solution in 30 ml of 0.9% (wt/vol) sodium chloride. Store at 20 °C for up to 3 months. PBS (1×) Add 100 ml of 10× PBS to 900 ml of dH2O. Store at 20 °C for up to 9 months.
Ethanol 70% (vol/vol): Mix 1.7 liters of dH2O and 1 gallon of 100% ethanol. Store at 20 °C in a closed container.
Heparin: dilute 0.3 ml of heparin stock solution in 30 ml of 0.9% (wt/vol) sodium chloride. *Critical* Freshly prepare for each experiment.

Procedures

Bone marrow transplantation

1| Calculate the necessary number of mice for the experiment. Lethally irradiate the mice using 12 Gy in two fractions. Start on day 1 with a dose of 6 Gy to the whole body of Actb-GFP/C57BL/6 mice.
Critical step: During parabiosis, the donor and recipient share a common circulation. To prevent GFP + circulating hematopoietic cells from the donor from confounding the results after separation of the parabionts, the donor must receive a WT BMT at least 4 weeks before conjoining.

2| On the next day, repeat the whole-body irradiation as in Step 1.

3| On the next day (i.e., 1 day after second fraction of radiation), collect bone marrow from the femurs of WT-C57BL/6. Euthanize mice by injecting 0.1 ml of Fatal-Plus intra-abdominally. Dissect skin and muscles from the femurs (hind limbs) of the mouse, and cut off the joints using a blade and blade holder. Wash the bone marrow out of each bone by flushing them with 3 ml of 4% (vol/vol) heparin/PBS solution using a 30-G needle, and

collect the marrow in 15-ml tubes kept on ice. Centrifuge the bone marrow cells for 3 min at 500g at 4 °C, and then remove the supernatant. Resuspend the bone marrow cell pellet obtained from one mouse (two femurs) in 600 ∝l of PBS by using a 16-G needle and filtering through a 70-∝m cell strainer. Infuse 150 ∝l of bone marrow into the tail vein of the recipient Actb-GFP/C57BL/6 mouse of at least 8 weeks of age (i.e., the bone marrow cells from one mouse could be used to transplant three lethally irradiated mice).
critical step: Do not crush the bone when cutting off the ends, as it makes bone marrow flushing difficult.

Critical step Keep bone marrow cells on ice at all times before transplantation.

4| Wait 4 weeks for the bone marrow to engraft before proceeding to the next steps, while keeping mice in regular cages under sterile conditions.

5| Anesthetize both mice using 0.4 ml of ketamine/xylazine and a 30-G syringe.

Critical step: To make sure they wake up at the same time, it is important to anesthetize mice at the same time with the same amount of anesthetic.

6| Use a clipper to shave the entire right flank of the donor mouse and left flank of the recipient and clean their skin using 70% (vol/vol) ethanol.

7| Mark the incision line on the skin of the mouse using permanent marker. This should be half an ellipse starting from behind the ear to a point 1 cm anterior-lateral to the tail.

For the Actb-GFP/C57BL/6 skin donor, this line should be on the right flank of the animal going from the ear to the ventral side. For the WT recipient, the incision line should be on the left flank going from behind the ear toward the back of the mouse and the tail (Fig. 2a).

Critical step: It is important that both incision lines are of the same length and shape.

Parabiosis surgery

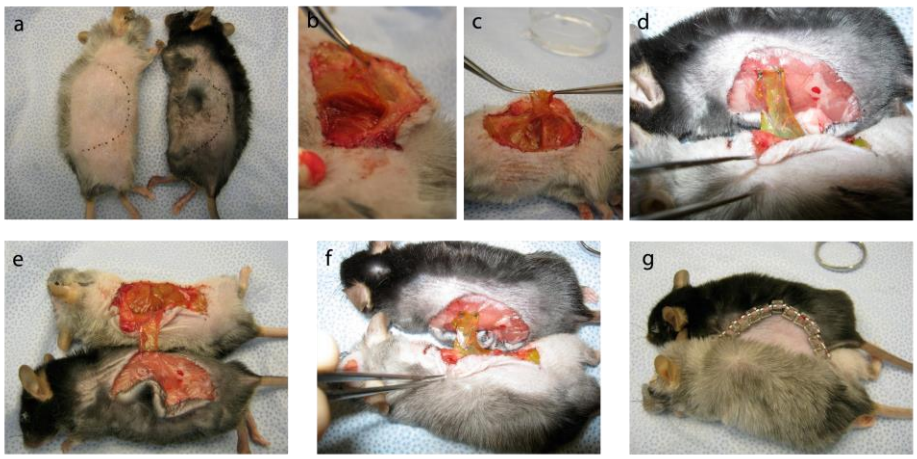

Figure 2 | GFP + skin transplantation through parabiosis surgery under general anesthesia. (a–g) The fur is shaved and the size of the transplant marked on the skin (a); a muscle flap is dissected from the thoracic cage and the peritoneum using a cotton swab (b); a 1–2 cm muscle flap (c,d) of the muscle flap is attached onto the non-GFP mouse with two sutures, and the pair of mice is turned onto their backs to apply two more sutures ~1 cm apart from the first set (e); a 1 cm2 of GFP + muscle is positioned on the non-transgenic mouse to ensure the development of a shared circulation (f); and the skin is closed with wound clips to finalize the parabiosis surgery (g). All animal procedures were performed according to the guidelines of public health service policy on humane care of laboratory animals and in accordance with an approved protocol by the Institutional Animal Care and Use Committee of MGH.

8| Make a skin incision along the incision line in the donor using forceps and scissors. Dissect skin and fat tissue from underlying muscles.

Critical step: Do not cut the right brachial artery, as this will cause massive bleeding.

9| Use forceps to lift the muscle from the thoracic ribs and dissect a muscle layer with small scissors and cotton swabs. Cut the intercostal muscles. Work from the ventral to the dorsal side and from anterior to posterior (Fig. 2b).

10| After dissecting the muscle from the thoracic wall, continue separating toward the tail. Use cotton swabs to separate the muscle from the peritoneum and use scissors to cut the ventral edges of the muscle layer. Create a muscle flap of about 2–3 cm in size that folds to the back of the mouse (Fig. 2c).

Critical step: The muscle layer and peritoneum join in the ventral midline. To avoid damaging the peritoneum, dissect up to 3 mm from the ventral line.

11| Move to the recipient mouse and make a skin incision along the incision line. Dissect the skin from the underlying muscle.

12| Position the mice next to each other with their heads facing down in the same direction. Use forceps, a needle holder and sutures to position the donor's muscle flap on the intact muscle of the recipient mouse. Make two mattress stitches on the lateral edges of the far end of the muscle flap (Fig. 2d).

13| Position the pair of mice on their backs and secure the muscle transplant with two more stitches as proximal to the donor as possible (Fig. 2e). This will create a fixed overlay of 1 cm2 of muscle tissue to ensure development of a shared circulation (Fig. 2f).

14| Close the skin by positioning the donor skin onto the back of the recipient mouse with wound clips (Fig. 2g). When finished, turn the pair and close the ventral skin. Use 5.0 Vicryl sutures to close the corners in the ear and tail areas. The mice should look similar to those in Figure 1a.

15| Administer 0.2 ml of buprenorphine and house every pair of mice individually in a special cage with easy water and food access.

16| Remove half of the wound clips (alternating, i.e., every other clip) after 1 week.

17| Remove the remaining wound clips after 2 weeks.

Separation of parabionts (3 weeks after initial conjoinment)

18| Three weeks after initial conjoinment, anesthetize the mice with ketamine/xylazine.

19| Cut the donor skin and subcutaneous tissues so that a large skin transplant (2–3 cm) is created from the Actb-GFP/ C57BL/6 donor mouse to be included in the skin of the WT mouse (see Fig. 1b for an example of the final appearance). Close the wound edges with wound clips. After separation, euthanize the donor mouse by cervical dislocation or by injecting 0.1 ml of Fatal-Plus intraperitoneally with a 30-G needle. House the transplanted mouse under pathogen-free conditions and allow the wound to heal (~1 week).

Tumor inoculation and resection

20| Anesthetize mice and inject 5×10^5 (fluorescence-labeled) metastatic cells suspended in 100 μl of Hank's buffered salt solution in the middle of the skin transplant.

21| Monitor the tumor size daily by caliper measurement. When the tumor diameter reaches 10 mm, resect the primary tumor and close the wound with wound clips.

Tissue collect and processing

22| After 3 weeks, or once metastases have formed, euthanize the mice by injecting 0.1 ml of Fatal-Plus intra-abdominally and collect the lungs or other target organs for metastases if you are using a different cell line (e.g., liver).

23| Fix the lungs in 4% (wt/vol) paraformaldehyde for 6 h, wash them with PBS, and then dehydrate them in 30% (wt/vol) sucrose overnight.

Critical step: Do not overfix the tissue as this may cause difficulties for immunohistochemical analyses.

24| Fill appropriate sized molds with OCT, embed collected tissues and store at −80 °C.

Pause point: Collected tissues can be sectioned and stained at any time. OCT-embedded blocks can be stored at – 80 °C for over a year.

25| Use cryostat to cut 20 μm tissue sections. Use standard antibody and counterstaining protocols to further analyze the tissue using a fluorescent microscope.

Troubleshooting advice can be found in table 1.

TABLE 1 | Troubleshooting table.

Step	Problem	Possible reason	Solution
1	Death of the mouse seconds after infusion of the bone marrow	Pulmonary embolism	Repeat the procedure after carefully filtering the bone marrow cell suspension. Inject slowly (over 1–2 min)
2	Mouse is not fully anesthetized	Dose is insufficient	Different strains of mice may have disparate sensitivities to a particular anesthesia. The dose prescribed in the protocol generally provides a safe and appropriate response; however, this dose may not be sufficient in all situations
4	Death of the mouse days/weeks after infusion of the bone marrow	Failure of the bone marrow to engraft because of poor viability or a small number of cells	Keep the bone marrow on ice during the time it is outside an animal. Be sure to infuse a proper amount of cells (agitate syringe before injection)
7	Damage to the peritoneum	Incomplete separation of the muscle layers before cutting the muscle flap	Use 5.0 vicryl and the mattress suturing technique to close the hole in the peritoneum
9	Difficulties suturing through the muscle flap	Sutures are covered with blood	Use 70% (vol/vol) ethanol and a sponge to clean the suture before proceeding
11	Skin is attached to underlying tissues	Tissue dries easily during prolonged surgery	Apply saline to the dried tissue using a cotton swab
12	Skin does not heal	The outside part of the skin was rolled inside when wound clips were applied	Ensure that only the inside parts of the skin are touching each other before applying wound clips
19	No formation of metastases	Prolonged *in vitro* culture could change the cell phenotype. Fluorescent labeling of tumor cells might affect their phenotype	Repeat the experiment using original cell stock or another fluorophore (that might be less toxic)

TIMING

Steps 1 and 2, irradiation of Actb-GFP/C57BL/6 mice: 1 h

Step 3, bone marrow transplantation: 1.5 h

Step 4, bone marrow engraftment: 4 weeks

Steps 5–17, parabiosis surgery: 1 h

Step 18, separation surgery and skin graft: 15 min

Step 19, skin graft wound healing: 1 week

Step 20, tumor implantation in skin transplant: 10 min

Step 21, tumor growth: 2–3 weeks

Step 22, lung tissue collect and evaluation of metastatic burden: 45 min

Step 23, fixation and dehydration of lung tissue: 2 d

Step 24, embedding lung tissue in OCT: 15 min

Step 25, immunohistochemical analysis: depending on the protocol used, usually 1–2 d.

Anticipated results

We used this parabiosis model to quantitatively evaluate the participation of primary site–derived host cells. LLC1 cells were implanted subcutaneously in the GFP + skin transplant, allowed to grow up to a diameter of 10 mm, and then primary tumors were excised to allow metastases to grow. GFP + host-derived cells were detectable in lung metastases in all five animals in which the primary tumor contained GFP + host cells (Fig. 3). The frequency of the involvement of host-derived cells from primary tumors in distant metastases varied between 27% and 86% of the metastatic nodules. The frequency of GFP + host cells in metastases correlated with the density of GFP + cells in the primary tumor (data not shown). Next, we collected the lungs containing LLC1 metastases with GFP + passenger stromal cells. Immunohistochemical analysis of skin-derived, GFP + stromal cells in the lungs revealed that the majority (~75%) of these cells are of mesenchymal origin[13] (Fig. 4).

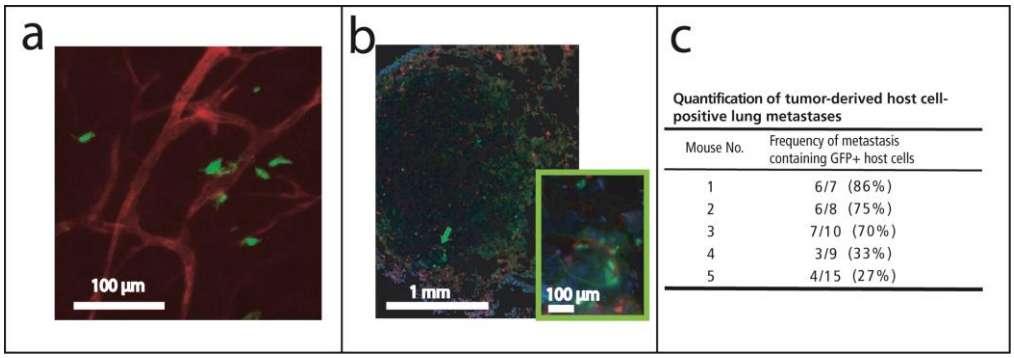

Quantification of tumor-derived host cell-positive lung metastases

Mouse No.	Frequency of metastasis containing GFP+ host cells
1	6/7 (86%)
2	6/8 (75%)
3	7/10 (70%)
4	3/9 (33%)
5	4/15 (27%)

Figure 3 | Quantification of tumor-derived GFP + stromal cells in lung metastases. Large skin flaps were transferred from Actb-GFP/C57BL mice (after C57BL/6 bone marrow transplantation) to C57BL/6 mice through parabiosis. GFP + host cells were detected in the lung metastases of subcutaneously grown LLC-1tumors (implanted in the transplanted skin area). (a,b) Multiphoton (a) and confocal microscopy (b) detection of GFP + cells in the lung metastatic foci. Inset, magnified image of the area indicated by the green arrow. (c) Quantification of the frequency of GFP + cells in metastatic nodules in the skin transplant model. Images are 315 ∝m (a), 1.72 mm (b) and 420 ∝m (inset in b) across. Blood vessels are enhanced by rhodamine-labeled infusion (shown in red) in a; DAPI nuclear counterstaining is shown in blue in b. Reproduced with permission from ref. 13. All animal procedures were performed according to the guidelines of public health service policy on humane care of laboratory animals and in accordance with an approved protocol by the Institutional Animal Care and Use Committee of MGH.

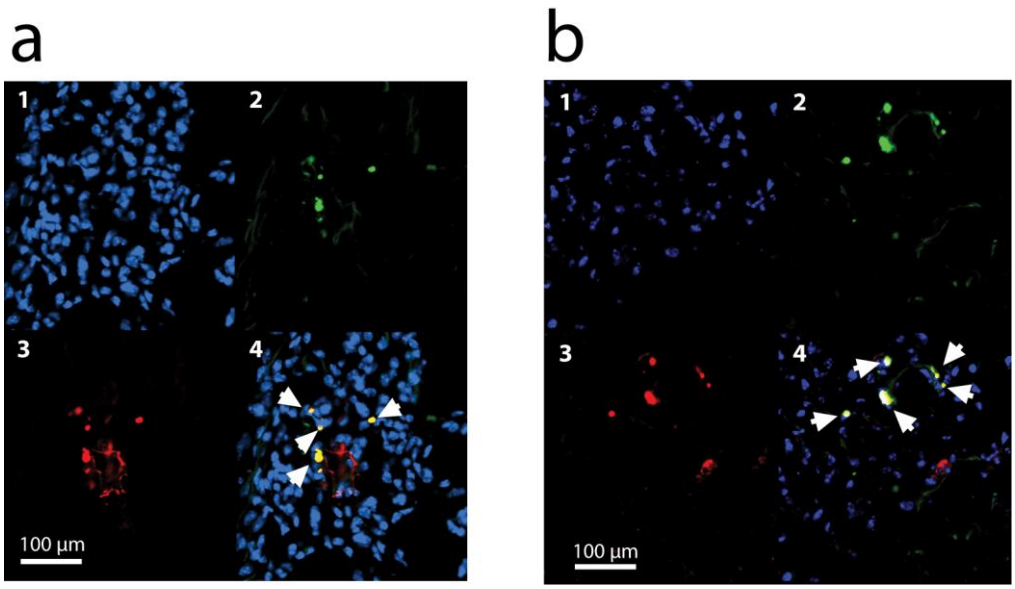

Figure 4 | Passenger stromal cells in spontaneous metastasis. (a,b) GFP + stromal cells that have metastasized spontaneously from the skin transplant to the lungs. Immunohistochemical markers have been used to show colocalization of these stromal cells with α-SMA (a) and FSP-1 (b) expression. (1) In blue, DAPI nuclear staining; (2) in green, GFP + stromal cells, (3) in red, expression of α-SMA (in a) and FSP-1 (in b), and (4) overlay of the three colors; arrows indicate colocalization of GFP and α-SMA or FSP-1 expression. Reproduced with permission from ref. 13. All animal procedures were performed according to the guidelines of public health service policy on humane care of laboratory animals and in accordance with an approved protocol by the Institutional Animal Care and Use Committee of MGH.

References

1. Barcellos-Hoff MH, Ravani SA. Irradiated mammary gland stroma promotes the expression of tumorigenic potential by unirradiated epithelial cells. *Cancer Res.* Mar 1 2000;60(5):1254-1260.

2. Bhowmick NA, Chytil A, Plieth D, et al. TGF-beta signaling in fibroblasts modulates the oncogenic potential of adjacent epithelia. *Science.* Feb 6 2004;303(5659):848-851.

3. Coussens LM, Werb Z. Inflammation and cancer. *Nature.* Dec 19-26 2002;420(6917):860-867.

4. Elenbaas B, Spirio L, Koerner F, et al. Human breast cancer cells generated by oncogenic transformation of primary mammary epithelial cells. *Genes Dev.* Jan 1 2001;15(1):50-65.

5. Jacobs TW, Byrne C, Colditz G, Connolly JL, Schnitt SJ. Radial scars in benign breast-biopsy specimens and the risk of breast cancer. *N Engl J Med.* Feb 11 1999;340(6):430-436.

6. Bhowmick NA, Neilson EG, Moses HL. Stromal fibroblasts in cancer initiation and progression. *Nature.* Nov 18 2004;432(7015):332-337.

7. Joyce JA, Pollard JW. Microenvironmental regulation of metastasis. *Nat Rev Cancer.* Apr 2009;9(4):239-252.

8. Olumi AF, Grossfeld GD, Hayward SW, Carroll PR, Tlsty TD, Cunha GR. Carcinoma-associated fibroblasts direct tumor progression of initiated human prostatic epithelium. *Cancer Res.* Oct 1 1999;59(19):5002-5011.

9. Orimo A, Gupta PB, Sgroi DC, et al. Stromal fibroblasts present in invasive human breast carcinomas promote tumor growth and angiogenesis through elevated SDF-1/CXCL12 secretion. *Cell.* May 6 2005;121(3):335-348.

10. Tlsty TD. Stromal cells can contribute oncogenic signals. *Semin Cancer Biol.* Apr 2001;11(2):97-104.

11. Fidler IJ. The pathogenesis of cancer metastasis: the 'seed and soil' hypothesis revisited. *Nat Rev Cancer.* Jun 2003;3(6):453-458.

12. Bouvet M, Tsuji K, Yang M, Jiang P, Moossa AR, Hoffman RM. In vivo color-coded imaging of the interaction of colon cancer cells and splenocytes in the formation of liver metastases. *Cancer Res.* Dec 1 2006;66(23):11293-11297.

13. Duda DG, Duyverman AM, Kohno M, et al. Malignant cells facilitate lung metastasis by bringing their own soil. *Proc Natl Acad Sci U S A.* Nov 22 2010.

14. Podsypanina K, Du YC, Jechlinger M, Beverly LJ, Hambardzumyan D, Varmus H. Seeding and propagation of untransformed mouse mammary cells in the lung. *Science.* Sep 26 2008;321(5897):1841-1844.

15. Hiratsuka S, Nakamura K, Iwai S, et al. MMP9 induction by vascular endothelial growth factor receptor-1 is involved in lung-specific metastasis. *Cancer Cell.* Oct 2002;2(4):289-300.

16. Kaplan RN, Riba RD, Zacharoulis S, et al. VEGFR1-positive haematopoietic bone marrow progenitors initiate the pre-metastatic niche. *Nature.* Dec 8 2005;438(7069):820-827.

17. Kim S, Takahashi H, Lin WW, et al. Carcinoma-produced factors activate myeloid cells through TLR2 to stimulate metastasis. *Nature.* Jan 1 2009;457(7225):102-106.

18. van Deventer HW, Wu QP, Bergstralh DT, et al. C-C chemokine receptor 5 on pulmonary fibrocytes facilitates migration and promotes metastasis via matrix metalloproteinase 9. *Am J Pathol.* Jul 2008;173(1):253-264.

19. Al-Mehdi AB, Tozawa K, Fisher AB, Shientag L, Lee A, Muschel RJ. Intravascular origin of metastasis from the proliferation of endothelium-attached tumor cells: a new model for metastasis. *Nat Med.* Jan 2000;6(1):100-102.

20. Chertow BS, Fidler WJ, Fariss BL. Graves' disease and Hashimoto's thyroiditis in monozygous twins. *Acta Endocrinol (Copenh).* Jan 1973;72(1):18-24.

21. Liotta LA, Saidel MG, Kleinerman J. The significance of hematogenous tumor cell clumps in the metastatic process. *Cancer Res.* Mar 1976;36(3):889-894.

22. Ruiter DJ, van Krieken JH, van Muijen GN, de Waal RM. Tumour metastasis: is tissue an issue? *Lancet Oncol.* Feb 2001;2(2):109-112.

23. Sahai E. Illuminating the metastatic process. *Nat Rev Cancer.* Oct 2007;7(10):737-749.

24. Fidler IJ. The relationship of embolic homogeneity, number, size and viability to the incidence of experimental metastasis. *Eur J Cancer.* Mar 1973;9(3):223-227.

25. Fukumura D, Xavier R, Sugiura T, et al. Tumor induction of VEGF promoter activity in stromal cells. *Cell.* Sep 18 1998;94(6):715-725.

26. Yang M, Li L, Jiang P, Moossa AR, Penman S, Hoffman RM. Dual-color fluorescence imaging distinguishes tumor cells from induced host angiogenic vessels and stromal cells. *Proc Natl Acad Sci U S A.* Nov 25 2003;100(24):14259-14262.

27. Albini A, Benelli R. The chemoinvasion assay: a method to assess tumor and endothelial cell invasion and its modulation. *Nat Protoc.* 2007;2(3):504-511.

28. Bayless KJ, Kwak HI, Su SC. Investigating endothelial invasion and sprouting behavior in three-dimensional collagen matrices. *Nat Protoc.* 2009;4(12):1888-1898.

29. Duyverman AM, Kohno M, Roberge S, Fukumura D, Duda DG, Jain RK. An isolated tumor perfusion model in mice. *Nat Protoc.* Apr 2012;7(4):749-755.

30. Duyverman AM, Steller EJ, Fukumura D, Jain RK, Duda DG. Studying primary tumor-associated fibroblast involvement in cancer metastasis in mice. *Nat Protoc.* Apr 2012;7(4):756-762.

31. Duda DG, Fukumura D, Munn LL, et al. Differential transplantability of tumor-associated stromal cells. *Cancer Res.* Sep 1 2004;64(17):5920-5924.

Chapter 3

An isolated tumor perfusion model in mice

Annique MMJ Duyverman
Mitsutomo Kohno
Sylvie Roberge
Dai Fukumura
Dan G Duda
Rakesh K Jain

Edwin L. Steele Laboratory for tumor Biology, Department of Radiation Oncology, Massachusetts General Hospital and Harvard Medical School, Boston, USA

Nature Protocols 2012; Vol 7, No 4: p 749-755

Abstract

The role of stromal cells in the tumor microenvironment has been extensively characterized. We and others have shown that stromal cells may participate in several steps of the metastatic cascade. This protocol describes an isolated tumor perfusion model that enables studies of cancer and stromal cell shedding. It could also be used to study the effects of therapies interfering with the shedding of tumor cells or fragments, circulating (stem) cells or biomarkers. Primary tumors are grown in a microenvironment in which stromal cells express GFP ubiquitously. tumors are implanted orthotopically or can be implanted ectopically. As a result, all tumor-associated stromal cells express GFP. This technique can be used to detect and study the role of stromal cells in tumor fragments within the circulation in mice. Studying the role of stromal cells in circulating tumor fragments using this model may take 2–10 weeks, depending on the growth rate of the primary tumor.

Introduction

Neoplastic tumor cells and host-derived stromal cells coexist in carcinomas. Clinical and preclinical evidence supports the contribution of these nonmalignant stromal cells to the development of tumors[1-6]. Many studies have shown that solid tumors actively recruit these stromal cells to create a microenvironment that promotes primary tumor growth and dissemination[7-10]. Moreover, this process is likely to be repeated when tumors colonize secondary sites during metastatic growth.

A tumor cell from the primary tumor can lead to established metastases when it successfully completes each of the sequential and interrelated steps of the metastatic cascade. Each of these steps can be rate limiting, and failure to complete a step can abrogate the entire process[11]. Recent studies have shown that the host-derived stroma may increase the efficiency of this complex system. Among the stromal cell types that have been linked to tumor promotion and progression are endothelial cells, pericytes, fibroblasts and various bone marrow–derived cells, including splenocytes, macro-phages, neutrophils, mast cells, myeloid-derived suppressor cells and mesenchymal stem cells[3, 12, 13]. Metastatic cells could reside in the lungs awaiting oncogenic activation[14], or could home to pre-existing niches created by inflammation and immune cell or fibroblast accumulation[15-18]. In addition, it has been shown that metastatic cells proliferate intravascularly before extravasation into the lung tissue[19].

Previous applications of the protocol

Studies reported more than 30 years ago showed that cancer cell clumping in circulation increases metastasis[20, 21]. These clumps may be emboli, formed in circulation because of interactions with immune cells[11, 22, 23]. Indeed, the injection of emboli-containing tumor cells increases the efficiency of metastasis. However, the clumps may also be fragments consisting of tumor cells that carry 'passenger' stromal cells from the primary site. By using the techniques described in this protocol in combination with two spontaneous metastases models - one using skin transplantation by transient parabiosis and a second using carcinoma-associated fibroblasts to selectively deplete stromal cells[24, 25] - we have recently shown that these host-derived cells increase tumor cell viability in circulation and serve as a provisional stroma in the secondary site and increase the cancer's metastatic efficiency[26].

Overview of the technique

The technique described in this protocol can be used to study circulating tumor cells originating from any primary tumor. Tumors can be implanted orthotopically or ectopically, and non-tumor-bearing mice are used as a control. Here we use the renal perfusion model in combination with primary tumor implantation in the renal capsule. Implanting tumors at different (orthotopic) sites might provide additional insights in assays of mestastasis, and they could be adapted from previously established isolated tumor models. These include transplanted and spontaneous breast cancer, ovarian cancer and liver cancer models[27-30]. The experimental design of the protocol used is depicted in Figure 1. To study tumor cells and fragments shed by the primary tumor, we implant fluorescent-labeled tumor cells in the kidney capsule. After 12 d, we use the isolated kidney-tumor perfusion model to collect tumor cells and fragments that were shed by the primary tumor. By monitoring blood pressure in the carotid artery and adjusting the perfusion rate through the jugular vein, we are able to collect tumor perfusate for up to an hour, yielding 3–4 ml of blood per mouse.

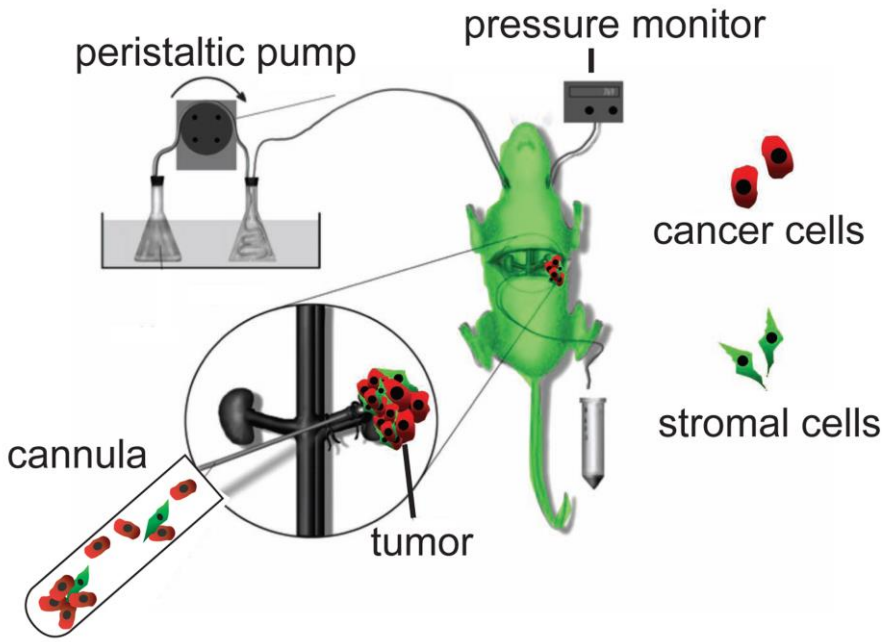

Figure 1 | Design of the experiment. LLC1-dsRed tumor cells are implanted in the renal capsule. When the tumor size is 8 mm, the renal vein is cannulated, and tumor cells and fragments are collected by filtration of the perfusate using a peristaltic pump and artificial blood perfusion. Reproduced with permission from ref. 26. All animal procedures were performed according to the guidelines of public health service policy on humane care of laboratory animals and in accordance with an approved protocol by the Institutional Animal Care and Use Committee of MGH.

Comparison with other techniques

Several in vitro assays have been developed to study host–tumor cell interactions related to progression and invasion[31, 32], including the chemoinvasion assay using the reconstituted BD Matrigel in Boyden blind-well chambers. It can be applied to detect the migratory activity associated with matrix degradation and can also be adapted to study the selective degrading activity on different matrix substrates. The advantage of this in vitro assay is the ease of controlling different parameters in the experiment. At the same time, the lack of in vivo microenvironmental factors may con-found the results. Many in vivo models have been used to examine the role of stromal components within the

primary tumor microenvironment. Human mammary tissue can be reconstructed in a mouse model to study cross talk between tissue stroma and the epithelium, as well as factors involved in breast stem cell biology of tumor initiation and progression[33]. However, there is a paucity of techniques for studying and visualizing primary tumor stromal cells in different steps of the metastatic process. We have developed an experimental protocol that can be used to quantitatively study the contribution of stromal cells to tumor fragment survival within the circulation. We describe the isolated tumor perfusion model to study the viability of tumor cells in circulating tumor fragments. This model was originally developed by Gullino, and later adapted by us for various molecular and cellular studies of cancer[27-29, 34, 35]. We have used this model to unravel the role of 'passenger' fibroblasts in tumor metastasis to the lung[26]. However, other tumor stromal cells could potentially be studied using this protocol.

Advantages and limitations

The key advantage of our protocol over other existing methods is that one can gain the ability to image and quantify in vivo all cells and fragments that are shed by the kidney, liver, ovary and inguinal gland during metastasis. Alternatively, one could use the collected cells/fragments for consecutive in vivo experiments in which the effect of drugs on tumor cell/clump shedding could be studied. The major limitation of this technique is that animals have to be exsanguinated. In addition, a large number of mice are required to study the effects of therapy over time. The renal perfusion model shown here is an ectopic tumor model, where tumors are implanted surgically in the renal capsule. However, other organs or tissues could, in principle, be used to collect efferent cells. A further potential disadvantage is that the studies require GFP + or other transgenic immunocompetent mice, which can only be used with certain (syngeneic) tumor lines.

Material

Critical: All reagents and equipment can be substituted with appropriate alternatives from other manufacturers.

REAGENTS

- PBS (Cellgro, cat. no. 20-031-CV)
- Buprenorphine hydrochloride (0.3 mg ml − 1; MGH pharmacy, cat. no. 716510) *Caution:* Buprenorphine hydrochloride is a poison, and may cause prolonged respiratory depression. Wear protective clothing to avoid contact or inhalation. Buprenorphine is a controlled substance and should be handled according to relevant rules of the host institutions.
- Ethanol (70% (vol/vol); Pharmco, cat. no. 111000190)
- Fluorescent-labeled LLC1 cells (e.g., dsRed-labeled cells; ATTC, cat. no. CRL-1642)
- Hank's balanced salt solution (1×; Gibco, cat. no. 14170)
- Heparin sodium (1,000 USP Units ml − 1; APP Pharmaceuticals, cat. no. 504011)
- Ketamine (100 mg ml − 1; MGH pharmacy) and xylazine (10 mg ml − 1; Webster, cat. no. 200204.00) mixture per kg of body weight)
- Mice, male Actb-GFP/C75BL/6, 6–10 weeks of age. *Caution:*All animal studies must be reviewed and approved by the institutional animal care and use committees to ensure that they conform to relevant ethics regulations.
- Cells for transplantation, e.g., LLC1-dsRed tumor cells
- Cyanoacrylate glue (Krazy Glue) *Caution:*Avoid contact with skin, and wear gloves when handling.
- Formaldehyde
- Paraformaldehyde
- Sodium chloride
- dH2O

EQUIPMENT

- 5-0 Ethibond sutures (Ethicon, cat. no. X698G)
- Polyethylene 10 + 50 tubing (PE10, PE50; Becton Dickinson, cat. nos. 427401 and 427411)
- Applicator tips (Owens and Minor, cat. no. 5937-W0D1002)
- Bright-field microscope
- Caliper (Roboz Surgical Instrument, cat. no. RS-6466)
- Clipper (Webster, cat. no. 78997-010)
- Fluorescence confocal or multiphoton microscope (e.g., Olympus). For confocal microscopy, use the Argon laser, 488 nm excitation and an emission filter of 505–525 nm to detect GFP signal, and the HeNe laser, 543 nm excitation and an emission filter of 565–595 nm to detect dsRed signal. For two-photon microscopy, use 840 nm excitation and an emission filter of 515–555 nm (for GFP) or/and an emission filter of 575–645 nm (for dsRed)
- Forceps (Roboz Surgical Instrument, cat. no. RS-5153, RS 5150, RS-5132)
- Gas exchanger (Becton Dickson)
- Heating pad (Shore Line, cat. no. 712.0000.04)
- Hemostatic forceps (9-inch, jaw length 6 cm; Roboz Surgical Instrument, cat. no. RS-7679)
- Micro aneurysm clip, straight, plus clip applier (Roboz Surgical Instrument, cat. no. RS-5420 + RS-8140)
- Micro forceps (2×; F.S.T. cat. no. 11063-07)
- Micro forceps (2×; Roboz Surgical Instrument, cat. no. RS-5069)
- Micro scissors (Tiemann, cat. no. 160-147)
- Needle holder (14 cm; Roboz Surgical Instrument, cat. no. RS-6412)
- Peristaltic pump (Ismatec cat. no. 7618-3)
- Permanent marker (Staedtler, cat. no. 342-9)
- Pressure transducer (Gould INC)
- Reservoir of Oxyglobin (Biopure, cat. no. HBOC-301)
- Scissors (Roboz Surgical Instrument, cat. no. RS-5840, RS-5883)
- Silastic tubing (Fisher, cat. no. 11-18915C)

- Three-way stopcock (Cole-Parmer, cat. no. 30600-02)
- Surgical blade (no.10; Fisher Scientific, cat. no. 08-916-5A)
- Scalpel handle (Roboz Surgical Instrument, cat. no. RS-9843)
- Syringe (1 cc with a 26-G needle for anesthesia; Fisher Scientific, cat. no. 14-823-2E)
- 30-G needle for injecting tumor cells
- 6-0 silk sutures

REAGENT SETUP

Paraformaldehyde 4% (wt/vol): Add 180 ml of 1× PBS to 120 ml of 10% (wt/vol) formaldehyde. *Critical:* This solution has a short shelf life (< 1 week); therefore, it should be freshly prepared on the day of the experiment.
Buprenorphine hydrochloride: Dissolve 1 ml of the 0.3 mg ml − 1 stock solution in 30 ml of 0.9% (wt/vol) sodium chloride. Store at 20 °C for up to 3 months. PBS (1×) Add 100 ml of 10× PBS to 900 ml of dH2O. Store at 20 °C for up to 9 months.
Ethanol 70% (vol/vol): Mix 1.7 liters of dH2O and 1 gallon of 100% ethanol. Store at 20 °C in a closed container.
Heparin: Dilute 0.3 ml of stock solution in 30 ml of sodium chloride (freshly prepare for each experiment).

Procedure

Tumor implantation in the left kidney

1| Anesthetize a male Actb-GFP/C57BL/6 mouse, 6–10 weeks of age, using an intramuscular injection of 0.4 ml of ketamine/xylazine and place it on a heating pad.

2| Position the mouse on the heating pad with the left flank facing the surgeon. Make an 8-mm incision through the skin and muscle layers approximately 1 cm lateral to the spine and 3 mm dorsal to the lowest ribs. Externalize the left kidney using applicator tips.

3| Create a small pocket under the renal capsule using the tip of the micro syringe. Inject 1×10^6 LLC1-dsRed tumor cells in 0.1 ml of Hank's balanced salt solution in the renal capsule using a 30-G needle.

4| Remove any liquids that are leaking out of the capsule using an applicator tip.

5| Close the muscle layers and skin using 5-0 Ethibond sutures. Keep the mice in appropriate cages under sterile conditions and allow the tumors to grow to 8 mm.

6| At the preferred time point (e.g., 2 weeks after implantation of LLC1 tumors), anesthetize the mouse using an intramuscular injection of 0.4 ml of ketamine/xylazine and keep it on a heating pad.

7| Open the abdomen by laparatomy to inspect the location of the kidney tumor. Reposition the organs and cover the abdomen with skin and a sponge before moving to the next step.

Cannulation of the carotid artery

8| Position the mouse on its back, with the mouse's head facing the surgeon. Fix the head by taping it across the nose and fix the body by taping across the paws and the sternum (Fig. 2a).

9| Make a midline incision under the chin, exposing the salivary glands. Expose the trachea by separating the salivary glands sideways using the micro forceps (Fig. 2b).

10| Dissect the muscles overlying the carotid artery using microdissection forceps and dissection microscope. *Critical step:* It is important to remove all the connective tissue surrounding the carotid artery, as this facilitates cannulation.

11| Loop two 6-0 silk sutures around the artery, 5 mm apart, and then close the cranial ligature. Make a loose knot in the caudal suture (Fig. 2c).

12| Apply the hemostatic clamp onto the carotid artery caudal to the loose knot (Fig. 2c).

Figure 2 | Cannulation of the carotid artery. (a) Position the mouse on its back, head facing the surgeon. Fix the head by taping it across the nose and fix the body by taping across the paws and the sternum. (b) Make a midline incision under the chin, exposing the salivary glands. Expose the trachea by separating the salivary glands sideways using the micro forceps. (c) Apply the hemostatic clamp onto the carotid artery caudal to the loose knot. All animal procedures were performed according to the guidelines of public health service policy on humane care of laboratory animals and in accordance with an approved protocol by the Institutional Animal Care and Use Committee of MGH.

13| Connect the heparin-filled PE10 tubing to a three-way stopcock and pressure transducer through a 30-G needle. While holding the cranial suture, cut across one-third of the carotid vessel wall with microscissors, and then insert the heparin-filled PE10 tubing into the vessel toward the hemostatic clamp.

Critical step: Do not section the vessel completely, as this makes inserting the tubing impossible. Release the clamp and insert the tubing 3 mm beyond the clamp.

14| Close the suture around the vessel and tubing to secure the tubing. Total tubing insertion is 8 mm. At the other end of the PE tubing, insert a 30-G needle connected to a three-way stopcock and the pressure transducer. Add a drop of Krazy Glue to fix the tubing and vessel.

Cannulation of the jugular vein

15| Move to the right side of the trachea to cannulate the jugular vein.

16| Remove the connective tissue surrounding the jugular vein for 8 mm. If any vessel branches off the vein, then ligate it with two silk sutures and cut in between.

Critical step: Dissect the jugular vein in its anatomical position to avoid rupture of this delicate vein; it has a much thinner wall than the carotid artery.

17| Loop two 6-0 silk sutures around the vein, 5 mm apart, and then close the cranial ligature. Make a loose knot in the caudal suture.

18| Apply the hemostatic clamp onto the jugular vein caudal to the loose knot.

19| Connect the PE50 tubing to a reservoir of Oxyglobin. While holding the cranial suture, cut across one-third of the vessel wall using microscissors and insert the PE50 tubing in the direction of the hemostatic clamp. Release the clamp and insert the tubing 3 mm beyond the clamp. Close the suture around the vessel and tubing, and add a drop of Krazy Glue to secure the tubing. The total tubing insertion length is 8 mm.

Critical step: As there is not yet any marked loss of circulating volume, perfuse at very low rates.

Kidney perfusion

20| Reposition the mouse on its back with the tail facing the surgeon.

Critical step: Do not disturb the tubing inserted in the carotid artery or jugular vein while repositioning the animal.

21| Access the abdominal cavity through the previously performed laparatomy.

22| Move and hold all the organs to the right side using a wet sponge to clear the field for the cannulation of the left renal vein.

23| Locate the left adrenal vein and testicular vein draining into the renal vein and ligate both to avoid rupture. Use two 6-0 silk sutures to ligate the branches and cut in between to create a space to move the renal vein around.

24| Dissect the connective tissue around the renal vein to locate the renal artery, which is behind the vein, and then separate the two.

25| Loop two 6-0 silk sutures around the renal vein. Close the proximal one and keep a loose knot in the distal one for tube insertion. While holding the closed suture, cut 30% of the vein across and insert a 5-cm-long, heparinized PE10 as close to the kidney as possible. Close the suture to fix the tubing and add a drop of Krazy Glue at the point of insertion.

26| Collect the dripping perfusate into the 15-ml collection tube kept on ice, and increase the Oxyglobin flow to maintain a physiological pressure between 60 and 100 mm Hg. Oxygenation of the perfusate solution is achieved by a gas exchanger in which the perfusate is led through 16 feet of silastic tubing while being equilibrated with warm humidified 95% O2 and 5% CO2. During the experiment, keep the perfusate in a heated bath and lead it through the gas exchanger and then into the jugular vein into the mouse's circulation.

27| Cover the open abdomen with a wet sponge for the remaining time of the experiment, up to 1 hour.

Troubleshooting advice can be found in table 1.

TABLE 1 | Troubleshooting table.

Step	Problem	Possible reason	Solution
2	Inability to exteriorize the kidney	Incision is not in the correct place	Reposition/enlarge the incision
3	Injected cells leak out	Pocket is not large enough	Exclude the mouse from procedure and create larger pockets without rupturing the renal capsule
7	Tumor is growing close to the kidney vein or invades more than 30% of the kidney	Blood flow from the kidney into the renal vein is impaired by the tumor	Exclude the mouse from the procedure
13	Difficulty inserting the tubing into the vessel	Tubing is not shaped correctly	Cut the tubing diagonally for easier insertion
14	Cannula leak	Knot not secured tightly	Leave the inferior knot in place, loop and knot an additional suture proximally and tighten securely
	Obstructed tubing	Blood clot in the tubing	Heparinize the tubing with 0.05 M heparin
14, 19, 25	Extravasation of the tubing	Tubing is disconnected during repositioning of the animal	Securely tighten the knots in sutures and apply glue
26	Collected cells are not viable	Cell death	Keep the perfusate on ice during the experiment
27	Premature death of the mouse	Hyper/hypotension	Carefully monitor blood pressure during the collection of perfusate and adjust Oxyglobin flow

TIMING

Steps 1 and 2, anesthesia and positioning of the mouse: 10 min Steps 3 and 4, tumor cell injection: 3 min

Step 5, muscle and skin closure: 10 min

Steps 6–14, cannulation of the carotid artery: 10 min

Steps 15–19, cannulation of the jugular vein: 20 min

Steps 20–26, cannulation of renal artery: 20 min

Step 27, collection of perfusate: 1 h

Anticipated results

Figure 2 shows some typical results of the renal perfusion model. Heterogeneous tumor and stromal cell clumps can be detected in the filtered perfusate using a fluorescence microscope (Fig. 2). These harvested clumps and single cells can be further studied for viability, composition or expression of specific proteins of interest. In our study, the vast majority (~81%) of the shed dsRed + cancer cells were single cells (Fig. 3a). However, we also collected small tumor clumps (≤200 μm in diameter), and all tumor clumps composed of six or more cells contained GFP-expressing host cells (Fig. 3a). In addition, caspase 3 and caspase 7 activation - a measure of apoptosis - was detectable in most (~88%) of the single or doublets of cancer cells at the time of shedding. In contrast, the heterotypic cell clumps contained almost twice as many viable cancer cells (22.8 ± 4.5%, $P < 0.05$; see Fig. 3b). The clumps can be used for consecutive in vitro or in vivo experiments to study the effect of antimetastatic drugs on tumor cell clumping and viability (Fig. 4).

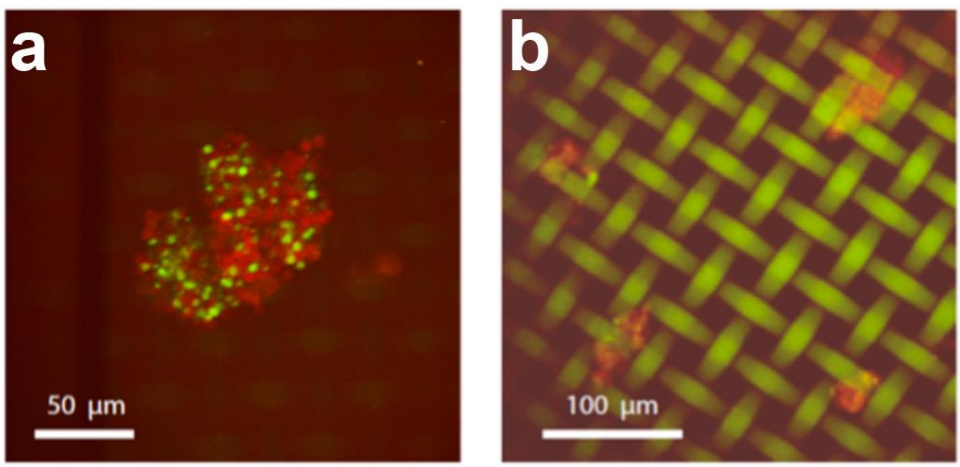

Figure 3 | Representative images of tumor cell clumps retained on a 40-mm mesh. (a,b) Clumps filtered from tumor perfusate. Red, LLC1-dsRed cells; green, GFP + host-derived cells from the Actb-GFP/C57BL/6 mice.

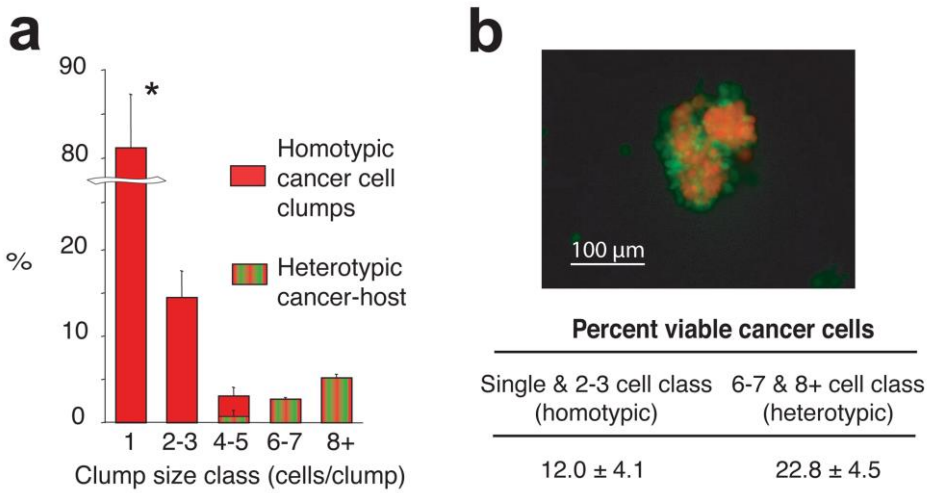

Figure 4 | Size and viability of circulating metastatic cancer cells. (a) Histogram of the composition of shed tumor cells/clumps obtained from the renal perfusion experiment (n = 5 mice). The majority of shed cancer cells were single or doublets. Host-derived GFP + cells were present in all large clumps consisting of more than 4–5 cells (*P < 0.05). (b) Representative fluorescence multiphoton laser scanning microscopy image of a heterogeneous clump, shed by a tumor, using the isolated renal perfusion model (green, GFP + stromal cells; red, dsRed + tumor cells). Image is 420 µm across. Reproduced with permission from ref. 26. All animal procedures were performed according to the guidelines of public health service policy on humane care of laboratory animals and in accordance with an approved protocol by the Institutional Animal Care and Use Committee of MGH.

References

1. Barcellos-Hoff MH, Ravani SA. Irradiated mammary gland stroma promotes the expression of tumorigenic potential by unirradiated epithelial cells. *Cancer Res.* Mar 1 2000;60(5):1254-1260.

2. Bhowmick NA, Chytil A, Plieth D, et al. TGF-beta signaling in fibroblasts modulates the oncogenic potential of adjacent epithelia. *Science.* Feb 6 2004;303(5659):848-851.

3. Bouvet M, Tsuji K, Yang M, Jiang P, Moossa AR, Hoffman RM. In vivo color-coded imaging of the interaction of colon cancer cells and splenocytes in the formation of liver metastases. *Cancer Res.* Dec 1 2006;66(23):11293-11297.

4. Coussens LM, Werb Z. Inflammation and cancer. *Nature.* Dec 19-26 2002;420(6917):860-867.

5. Elenbaas B, Spirio L, Koerner F, et al. Human breast cancer cells generated by oncogenic transformation of primary mammary epithelial cells. *Genes Dev.* Jan 1 2001;15(1):50-65.

6. Jacobs TW, Byrne C, Colditz G, Connolly JL, Schnitt SJ. Radial scars in benign breast-biopsy specimens and the risk of breast cancer. *N Engl J Med.* Feb 11 1999;340(6):430-436.

7. Bhowmick NA, Neilson EG, Moses HL. Stromal fibroblasts in cancer initiation and progression. *Nature.* Nov 18 2004;432(7015):332-337.

8. Olumi AF, Grossfeld GD, Hayward SW, Carroll PR, Tlsty TD, Cunha GR. Carcinoma-associated fibroblasts direct tumor progression of initiated human prostatic epithelium. *Cancer Res.* Oct 1 1999;59(19):5002-5011.

9. Orimo A, Gupta PB, Sgroi DC, et al. Stromal fibroblasts present in invasive human breast carcinomas promote tumor growth and angiogenesis through elevated SDF-1/CXCL12 secretion. *Cell.* May 6 2005;121(3):335-348.

10. Tlsty TD. Stromal cells can contribute oncogenic signals. *Semin Cancer Biol.* Apr 2001;11(2):97-104.

11. Fidler IJ. The pathogenesis of cancer metastasis: the 'seed and soil' hypothesis revisited. *Nat Rev Cancer.* Jun 2003;3(6):453-458.

12. Fukumura D, Xavier R, Sugiura T, et al. Tumor induction of VEGF promoter activity in stromal cells. *Cell.* Sep 18 1998;94(6):715-725.

13. Joyce JA, Pollard JW. Microenvironmental regulation of metastasis. *Nat Rev Cancer.* Apr 2009;9(4):239-252.

14. Podsypanina K, Du YC, Jechlinger M, Beverly LJ, Hambardzumyan D, Varmus H. Seeding and propagation of untransformed mouse mammary cells in the lung. *Science.* Sep 26 2008;321(5897):1841-1844.

15. Hiratsuka S, Nakamura K, Iwai S, et al. MMP9 induction by vascular endothelial growth factor receptor-1 is involved in lung-specific metastasis. *Cancer Cell.* Oct 2002;2(4):289-300.

16. Kaplan RN, Riba RD, Zacharoulis S, et al. VEGFR1-positive haematopoietic bone marrow progenitors initiate the pre-metastatic niche. *Nature.* Dec 8 2005;438(7069):820-827.

17. Kim S, Takahashi H, Lin WW, et al. Carcinoma-produced factors activate myeloid cells through TLR2 to stimulate metastasis. *Nature.* Jan 1 2009;457(7225):102-106.

18. van Deventer HW, Wu QP, Bergstralh DT, et al. C-C chemokine receptor 5 on pulmonary fibrocytes facilitates migration and promotes metastasis via matrix metalloproteinase 9. *Am J Pathol.* Jul 2008;173(1):253-264.

19. Al-Mehdi AB, Tozawa K, Fisher AB, Shientag L, Lee A, Muschel RJ. Intravascular origin of metastasis from the proliferation of endothelium-attached tumor cells: a new model for metastasis. *Nat Med.* Jan 2000;6(1):100-102.

20. Fidler IJ. The relationship of embolic homogeneity, number, size and viability to the incidence of experimental metastasis. *Eur J Cancer.* Mar 1973;9(3):223-227.

21. Liotta LA, Saidel MG, Kleinerman J. The significance of hematogenous tumor cell clumps in the metastatic process. *Cancer Res.* Mar 1976;36(3):889-894.

22. Ruiter DJ, van Krieken JH, van Muijen GN, de Waal RM. Tumour metastasis: is tissue an issue? *Lancet Oncol.* Feb 2001;2(2):109-112.

23. Sahai E. Illuminating the metastatic process. *Nat Rev Cancer.* Oct 2007;7(10):737-749.

24. Duyverman AM, Kohno M, Duda DG, Jain RK, Fukumura D. A transient parabiosis skin transplantation model in mice. *Nat Protoc.* Apr 2012;7(4):763-770.

25. Duyverman AM, Steller EJ, Fukumura D, Jain RK, Duda DG. Studying primary tumor-associated fibroblast involvement in cancer metastasis in mice. *Nat Protoc.* Apr 2012;7(4):756-762.

26. Duda DG, Duyverman AM, Kohno M, et al. Malignant cells facilitate lung metastasis by bringing their own soil. *Proc Natl Acad Sci U S A.* Nov 22 2010.

27. Gullino PM. Tumor pathophysiology: the perfusion model. *Antibiot Chemother.* 1980;28:35-42.

28. Gullino PM, Grantham FH. Studies on the exchange of fluids between host and tumor. I. A method for growing "tissue-isolated" tumors in laboratory animals. *J Natl Cancer Inst.* Sep 1961;27:679-693.

29. Kristensen CA, Roberge S, Jain RK. Effect of tumor necrosis factor alpha on vascular resistance, nitric oxide production, and glucose and oxygen consumption in perfused tissue-isolated human melanoma xenografts. *Clin Cancer Res.* Mar 1997;3(3):319-324.

30. Nakhasi HL, Grantham FH, Gullino PM. Expression of kappa-casein in normal and neoplastic rat mammary gland is under the control of prolactin. *J Biol Chem.* Dec 10 1984;259(23):14894-14898.

31. Albini A, Benelli R. The chemoinvasion assay: a method to assess tumor and endothelial cell invasion and its modulation. *Nat Protoc.* 2007;2(3):504-511.

32. Bayless KJ, Kwak HI, Su SC. Investigating endothelial invasion and sprouting behavior in three-dimensional collagen matrices. *Nat Protoc.* 2009;4(12):1888-1898.

33. Proia DAK, C. Reconstruction of human mammary tissue in a mouse model. *Nature Protocols.* 2006;1:206-214.

34. Bockhorn M, Roberge S, Sousa C, Jain RK, Munn LL. Differential gene expression in metastasizing cells shed from kidney tumors. *Cancer Res.* Apr 1 2004;64(7):2469-2473.

35. Swartz MA, Kristensen CA, Melder RJ, et al. Cells shed from tumours show reduced clonogenicity, resistance to apoptosis, and in vivo tumorigenicity. *British Journal of Cancer.* Nov 1999;81(5):756-759.

Chapter 4

Studying primary tumor–associated fibroblast involvement in cancer metastasis in mice

Annique MMJ Duyverman
Ernst JA Steller
Dai Fukumura
Rakesh K Jain
Dan G Duda

Edwin L. Steele Laboratory for tumor Biology, Department of Radiation Oncology, Massachusetts General Hospital and Harvard Medical School, Boston, USA

Nature Protocols 2012; Vol 7, No 4: p 756-762

Abstract

Stromal cells have been studied extensively in the primary tumor microenvironment. In addition, mesenchymal stromal cells may participate in several steps of the metastatic cascade. Studying this interaction requires methods to distinguish and target stromal cells originating from the primary tumor versus their counterparts in the metastatic site. Here we illustrate a model of human tumor stromal cell—mouse cancer cell coimplantation. This model can be used to selectively deplete human stromal cells (using diphtheria toxin, DT) without affecting mouse cancer cells or host-derived stromal cells. Establishment of novel genetic models (e.g., transgenic expression of the DT receptor in specific cells) may eventually allow analogous models using syngeneic cells. Studying the role of stromal cells in metastasis using the model outlined above may take 8 weeks.

Introduction

Tumor-associated fibroblasts (TAFs) have important and diverse roles in carcinogenesis and tumor growth[1-9]. Although much less studied, primary TAF involvement is also potentially crucial when tumors colonize secondary sites during metastasis. Metastatic cells can reside in the lungs awaiting oncogenic activation[10], or can home to pre-existing niches created by inflammation and immune cell or fibrocyte accumulation[11-14]. Alternatively, metastatic cells can proliferate intravascularly before extravasation into the lung tissue[15]. This could be a result of cancer cell clumping in circulation, a phenomenon that increases metastasis efficiency[16-20]. However, the clumps may also be fragments that carry over 'passenger' mesenchymal stromal cells from the primary site. By using the techniques described in this protocol, we have recently shown that mesenchymal stromal cells may serve as a provisional stroma in the secondary site and increase the metastatic efficiency of cancer[21].

We developed an experimental protocol of spontaneous lung metastasis formation in mice in which human TAFs (originating from the primary tumor) can be selectively depleted using DT once they colonize the lungs. We have used this protocol - in combination with established spontaneous metastasis models using skin transplantation by transient parabiosis and an isolated tumor perfusion model[22, 23] - to provide direct evidence for the role of passenger TAFs in tumor metastasis to the lungs (see ref. 21).

Overview of the technique

This protocol describes an experiment for studying the involvement of stromal cells in specific steps in the metastatic cascade. The experimental design of the protocol is depicted in Figure 1. We have previously used this protocol in a spontaneous metastasis formation model. We first isolated TAFs from fresh human breast cancer tissue, from independent cases of sporadic invasive ductal breast carcinomas (TNM stage II, SBR grade II–III). TAFs and tumor cells (LLC1) were implanted in the hind limb of a mouse and primary tumors were allowed to grow to a size of 10 mm before they were surgically

resected. To determine the effect of passenger stromal cells within the circulating fragments, we selectively depleted the human TAFs using DT, which is 1,000 times more toxic to human cells compared with mouse cells[24, 25]. The dosage of DT used in this protocol was effective in depleting human soft tissue sarcoma cells and TAFs, while having no adverse effect on mouse cell growth (i.e., normal or cancer cells)[24, 25]. However, we recommend first determining an in vitro dose-response curve when using DT to deplete other types of human cells. Mice bearing LLC1 tumors were used as controls. Metastases were counted in the lungs 2 weeks later with a dissecting microscope and whole-mount lung tissue. Human passenger stromal cells were identified in metastatic nodules by immunohistochemistry using human-specific antibodies.

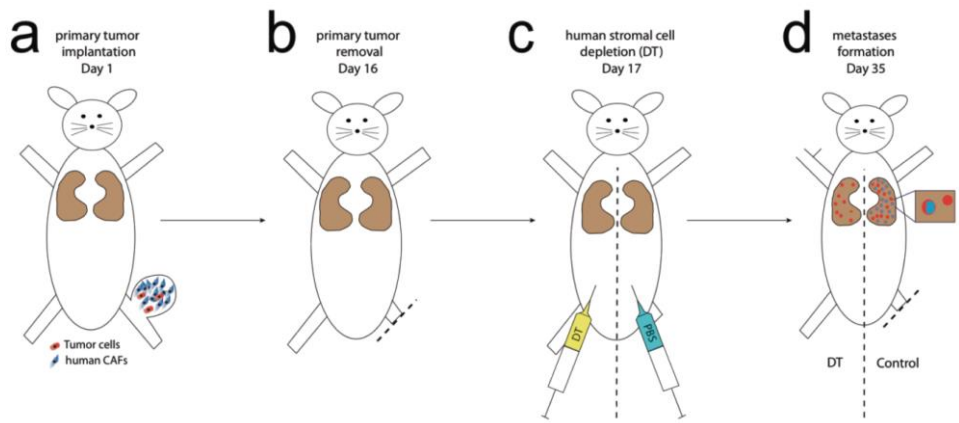

Figure 1 | Design of the experiment (a–d) The use of human tumor (carcinoma)-associated fibroblasts (CAFs) enables selective depletion of stromal cells in a spontaneous metastasis model in mice with DT treatment using the following steps: primary tumor inoculation using metastatic mouse cancer cells (red) and human CAFs (blue) (a); primary tumor resection (b); depletion of human CAFs using diphtheria toxin 1 d after resection (c); and metastases formation in the lungs (d). All animal procedures were performed according to the guidelines of public health service policy on humane care of laboratory animals and in accordance with an approved protocol by the institutional animal care and use committee of MGH.

Comparison with other techniques

The hind limb model is a very reproducible postsurgical metastasis model without the risk of local tumor regrowth[26-28]. Tumor resection when grown in other sites (e.g., mammary pad) is technically feasible but is associated with high local relapse rates, which confounds the study outcomes. In addition, there are alternative models of fibroblast depletion that could be performed at specific time points during tumor progression. One example is the use of transgenic mice expressing the herpes simplex virus thymidine kinase (HSV-TK) under the type I collagen promoter[29]. Another example is the use of transgenic mice that express HSV-TK under control of the S100A4 (FSP1) promoter to specifically ablate S100A4 + stromal cells[5]. Treatment with the antiviral agent ganciclovir can specifically induce apoptosis in cells expressing these markers. TAFs collected from these mice could potentially be used for coimplantation with tumor cells in a spontaneous model of metastasis.

Advantages and limitations

The key advantage of our protocol over other existing methods is that one can gain the ability to selectively deplete tumor stromal cells without affecting the microenvironment in the secondary site by coimplanting human-derived stromal cells with mouse tumor cells, followed by cell depletion using human-selective toxins. The limitation is the fact that the model uses xenotransplantation of a human tumor in an immunocompromised mouse. This limitation could be overcome by developing transgenic models, if feasible, of tumor stromal cell depletion using genetic tools in syngeneic and orthotopic tumor models.

Applications of the TAF model

- In our experiments, we use TAFs isolated from human breast cancer tissue. By using the same technique, tissue-specific fibroblasts could be isolated from other organs such as prostate or liver (hepatic stellate cells)[30, 31].
- In our studies, we have focused on lung cancer and TAFs. However, in principle, the protocol could be used with any cancer line that is spontaneously metastatic to the lung in mouse experimental models, such as carcinomas (mammary, prostate, lung) and melanomas.
- Tumor models bearing metastases in organs other than the lungs can be used to study organ-specific metastasis and microenvironment.

Materials

REAGENTS

- PBS (1×; Cellgro, cat. no. 20-031-CV)
- Antibodies: vimentin clone 3B4 (DAKO, cat. no. M7020), α-SMA (DAKO, cat. no. M0851), anti-pan-cytokeratin AE1-AE3 (Boehringer Mannheim) and CD31 (DAKO, cat. no. M0823)
- Buprenorphine hydrochloride (0.3 mg ml − 1; MGH pharmacy, cat. no. 716510) *caution:* Buprenorphine hydrochloride is a poison; it may cause prolonged respiratory depression. Wear protective clothing to avoid contact or inhalation. Buprenorphine is a controlled substance and should be handled according to relevant rules of the host institutions.
- Calf serum (CS; Sigma, cat. no. C8056)
- Collagenase type I (1 mg ml − 1; Boehringer Mannheim)
- Diphtheria toxin (DT) from Corynebacterium diphtheriae, lyophilized powder, 1 mg per vial (Sigma-Aldrich, cat. no. D0564) *caution:* DT is a pyrogen; do not inhale or expose it to the skin. Handle DT in a chemical hood while wearing appropriate protective clothing.
- Dulbecco's modified Eagle's medium (DMEM; Sigma, cat. no. D 5030)

- Ethanol (70% (vol/vol); Pharmco, cat. no. 111000190)
- Fatal-Plus (Vortech, cat. no. NDC 298-9373-68) *caution:* Fatal-Plus is a poisonous agent; caution should be exercised to avoid contact of the drug with open wounds or accidental self-inflicted injections.
- Human fibroblasts isolated from human breast cancer tissue
  caution: Appropriate permissions must be obtained prior to using human breast tissue.
- Human carcinoma–associated fibroblasts (isolated from human patients)
- LLC1 cells (ATTC, cat. no. CRL-1642)
- Hank's balanced salt solution (HBSS, 1×; Gibco, cat. no. 14170)
- Hyaluronidase (125 units ml − 1; Sigma)
- Ketamine (100 mg ml − 1; MGH pharmacy) and xylazine (10 mg ml − 1; Webster, cat. no. 200204.00) mixture per kg body weight
- Mice; immunodeficient mice (Nude/SCID) 6–10 weeks of age
  caution: All animal studies must be reviewed and approved by the institutional animal care and use committees and conform to all relevant ethics regulations.
- Paraformaldehyde (10% (wt/vol); Polyscience, cat. no. 4018)
  caution: Hazardous when exposed to skin, inhaled or swallowed. Preparation of 4% (wt/vol) paraformaldehyde should be carried out in a chemical hood with appropriate clothing.
- Sodium chloride

EQUIPMENT

- Autoclip applier plus 9-mm autoclips (Roboz, cat. no. RS-9260 + RS-9262)
- Bright-field microscope
- Caliper (Roboz, cat. no. RS-6466)
- Clipper (Webster, cat. no. 78997-010)
- Cryomolds (Cardinal Health, cat. no. M7144-13)
- Cryostat (Microm, cat. no. HM-560)
- Fluorescence microscope (Cambridge Research & Instrumentation)
- Heating pad (Shore Line, cat. no. 712.0000.04)

- Hemostatic forceps, 9 inch, jaw length 6 cm (Roboz, cat. no. RS-7679)
- MacLab (AD Instruments, cat. no. ML305)
- Surgical blade no. 10 (Fisher Scientific, cat. no. 08-916-5A), scalpel handle (Roboz, cat. no. RS-9843)
- Syringe, 1 ml with 26-G needle for anesthesia (Fisher Scientific, cat. no. 14-823-2E)
- Incubator

REAGENT SETUP

Paraformaldehyde 4%: (wt/vol) Prepare by adding 180 ml of 1× PBS to 120 ml of 10% (wt/vol) formaldehyde. *Critical step:* This solution has a short shelf-life (<1 week). Diphtheria toxin: Reconstitute 1 mg of powder in the vial with 0.5 ml of 1× PBS to prepare stock solution (the solution will contain 1 mg of toxin in 10 mM Tris and 1 mM disodium EDTA at pH 7.5). To prepare 10 ml of final concentration (1 μg ml − 1), add 5 μl of the stock solution to 200 ml of 1× PBS. Treat mice by one intraperitoneal (i.p.) injection of 0.2 ml of DT. Store at 4 °C for up to 4 weeks.
Buprenorphine hydrochloride: Dissolve 1 ml of the 0.3 mg ml − 1 stock solution in 30 ml 0.9% (wt/vol) sodium chloride. Store at 20 °C for up to 3 months. PBS (1×) Add 100 ml of 10× PBS to 900 ml of dH2O. Store at room temperature (20 °C) for up to 9 months.
Ethanol 70%: (vol/vol) Mix 1.7 liters of dH2O and 1 gallon of 100% ethanol. Store at 20 °C in a closed container.

Procedure

Isolation of human TAFs from breast adenocarcinomas - TIMING 3 months

1| Isolate fibroblasts from cancer- and non-cancer–associated regions of breast tissues dissected from whole breast mastectomies as determined by gross examination at the time of surgical excision and subsequent histological analysis (see original method in ref. 6).

Caution: Appropriate permissions must be obtained prior to using breast tissue. *Critical step:* Select minimally necrotic regions of the tumor mass.

2| Digest tissues using collagenase type I (1 mg ml − 1) and hyaluronidase (125 U ml − 1) at 37 °C with agitation for 12–18 h in DMEM with 10% (vol/vol) CS.

3| Incubate the dissociated tissues for 5 min at 20 °C without shaking.

4| Transfer the stromal cell–enriched supernatant to a new tube (other tissues can be discarded).

5| Centrifuge the stromal cell fraction at 250g for 5 min and resuspend the pellet (containing human TAF cells) in DMEM with 10% (vol/vol) CS and transfer to 15-cm tissue culture plates.

6| Expand TAFs by in vitro passage for two or three population doublings in DMEM with 10% (vol/vol) CS in an incubator at 37 °C and in 5% CO2.

7| Check the purity of these cell populations using immunocytochemistry with fluorescently labeled antibodies against human vimentin (clone 3B4), α-SMA, pan-cytokeratin AE1-AE3 and CD31. These should be performed according to the manufacturers' protocols.

Pause point: Cells can be stored in liquid nitrogen indefinitely.

Primary tumor implantation - TIMING 1.5 h

8| Use 8-week-old SCID mice. Anesthetize each mouse using 0.25 ml of ketamine/xylazine, place it on a heated pad, and then shave its right hind limb.

9| Coimplant 2 × 105 LLC1 tumor cells and 1 × 106 TAFs (1:5 ratio) in 50 μl of HBSS in the right leg of the mouse using a 1-ml syringe with a 30-G needle. Insert the needle through the skin 1 mm distal to the knee joint on the lateral side.
Create a 3-mm2 subcutaneous pocket by breaking through the muscle ligaments and moving the needle gently. Inject the cell mixture while retracting the needle. Tumors usually form in 100% of the mice. *Critical step:* TAFs should be used before the ninth in vitro passage, as they tend to grow slower (become senescent) afterward. *Critical step:* Avoid puncturing the skin while creating the pocket. This will cause the cell solution to leak out during injection.

Primary tumor resection - TIMING 30 min

10| House the mice under standard pathogen-free conditions. Monitor the tumor growth daily and perform surgical resection as detailed below when tumors reach a mean diameter of 10 mm.

11| Anesthetize the mouse using 0.4 ml of ketamine/xylazine mixture, and then place the mouse on a heated pad. *Critical step:* Dose the anesthesia carefully depending on the weight and strain of the mouse. For this procedure, deep anesthesia is required.

12| Five minutes after injection of the anesthetic, confirm that the mice are not responsive to pain stimuli (tail pinch, toe pinch).

13| Shave the right inguinal region.

14| Position a hemostatic clamp proximal to the tumor over the hip joint and close it tightly. Ensure that the site is clear of tumor tissue. At the same time, position the clamp as distal to the hip joint as possible to avoid clamping of the bladder and mouse genitals. The same clamping method could be use to resect tumors grown subcutaneously or in the mammary fat pad, but there is a higher risk of local regrowth of the tumors, which may confound the outcomes.

15| Resect the hind limb distal to the clamp by using a surgical blade and holding the hemostatic clamp in the other hand. *Critical step:* Cut away from the hand in order to avoid injuries to the mouse and the researcher.

16| Wait for 7 min to allow hemostasis while keeping the mouse on a heated pad.

17| Release the hemostatic clamp and check the resection site for residual bleeding. When the wound is dry, close it with four 9-mm wound clips.

18| Administer 0.2 ml of buprenorphine and ensure that the mice have easy access to food and water for 24 h postoperatively.

Selective depletion of human TAFs with DT - TIMING 15 min

19| Prepare a 1-ml syringe with 0.2 ml of DT at a concentration of 1 μg ml − 1 in PBS (use 0.2 ml of PBS for controls).

20| Hold the mouse with the left thumb and index finger by the neck skin, stretch it over the left hand and hold the tail using the little finger on your left hand. With your right hand, inject the DT intraperitoneally in the lower right quadrant of the mouse's abdomen. Move the needle to ensure that the DT is not injected in the internal organs. To confirm the selective killing of human tissue–derived TAFs, use two control groups: mice injected with mouse tumor cells alone, and mice injected with cancer cells and human TAFs and treated with inactive forms of DT (i.e., diphtheria toxoids). *Critical step:* Inject all solutions at room temperature to avoid a drop in body temperature after injection.

Tissue collection and evaluation of metastatic tumor load in the lungs - TIMING 30 min

21| At the end point of the study (i.e., when metastases have formed in the target organ (e.g., 2 weeks after TAF depletion for LLC1 metastasis to the lungs)), euthanize the mice; use an i.p. injection of 0.2 ml of Fatal-Plus using a 1-ml syringe and a 26-G needle when the first mouse shows a body weight loss of more than 20%, signs of severe pain or distress (including ruffled hair, inability to self-ambulate and signs of dehydration), or when mice become moribund. Typically, the time point is approximately 14–21 d after primary tumor resection in this model.

22| Open the thoracic cavity with forceps and scissors.

23| Collect the lungs and separate the lobes. Metastasis formation in this model is observed in 90–100% of the mice. Count the metastatic nodules on the surface of each of the lobes using a dissecting microscope, as described elsewhere[32]. Microscopic evaluation of lung tissue section is recommended to complement the macroscopic metastasis evaluation.

Troubleshooting advice can be found in table 1.

TABLE 1 | Troubleshooting table (continued).

Step	Problem	Possible reason	Solution
9	Tumor does not grow	Tumor cells are not viable	Repeat *in vitro* cell culture and counting. Keep the cells on ice during all procedures prior to implantation
10	Difficulty closing the hemostatic clamp	Clamp is too small for the size of the mouse	Use appropriate hemostatic clamps as described in the MATERIALS section
14	Wound bleeding after removal of the clamp	Incomplete closure of the clamp or too early removal	Re-apply the clamp and wait for another 5 min before proceeding to the next step
23	Inability to count metastatic nodules	Nodules are too numerous to count	Some tumor cell lines are extremely metastatic. Resect primary tumors at an earlier stage. However, a minimum size of 8 mm may be required for tumor metastases
		Nodules are difficult to detect	The metastatic nodules are usually clearly visible on the lung's surface without staining. However, to improve the visibility of nodules, lungs could be fixed in Bouin's fixative diluted 1:5 with neutral-buffered formalin. In addition, microscopic evaluation could be used to further quantify metastatic burden

TIMING

Selective depletion of human TAFs in mice

Steps 1–7, isolation of TAFs from human breast adenocarcinoma tissue: 3 months

Steps 8 and 9, coimplantation of TAFs and cancer cells in the hind limb of an immunodeficient mouse: 1.5 h

Steps 10–18, complete resection of the primary tumor by hind limb amputation: 30 min

Steps 19 and 20, selective depletion of human TAFs using an i.p. injection of DT: 15 min

Steps 21–23, collection of the lungs and evaluation of the metastatic burden: 30 min

Anticipated results

Typical results of the isolation of TAFs from human tissues are shown in Figure 2.

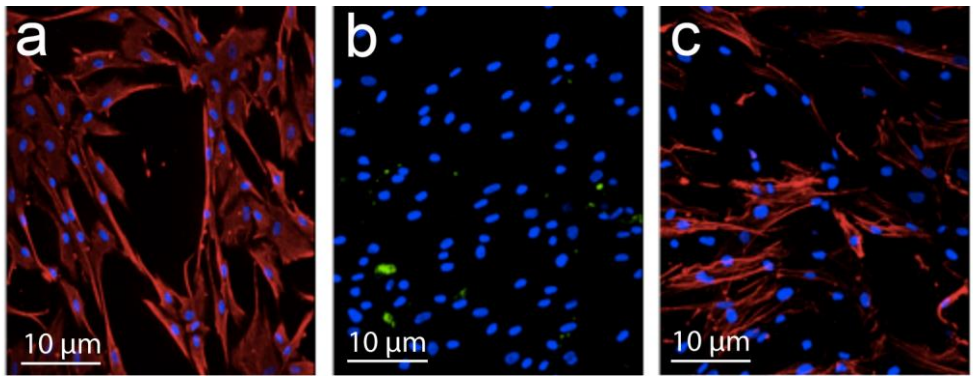

Figure 2 | Isolation of tumor-associated fibroblasts (TAFs) from breast cancer specimens. (a–c) Representative images of immunocytochemical staining for human vimentin (a), cytokeratin AE1-AE3 (b) and α-SMA (c), showing characteristic mesenchymal phenotype. Blue, DAPI nuclear stain (in a–c). Red, vimentin (in a) and α-SMA (in c). Images are 315 ∝m across.

Isolated cell lines were stained with vimentin to show their mesenchymal lineage (human breast cancer cells were used as a control). We confirmed this finding using immunocytochemical staining with pan-cytokeratin–specific AE1-AE3 antibodies to rule out epithelial cell contamination. Next, we confirmed that the TAFs are 'activated' myofibroblasts, in contrast to 'resting' skin fibroblasts and normal fibroblasts, isolated from breast tissue > 2 cm away from the tumor, which express lower levels of α-SMA. Finally, we used CD31 to rule out endothelial lineage of the isolated TAFs and normal fibroblasts. Human stromal cells could be coimplanted with tumor cells and be selectively depleted at a chosen time point. By immunostaining with anti-human vimentin antibody, which is specific for human cells—i.e., it does not stain mouse cells or tumor cells in this model—we showed incorporation of human TAFs in the primary tumor as well as their presence in the metastatic site[21] (Fig. 3a,b). The presence of human passenger TAFs in the lungs was confirmed by immunostaining for human nuclear antigen[21] (Fig. 3c). Furthermore, Figure 3 shows the results of TAF depletion during the metastatic process. When using the timelines as described above the primary tumor is allowed to grow to a

size that facilitates metastases formation. (No resection of the primary tumor or resection of tumors at a smaller size does not usually induce metastasis formation in this tumor model.) When the circulating stromal cells, as well as the stromal cells in the micrometastases, are depleted (after primary tumor removal) using DT, the outgrowth of micrometastases in the lung decreases significantly (Fig. 4a). Moreover, TAF depletion results in increased survival (Fig. 4b). Together, this indicates that the presence of stromal cells in circulating tumor fragments increases their viability and promotes metastatic seeding[21].

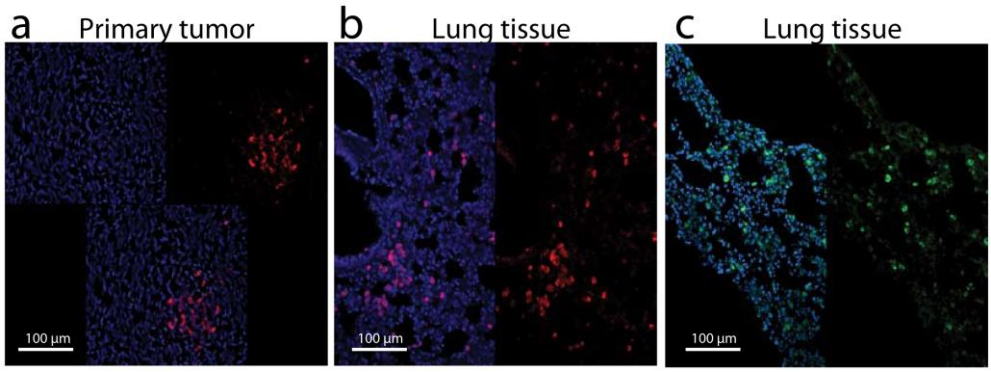

Figure 3 | Spontaneous metastasis of the passenger stromal cells in the coimplantation model. (a–c) Human CAFs coimplanted in the primary tumor site (a) and metastasizing to the lung (b,c). Immunohistochemical markers have been used to identify human cells using Cy3-labeled antihuman vimentin antibody (a,b) and FITC-labeled antihuman nuclear antigen antibody (c). Images are 700 µm across. Reproduced with permission from ref. 21. All animal procedures were performed according to the guidelines of public health service policy on humane care of laboratory animals, and in accordance with an approved protocol by the institutional animal care and use committee of MGH.

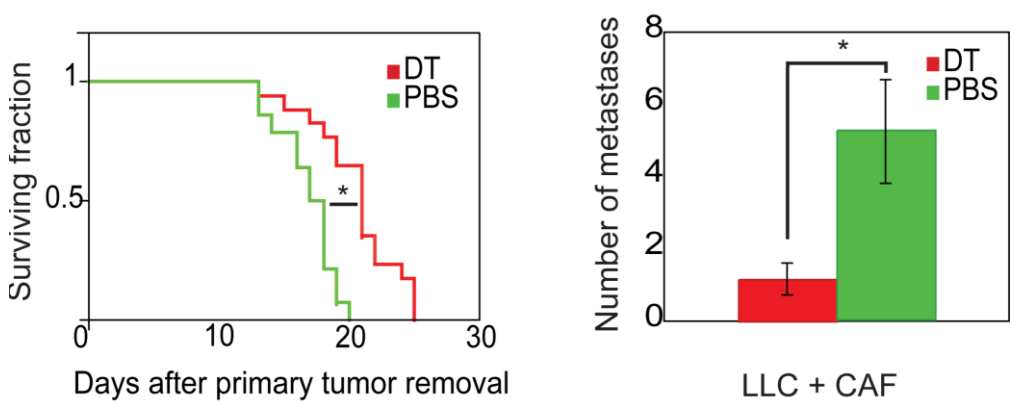

Figure 4 | Contribution of circulating stromal cells to spontaneous tumor metastases. (a,b) Selective depletion of stromal cells in the circulating fragments using DT results in prolonged survival (survival experiment in a) and a decrease in the number of lung metastases (time-matched evaluation in b). *P < 0.05. Reproduced with permission from ref. 21. All animal procedures were performed according to the guidelines of public health service policy on humane care of laboratory animals and in accordance with an approved protocol by the institutional animal care and use committee of MGH.

References

1. Bhowmick NA, Chytil A, Plieth D, et al. TGF-beta signaling in fibroblasts modulates the oncogenic potential of adjacent epithelia. *Science.* Feb 6 2004;303(5659):848-851.

2. Bhowmick NA, Neilson EG, Moses HL. Stromal fibroblasts in cancer initiation and progression. *Nature.* Nov 18 2004;432(7015):332-337.

3. Elenbaas B, Spirio L, Koerner F, et al. Human breast cancer cells generated by oncogenic transformation of primary mammary epithelial cells. *Genes Dev.* Jan 1 2001;15(1):50-65.

4. Jacobs TW, Byrne C, Colditz G, Connolly JL, Schnitt SJ. Radial scars in benign breast-biopsy specimens and the risk of breast cancer. *N Engl J Med.* Feb 11 1999;340(6):430-436.

5. Kalluri R, Zeisberg M. Fibroblasts in cancer. *Nat Rev Cancer.* May 2006;6(5):392-401.

6. O'Connell JT, Sugimoto H, Cooke VG, et al. VEGF-A and Tenascin-C produced by S100A4+ stromal cells are important for metastatic colonization. *Proc Natl Acad Sci U S A.* Sep 20 2011;108(38):16002-16007.

7. Olumi AF, Grossfeld GD, Hayward SW, Carroll PR, Tlsty TD, Cunha GR. Carcinoma-associated fibroblasts direct tumor progression of initiated human prostatic epithelium. *Cancer Res.* Oct 1 1999;59(19):5002-5011.

8. Orimo A, Gupta PB, Sgroi DC, et al. Stromal fibroblasts present in invasive human breast carcinomas promote tumor growth and angiogenesis through elevated SDF-1/CXCL12 secretion. *Cell.* May 6 2005;121(3):335-348.

9. Tlsty TD. Stromal cells can contribute oncogenic signals. *Semin Cancer Biol.* Apr 2001;11(2):97-104.

10. Podsypanina K, Du YC, Jechlinger M, Beverly LJ, Hambardzumyan D, Varmus H. Seeding and propagation of untransformed mouse mammary cells in the lung. *Science.* Sep 26 2008;321(5897):1841-1844.

11. Deventer K, Pozo OJ, Van Eenoo P, Delbeke FT. Development and validation of an LC-MS/MS method for the quantification of ephedrines in urine. *J Chromatogr B Analyt Technol Biomed Life Sci.* Feb 1 2009;877(4):369-374.

12. Hiratsuka S, Nakamura K, Iwai S, et al. MMP9 induction by vascular endothelial growth factor receptor-1 is involved in lung-specific metastasis. *Cancer Cell.* Oct 2002;2(4):289-300.

13. Kaplan RN, Riba RD, Zacharoulis S, et al. VEGFR1-positive haematopoietic bone marrow progenitors initiate the pre-metastatic niche. *Nature.* Dec 8 2005;438(7069):820-827.

14. Kim S, Takahashi H, Lin WW, et al. Carcinoma-produced factors activate myeloid cells through TLR2 to stimulate metastasis. *Nature.* Jan 1 2009;457(7225):102-106.

15. Al-Mehdi AB, Tozawa K, Fisher AB, Shientag L, Lee A, Muschel RJ. Intravascular origin of metastasis from the proliferation of endothelium-attached tumor cells: a new model for metastasis. *Nat Med.* Jan 2000;6(1):100-102.

16. Fidler IJ. The relationship of embolic homogeneity, number, size and viability to the incidence of experimental metastasis. *Eur J Cancer.* Mar 1973;9(3):223-227.

17. Fidler IJ. The pathogenesis of cancer metastasis: the 'seed and soil' hypothesis revisited. *Nat Rev Cancer.* Jun 2003;3(6):453-458.

18. Liotta LA, Saidel MG, Kleinerman J. The significance of hematogenous tumor cell clumps in the metastatic process. *Cancer Res.* Mar 1976;36(3):889-894.

19. Ruiter DJ, van Krieken JH, van Muijen GN, de Waal RM. Tumour metastasis: is tissue an issue? *Lancet Oncol.* Feb 2001;2(2):109-112.

20. Sahai E. Illuminating the metastatic process. *Nat Rev Cancer.* Oct 2007;7(10):737-749.

21. Duda DG, Duyverman AM, Kohno M, et al. Malignant cells facilitate lung metastasis by bringing their own soil. *Proc Natl Acad Sci U S A.* Nov 22 2010.

22. Duyverman AM, Kohno M, Duda DG, Jain RK, Fukumura D. A transient parabiosis skin transplantation model in mice. *Nat Protoc.* Apr 2012;7(4):763-770.

23. Duyverman AM, Kohno M, Roberge S, Fukumura D, Duda DG, Jain RK. An isolated tumor perfusion model in mice. *Nat Protoc.* Apr 2012;7(4):749-755.

24. Arbiser JL, Raab G, Rohan RM, et al. Isolation of mouse stromal cells associated with a human tumor using differential diphtheria toxin sensitivity. *Am J Pathol.* Sep 1999;155(3):723-729.

25. Padera TP, Stoll BR, Tooredman JB, Capen D, di Tomaso E, Jain RK. Pathology: cancer cells compress intratumour vessels. *Nature.* Feb 19 2004;427(6976):695.

26. Dawson MR, Duda DG, Fukumura D, Jain RK. VEGFR1 activity-independent metastasis formation. *Nature.* 2009:(in press).

27. Hiratsuka S, Duda DG, Huang Y, et al. C-X-C receptor type 4 promotes metastasis by activating p38 mitogen-activated protein kinase in myeloid differentiation antigen (Gr-1)-positive cells. *Proc Natl Acad Sci U S A.* Jan 4 2011;108(1):302-307.

28. Padera TP, Kadambi A, di Tomaso E, et al. Lymphatic metastasis in the absence of functional intratumor lymphatics. *Science.* Jun 7 2002;296(5574):1883-1886.

29. Tian B, Han L, Kleidon J, Henke C. An HSV-TK transgenic mouse model to evaluate elimination of fibroblasts for fibrosis therapy. *Am J Pathol.* Aug 2003;163(2):789-801.

30. Kassen A, Sutkowski DM, Ahn H, Sensibar JA, Kozlowski JM, Lee C. Stromal cells of the human prostate: initial isolation and characterization. *Prostate.* Feb 1996;28(2):89-97.

31. Mazzocca A, Dituri F, Lupo L, Quaranta M, Antonaci S, Giannelli G. Tumor-secreted lysophostatidic acid accelerates hepatocellular carcinoma progression by promoting differentiation of peritumoral fibroblasts in myofibroblasts. *Hepatology.* Jun 14 2011.

32. Welch DR. Technical considerations for studying cancer metastasis in vivo. *Clin Exp Metastasis.* May 1997;15(3):272-306.

Chapter 5

Malignant cells facilitate lung metastasis by bringing their own soil

Annique MMJ Duyverman[1]

Dan G.Duda[1]

Mitsutomo Kohno[1]

Sylvie Roberge

Dai Fukumura

Dan G Duda

Rakesh K Jain

[1] These authors contributed equally to this work

Edwin L. Steele Laboratory for tumor Biology, Department of Radiation Oncology, Massachusetts General Hospital and Harvard Medical School, Boston, USA

Proc Natl Acad Sci U S A. 2010 Dec 14;107(50):21677-82

Abstract

Metastatic cancer cells (seeds) preferentially grow in the secondary sites with a permissive microenvironment (soil). Here, we show that the metastatic cells can bring their own soil – from the primary site – stromal components including activated fibroblasts to the lungs. By analyzing the efferent blood from tumors we found that viability of circulating metastatic cancer cells is higher if they are incorporated in heterotypic tumor-stroma cell fragments. Moreover, we show that these co-traveling stromal cells provide an early growth advantage to the accompanying metastatic cancer cells in the lungs. Consistent with this hypothesis, we demonstrated that partial depletion of the carcinoma-associated fibroblasts, which spontaneously spread to the lung tissue along with metastatic cancer cells, significantly decreased the number of metastases and extend survival after primary tumor resection. Finally, we show that metastases the brain metastases from lung and other carcinomas in patients contain carcinoma-associated fibroblasts, in contrast to primary brain tumors or normal brain tissue. Demonstration of the direct involvement of primary tumor stroma in metastasis has important conceptual and clinical implications for the colonization step in tumor progression.

Introduction

Metastasis is a multi-step process in which metastatic cancer cells must invade the surrounding stroma, intravasate, survive in the circulation, arrest, extravasate, invade the matrix, and grow in the target organ– all while evading destruction by the immune system [1]. One possible mechanism by which metastatic tumors may create a “congenial” soil in the secondary site and facilitate growth in the new organ environment is to prepare “pre-metastatic site” by tumor-secreting factors [2-4]. We have previously shown that "passenger" stromal cells contained in the original tumor source survive and proliferate during the initial growth of tumor fragments implanted in a new host [5]. Here, we propose that the metastatic tumor cells bring "passenger" stromal cells from the primary tumor to the secondary site in the same host to provide a provisional stroma and facilitate initial growth and metastasis formation. Studies reported more than thirty years ago showed that cancer cell clumping in circulation increases metastasis [6, 7]. These clumps may be emboli, formed in circulation due to interactions with immune cells [8-10]. Indeed, injection of emboli containing both tumor and non-tumor cells increases the efficiency of metastasis [6, 11]. To test the hypothesis that metastatic cancer cells can bring their own soil to form metastases, we set out to answer five sequential questions. Do metastatic tumors shed heterotypic tumor fragments, and if so, is the viability of circulating cancer cells is higher in heterotypic fragments? Could stromal cells in heterotypic fragments survive, proliferate and facilitate early metastatic growth in the lungs? What type of stromal cells from the primary tumors could be detected in metastases spontaneously formed after primary tumor resection? Could the selective depletion of primary tumor-derived stromal cells affect the spontaneous metastasis formation? And lastly, are primary-tumor associated stromal cells present in metastatic tumors in patients?.

Results

Viability of circulating metastatic cancer cells is higher in heterotypic tumor fragments.

Tumors shed both single cells as well as clumps into the blood circulation. To establish if the circulating clumps (circulating fragments consisting of at least two cancer cells) contain tumor-derived stromal cells (e.g., fibroblasts, endothelial or tumor-infiltrated myeloid cells), we first implanted ds-Red-expressing metastatic Lewis lung carcinoma cells (LLC1) under the renal capsule in mice ubiquitously expressing the green fluorescent protein (GFP)– *Actb-GFP*/C57BL/6 mice, referred heretofore as *Actb-GFP* mice. When tumors reached 9-10 mm in diameter, we performed an isolated tumor perfusion to collect and analyze the content of the efferent blood from the tumor [12, 13] (Figure 1a). The vast majority (~81%) of the shed ds-Red$^+$ cancer cells were single cells (Figure 1b). However, we also collected small tumor clumps (≤ 200μm in diameter), and all tumor clumps composed of six or more cells contained GFP-expressing host cells (Figure 1b,c and Supplementary Table S1). At the time of shedding, caspase 3 and 7 activation – a measure of apoptosis – was detectable in most of the single or doublets of cancer cells and only 12.0 ± 4.1% was viable. In contrast, the heterotypic-cell clumps contained almost twice as many viable cancer cells (22.8 ± 4.5%, $p < 0.05$; see Figure 1d).

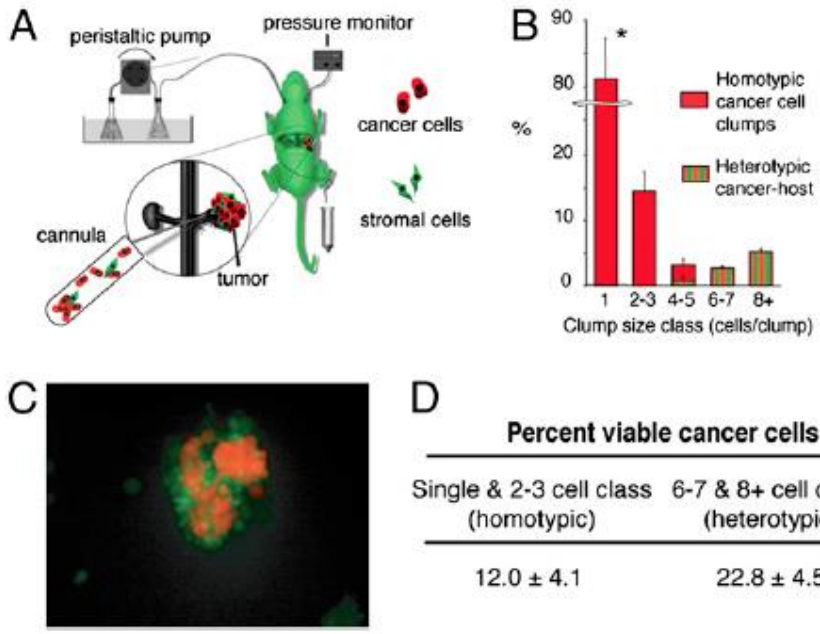

Figure 1| Tumors shed fragments containing viable cancer cells in blood circulation. (a) Schema of the tumor perfusion and blood collection setup: ds-Red-LLC1 tumors were grown in the kidney of mice ubiquitously expressing GFP, and tumor perfusate was collected by cannulating the efferent vein (renal vein). (b) Histogram of the composition of shed tumor cells/clumps obtained from the renal perfusion experiment (n=5 mice). The majority of shed cancer cells were single or doublets. Host-derived GFP^+ cells were present in all large clumps consisting of more than 4-5 cells. (*$p < 0.05$.) (c) Representative fluorescence multi-photon laser scanning microscopy image of a heterogeneous clump, shed by a tumor using the isolated renal perfusion model. (green: stromal cells, red: tumor cells). (d) Viability of the shed cells and clumps using caspase staining: Over 22% of the ds-Red^+ cancer cells within heterotypic (cancer + host cells) clumps were negative for caspase 3 and 7, while only 12% of the cancer cells collected as single cells or in homotypic clumps were viable ($p < 0.05$). Data are expressed as mean ± SD of four independent experiments.

Tumor fragments may increase early metastatic tumor growth by carrying over primary tumor stroma in the lungs in an experimental metastasis model

Clumps of cancer cells exhibit increased metastatic efficiency, even when viable cells are clumped with dead cells [7]. Thus, we first sought to determine if the host-derived "passenger" cells survive in circulation and are involved in metastatic tumor growth in the lungs. To this end, we intravenously injected in wild-type non-GFP C57BL/6 mice,

fluorescent tumor fragments (40-100μm in diameter) obtained by mechanical dissociation of ds-Red-LLC1 tumors grown in *Actb-GFP* mice. In this experimental metastasis model, GFP^+ host-derived "passenger" cells survived and were detectable in ds-Red^+ lung metastatic nodules after two weeks, as determined by whole-mount fluorescence microscopy (Figure 2a). Similar results were obtained using another metastatic lung carcinoma line (LA-P0297) and syngeneic *EF1α-GFP*/FVB mice (data not shown). Whereas not all initial micrometastatic foci eventually formed established metastases, a substantial number of metastatic nodules formed over first two weeks, and their mean diameter increased progressively (Figure 2b). Of interest, the number of GFP^+ host-derived cells per nodule (in nodules that contained GFP^+ cells) increased significantly over the first 7 days of growth (Figure 2c). Moreover, whereas the number of metastatic foci decreased with time, number of foci with GFP+ host cells remained constant. As a result, at day 7, the fraction of metastatic nodules that contained GFP^+ stromal cells became significantly higher as compared to that of the initial foci formed at day 1 after intravenous injection of the fragments (Figure 2d). These data indicate that stromal cells associated with the primary tumor are involved in the metastatic nodules and survive and proliferate at the secondary site during early growth of metastatic foci. They also suggest that metastatic foci that contain primary tumor-derived stromal cells have a survival advantage.

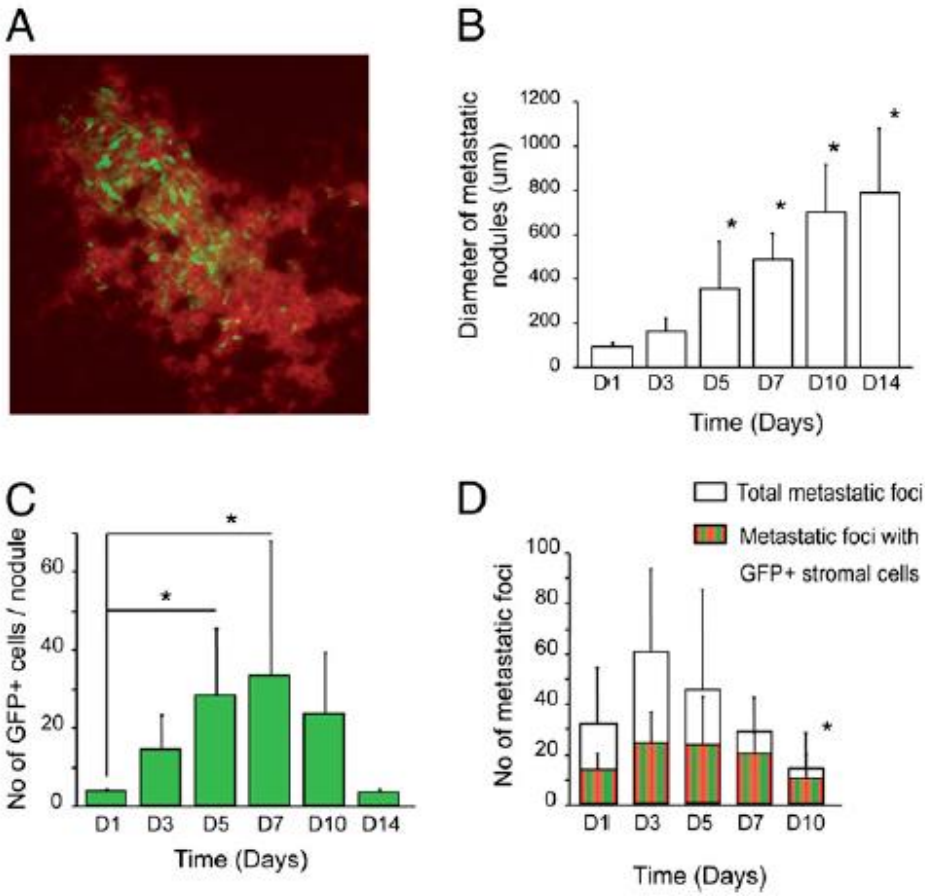

Figure 2| "Passenger" stromal cells survive and promote initial growth after i.v. infusion of tumor fragments. (a) Multiphoton microscopy image (630μm across) of GFP⁺ primary tumor-derived stromal cells in a lung metastatic nodule in a C57BL/6 mouse one week after i.v. infusion of *DsRed*-LLC1 tumor clumps obtained from a tumor growing in a *Actb-GFP* mouse. (b) The mean diameter of metastatic nodules increased significantly over time (*$p < 0.05$ versus day 1). (c) The number of GFP⁺ cells per metastatic nodule significantly increased from day 1 to days 5-7 (*$p < 0.05$ versus day 1, n = 4-5 mice). GFP⁺ cells are detectable for up to two weeks in the macropscopic metastases. (d) The presence of GFP⁺ host cell in the initial metastases appears to provide a growth advantage: The ratio of foci with host cells increases from approximately 40% on day 1 to 70-80% around day 7-10 (*$p < 0.05$ versus day 1). After day 10, there is a "dilution" in GFP⁺ stromal cells (a decrease of the ratio to 35%), likely due to infiltration of the foci by non-GFP host-derived stromal cells.Stromal cells from primary tumors are detectable in metastatic nodules spontaneously formed in the lungs after primary tumor resection.

Stromal cells from primary tumors are detectable in metastatic nodules spontaneously formed in the lungs after primary tumor resection

To characterize the stromal cells that spontaneously "metastasize" with cancer cells, we adapted a parabiosis mouse model [14] to create a mouse with a 2-cm graft of GFP^+ skin and subcutaneous tissue. This procedure allowed us to generate a primary tumor with a rich GFP^+ stromal cell infiltration in a wild-type (non-GFP) C57BL/6 mouse (see Figure 3a-c and Methods). We tansplanted non-GFP LLC1 tumor cells in the GFP+ skin and allowed the tumor to reach a diameter of 8 mm prior to resection. Three weeks after primary tumor resection, we studied grossly apparent lung metastases (arising from spontaneous foci formed prior to resection). In concert with the variability in GFP^+ cell number in the primary tumors (not shown), GFP^+ cells (i.e., primary tumor stroma-derived cells) were detectable in 27-86% of lung metastases. We used several different markers to characterize the GFP^+ cells by immunohistochemistry, given the known lack of marker specificity for stromal cells. We detected co-localization of GFP with expression of α-smooth muscle actin (αSMA) in 80% and of fibroblast-specific protein 1 (FSP1) in 75% of the stromal cells carried over to the lungs – both are indicative of the mesenchymal lineage (Figure 3d,e). In contrast, co-localization of GFP with F4/80 (a macrophage-selective marker) was detectable in 28% of the stromal cells (data not shown).

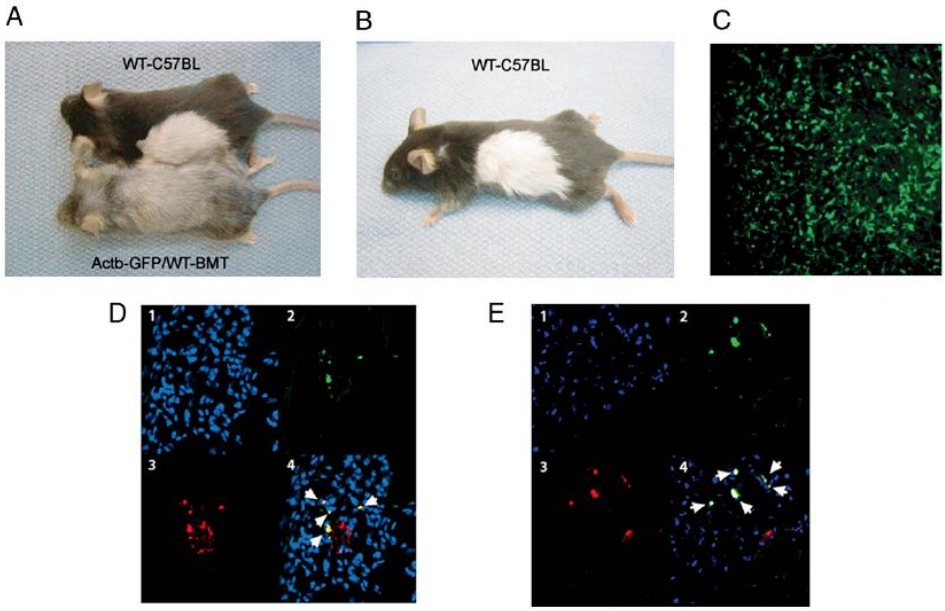

Figure 3 | Characterization of "passenger" stromal cells in a spontaneous metastasis formation model. (a,b) Transient parabiosis and bone marrow transplantation. Transient parabiosis model using C57BL/6 and *Actb-GFP*/WT-BMT mice (a). Fur de-pigmentation in *Actb-GFP*/WT-BMT mouse is secondary to the whole body irradiation (b). (c) Representative multiphoton microscopy image of a LLC1 tumor grown in a successful GFP$^+$ skin graft transplanted in a WT-C57BL mouse. The image is 630 μm across. (d, e) Phenotypic analysis of GFP$^+$ primary tumor-derived stromal cells in metastases by immunohistochemistry and confocal microscopy: GFP$^+$ cells frequently express αSMA (white arrows in d) and FSP1 (e). The subpanels are (1) blue, DAPI nuclear stain; (2) green, GFP; (3) red, Cy3-labeled antibody staining; and (4) merged image. Images are 280μm across.

Fibroblasts carried over from the primary tumor increase the efficiency of lung metastasis

Since fibroblasts were highly prevalent among the traveling stromal cells detectable in metastases, we next tested if their selective depletion in metastatic foci affects the metastatic growth. To this end, we used human carcinoma-associated fibroblasts and diphtheria toxin (DT) treatment (Supplementary Figure S1), because human cells are a 1000 times more sensitive to DT than murine cells and can be depleted by DT *in vivo* in mice [15, 16]. We first grew tumors by co-implantation of LLC1 cells with human CAFs in SCID mice. CAFs persisted in the growing tumors (Figure 4a), but did not affect their

growth rate (not shown). The spontaneous colonization of the implanted CAFs to the lungs was confirmed by immunostaining. To this end, we used two antibodies specific for human antigens (that do not cross-react with either mouse fibroblasts or tumor cells) in lung tissues collected three days post-amputation of the hindlimb bearing the tumor (Figure 4b,c). To specifically deplete the CAFs that colonized the lungs, we systemically administered DT to the tumor-bearing mice 1 day after complete resection of the primary tumors. DT treatment post-resection significantly increased the survival compared to control (PBS) treatment ($p<0.05$, Figure 4d), but only in mice in which the primary tumors were generated by co-implantation of LLC1 with CAFs and not in mice implanted with LLC1 cells alone (not shown). Moreover, when evaluated 2 weeks after resection, the lungs of DT-treated mice contained significantly fewer macroscopic metastases than those of mice treated with PBS ($p<0.05$, Figure 4e). We confirmed the decrease in number of metastatic nodules after CAF depletion post-resection using LA-P0297, another metastatic lung carcinoma cell line (Figure 4e). Of note, metastasis formation was not affected by the treatment with DT in mice implanted with cancer cells alone (Supplemental Figure S2). Finally, we sought to determine if CAF presence within the metastatic foci was critical for their promotion of metastatic growth. To this end, we intravenously injected single cell suspensions containing LLC1 and CAFs, a model in which cells randomly distribute throughout the lung terminal capillaries and venules. We depleted the CAFs by DT treatment at 24 hr after cell infusion. There was no significant difference in the number of metastases evaluated two weeks after infusion (not shown). These data show that tumor-associated fibroblasts can promote lung metastasis, and that this promotion may not occur when the CAFs are not in direct association with the cancer cells within metastatic foci.

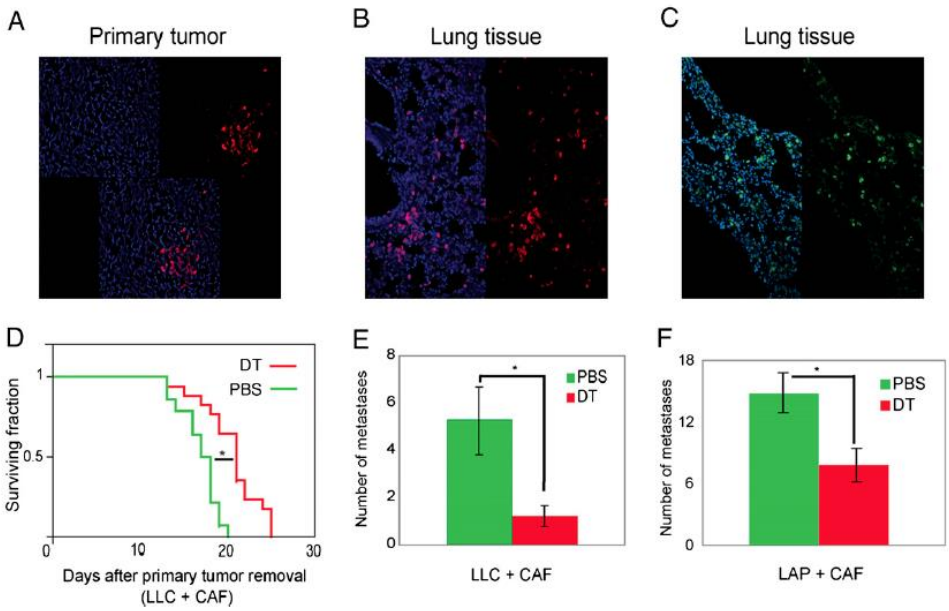

Figure 4| Carryover of primary tumor stromal cells in lung metastases increases metastasis formation and survival. (a-c) Representative confocal microscopy images of primary tumors generated by co-implatation of human CAFs with LLC1 cells confirming the persistence of CAFs in 5-mm tumors (a), as well as CAF presence in the lungs after primary tumor resection (b,c). Blue; DAPI nuclear stain, red; Cy3 labeled anti-human vimentin, green; FITC-labeled anti-human HLA. Images are 700 μm across. (d) Survival in mice with LLC1 metastases. CAF depletion using systemic DT treatment *after tumor resection* significantly increased survival (*$p < 0.001$ as compared to PBS control, n = 11-17 mice). (e,f) CAF depletion by DT treatment after tumor resection significantly reduced the number of spontaneous macrometastases in LLC1 (e) and LA-P0297 (f) models (*$p < 0.05$ as compared to PBS control, n = 11-12 mice).

Tumor-associated fibroblasts are detectable in human carcinoma metastases to the brain, but not in primary brain tumors

We next sought to establish clinical relevance of the primary tumor-associated fibroblasts in metastasis. To this end, we examined brain metastases of patients with a variety of tumors. Brain metastasis is an ideal setting to detect primary tumor-derived stromal cells such as CAFs since normal brain tissue does not contain fibroblasts. We performed immunostaining for aSMA in human samples of brain metastases from carcinomas of the lung, breast, kidney or endometrium, and used normal brain and primary malignant brain tumors (i.e., glioblastoma) as a control. The only cells that stained positive for aSMA in normal brain and glioblastoma tissues were blood vessel associated pericytes and smooth muscle cells (Figure 5a). In contrast, we frequently detected benign appearing $aSMA^+$ stromal cells with typical fibroblast spindle shape appearance distributed focally within the brain metastases in the extra-vascular area of the vast majority of cases (Figure 5b-e). Moreover, we detected by immunohistochemistry $CD10^+$ cells– a specific marker of endometrial stroma – in a rare case of endometrial carcinoma metastasis to the brain (Figure 5f). Collectively, these results provide compelling evidence for the presence and potential direct involvement of primary tumor-associated fibroblasts in metastasis in cancer patients.

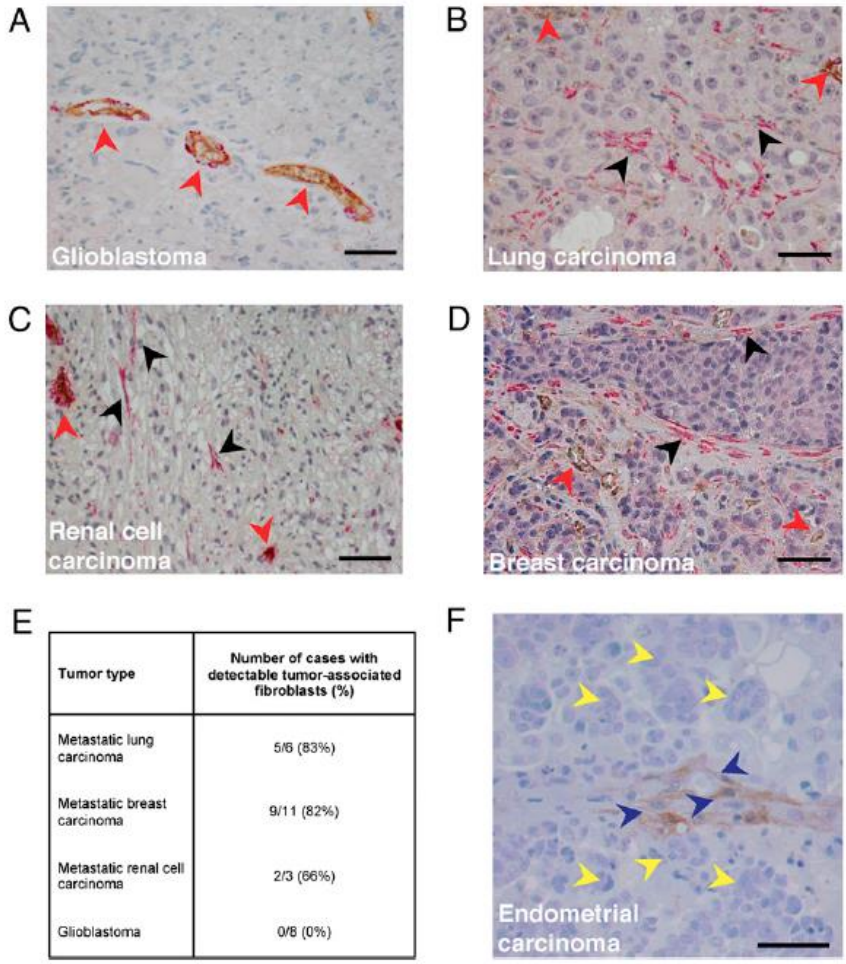

Tumor type	Number of cases with detectable tumor-associated fibroblasts (%)
Metastatic lung carcinoma	5/6 (83%)
Metastatic breast carcinoma	9/11 (82%)
Metastatic renal cell carcinoma	2/3 (66%)
Glioblastoma	0/8 (0%)

Figure 5| Clinical evidence for carryover of primary tumor stromal cells in human metastases. (a) Representative microscopy image of glioblastoma tissue. Red arrows indicate tumor vessels after αSMA/CD31 double staining. In normal human brain and primary brain tumors, only vessel associated pericytes and vascular smooth muscle cells are αSMA-positive. (b-d) Representative microscopy images of human brain metastases originating from lung carcinoma (**b**), renal cell carcinoma (**c**), and breast carcinoma (**d**). Red arrows indicate αSMA-positive perivascular cells associated with CD31-positive vascular endothelial cells. Black arrows indicate focal presence of αSMA-positive tumor-associated fibroblasts. (**e**) Quantification of cases of human brain metastasis with detectable tumor-associated fibroblasts. (**f**) Representative microscopy image of human brain metastasis from endometrial carcinoma: Endometrial stromal cells (CD10+ cells, blue arrows) are detectable in the brain in close association with the cancer cells (yellow arrows). Scale bar corresponds to 50 μm.

Discussion

Recent studies have shown that the efficiency of the metastatic process may be increased by various factors related to host-derived stroma. In experimental metastasis models, it has been shown that metastatic cells could lodge in the lungs prior to their oncogenic transformation [17], or could home to sites where immune cells or fibrocytes accumulate and promote metastatic growth [2-4, 18]. It has also been shown that metastatic cells could form intravascular colonies in the lungs, and subsequently invade the organ [19]. In addition, there is mounting evidence that the stromal compartment plays an important role in tumor progression and metastasis. Previously, it has been known that cancer cell clumping in circulation increases the metastasis efficiency. Here we show that host-derived stromal cells can directly contribute to the lung metastasis when carried-over from the primary site within tumor fragments. Our data indicate that tumor-associated stromal cells shed from the primary tumor together with accompanying cancer cells, survive in blood circulation as well as the secondary site and proliferate within the metastatic nodules. Pre-existence of a tissue-like structure containing fibroblasts in clumps may increase the viability of cancer cells in blood circulation and the secondary site. The roles of travelling stromal cells are likely to be more significant at the early stage of metastatic foci growth as their participation may be transient [5]. Furthermore, we report that this novel mechanism of metastatic cell colonization in the lungs can increase cancer's metastatic efficiency.

The ectopic presence of tumor-associated fibroblasts in brain metastases in patients indicates a potential clinical relevance of this phenomenon, which should be also explored further in future studies. It would be of great interest to demonstrate if and how neoadjuvant (pre-operative) therapies of primary tumors affect this process and if evaluating circulating tumor clumps could complement circulating tumor cells studies. In particular, identifying the adhesion molecules that are responsible for the adherence between the cancer cells and fibroblasts may provide new targets for anti-metastasis therapy. In what aspect this mechanism contributes to the organo-tropism of certain metastatic tumors is also unclear. Nevertheless, demonstration of the possible

involvement of the same tumor “soil” in both local and distant lesions has important conceptual implications for the colonization step of metastatic cascade.

Materials and Methods

Cells and gene transfections

We used two cell lines with established metastatic potential [20-22]. Lewis lung carcinoma (LLC-1) cells were purchased from ATCC (Manassas, VA). Another metastatic lung cancer cell line (LA-P0297) was established from spontaneous tumors that arose in FVB mice in our laboratory [21]. The cancer cells have a mean diameter of 20μm. All cells were maintained in DMEM supplemented with 10% fetal bovine serum. For some of the experiments, the cancer cells were transfected with *dsRed* using a retroviral vector (pMOWSdSV4.0-DsRED express, a kind gift from Dr. Brian Seed, Massachusetts General Hospital, Boston, MA). Carcinoma associated fibroblasts (CAFs) and the CAF isolation protocol were generously provided by Dr. R. Weinberg (Whitehead Institute and Massachusetts Institute of Technology, Cambridge, MA). We isolated CAFs from human breast cancer tissue obtained from the Department of Surgery at Massachusetts General Hospital and maintained cells in DMEM (ATCC) supplemented with 10% calf serum.

Animals

C57BL/6 mice expressing GFP under the chicken beta-actin promoter and cytomegalovirus (CMV) enhancer (*Actb-GFP*) were purchased from Jackson Laboratories (Bar Harbor, ME) and then re-derived, bred, and maintained in our animal facility. Wild-type (non-GFP) C57BL/6 and severe combined immunodeficient (SCID) mice were also bred and maintained in our gnotobiotic animal facility. All animal procedures were performed following the guidelines of Public Health Service Policy on Humane Care of Laboratory Animals and in accordance with an approved protocol by the Institutional Animal Care and Use Committee of Massachusetts General Hospital.

Tumor perfusion and efferent blood collection

Male *Actb-GFP* mice, 6-10 weeks of age were used for a kidney-isolated tumor perfusion model as previously described [23, 24]. 1 x 10^6 *DsRed*-LLC1 cells were injected under the capsule of the kidney. Tumors were allowed to grow for 10-12 days. To collect shed cancer cells and clumps, the renal vein of the left kidney, was cannulated, 3-4 ml of perfusate was collected and passed through a polycarbonate membrane filter (8 µm pore size) (Sterlitech, Kent, WA). Cytological elements retained on the filter were analyzed quantitatively by fluorescence multiphoton laser-scanning microscopy for the presence of ds-Red$^+$ positive cancer cells and GFP$^+$ host cells.

Apoptosis assay

To evaluate the viability of shed cancer cells, we used the Carboxyfluorescein Caspase 3 FLICA (Immunochemistry Technologies, Bloomington, MA) according to the manufacturer's protocol. C57BL/6 mice were inoculated with *DsRed*-LLC1 cells in the kidney and the shed cells were collected as described above. We detected caspase 3 and 7 activities (detected as green fluorescence signal) by fluorescence confocal microscopy.

Experimental lung metastasis using tumor fragment infusion

Male SCID mice, 8-10 weeks of age were used for the experimental lung metastases model. *Ds-Red*-LLC1 tumors grown in *Actb-GFP* mice, were mechanically dissociated and serially filtered through 100 and 40µm cell strainers (BD Biosciences, San Jose, CA). Tumor fragments were recovered and infused in non-transgenic C57BL/6 mice at a concentration of approximately 2,000 to 3,000 of fragments per 0.4 ml iv. On days 1, 3, 5, 7, 10 and 14 after tumor fragment infusion, lung metastases were counted on whole tissue mounts. In all foci, the number of GFP$^+$ stromal cells was quantitatively analyzed in images captured by fluorescence multi-photon laser-scanning microscopy. This experiment was repeated using another lung carcinoma cell line LA-P0297 and syngeneic FVB mice ubiquitously expressing GFP (*EF1a-GFP* transgenic mice).

Bone marrow transplantation (BMT)

Restorative BMT to mice that had been lethally irradiated using a dose of 2 x 6 Gy was performed as previously described [20].

Skin graft from BMT mice through parabiosis

To detect tumor host-derived cells in lung metastases, we engrafted *Actb-GFP* skin to a wild-type C57BL/6 mouse through the parabiosis procedure (i.e., by surgically conjoining the mice from the shoulder to the hip to share a common circulation). Two months prior to the surgical procedure, *Actb-GFP* received a restorative BMT from wild-type C57BL/6 mice (*Actb-GFP*/WT-BMT). The mice were kept in parabiosis with syngeneic C57BL/6 mice for three weeks and then surgically separated. After surgery, a 2 cm flap of the skin and subcutaneous tissues were transferred from the *Actb-GFP*/WT-BMT mice and sutured on the C57BL/6 mice. Before s.c. tumor inoculation in these mice we confirmed (i) the absence of hematopoietic GFP^+ cells in circulation and in digested lung tissue by flow cytometry; and (ii) the lack of αSMA^+GFP^+ and $FSP1^+GFP^+$ cell presence in the lung tissues by flow cytometry and immunohistochemistry (data not shown). One million LLC1 cells were subcutaneously inoculated in the engrafted skin area. Tumors were resected when they reached 8 mm in diameter and primary tumors were analyzed for GFP^+ cell content. Because of significant incorporation of non-GFP cells in the primary tumors, the fraction of GFP+ vs non-GFP cells varied from mouse to mouse. Thus, for the phenotypic analysis, we included only the mice that had detectable levels of GFP^+ cell recruitment in the primary tumors (5 of 7 mice; 71%).

Spontaneous lung metastasis formation after primary tumor resection

Male SCID mice, 8-10 weeks of age were co-implanted subcutaneously with 2 x 10^5 LLC1 (or LA-P0729) tumor cells and 1 x 10^6 human CAFs in 0.1 ml of PBS (i.e., at a 1:5 ratio). For primary tumor growth experiments, tumors were allowed to grow to a size of 5 mm, before they were treated with 0.2 ml of Diphtheria Toxin 1 μg/ml (DT, Sigma, St. Louis, MO). In the spontaneous metastasis formation models, tumors were allowed to grow to a size of 10 mm before they were resected. One day after primary tumor resection, mice

were treated with 0.2 ml of DT at a dose of 1μg/ml or PBS as a control. In pilot studies, we found that systemic DT treatment at this dose was effective in delaying tumor growth after s.c. injection of CAFs with LLC1 cells but not after s.c. injection of LLC1 cells alone (not shown). Mice were sacrificed when they showed signs of advanced disease (weight loss > 15%, ruffled fur and/or cachexia). Survival time distributions were analyzed using Kaplan-Meier plots. The number of macroscopic metastases per lung was counted using a dissecting microscope.

Tissue preparation and fluorescence immunohistochemistry

Mice were perfusion fixed by infusion of 4% paraformaldehyde through the left ventricle and lungs were post-fixed for 2 hours in 4% paraformaldehyde followed by overnight incubation in 30% sucrose in PBS at 4°C and subsequent embedding in freezing media. 10-20 μm tissue sections were counterstained using the nuclear dye DAPI and analyzed for GFP expression. For immunohistochemical characterization of stromal cells and detection of (human) CAFs, tissue sections were stained using anti-F4/80, anti-αSMA and anti-FSP1 (S100A4) antibodies. Tissue sections were incubated (i) 24 hr at 4°C with biotin-conjugated anti-F4/80 antibodies (Serotec, Raleigh, NC) followed by 1 hr incubation with a 1:200 dilution of Cy3-conjugated streptavidin (Molocular Probes, Eugene, OR); (ii) 2 hr at room temperature using a primary Cy3-conjugated anti-mouse αSMA antibody (Sigma, St Louis, MO); or (iii) 24 hr at 4°C using a rabbit polyclonal anti-FSP1 (Abcam, Cambridge, MA) followed by 1 hr incubation at room temperature with a Cy3-conjugated anti-rabbit antibody (Jackson Immunoresearch, PA). For human CAF identification, tissues were incubated for 30 min at room temperature using the monoclonal mouse, anti-human Vimentin clone 3B4 antibody (#M7020, DAKO, Carpinteria CA), or incubated 1 hour at 37°C using a monoclonal mouse anti-human HLA-ABC antigen Clone W6/32 (#R7000, DAKO) both followed by 1 hr incubation at room temperature with a FITC-labeled anti-mouse antibody. Tissues were mounted using DAPI containing mounting media.

Immunohistochemical analysis of brain metastases from carcinoma and glioblastoma patients

Formalin fixed paraffin-embedded brain tumor tissue from patients with glioblastoma, metastatic lung, breast, renal cell and endometrial carcinoma were obtained from the Department of Pathology, Massachusetts General Hospital. Each case was reviewed by a trained neuro-pathologist (MS). Tissues were stained using a CD31/αSMA double staining protocol. We used prediluted CD31 antibody (#N1596, DAKO) for 1 hr at room temperature, antigen detection was performed using Mouse EnVision Polymer. Next, sections were incubated with anti-αSMA 1:5000 (cat M0850, Sigma) in 5% NHS/PBS overnight at 4°C and double-stain Alkaline Phosphatase polymer (DAKO) was used to retrieve the antigen for 30 min at room temperature. Tissues were counterstained using hematoxylin and coverslipped with Faramount fixation. Immunostaining for CD10 was performed using anti-CD10 antibody (IgG_1 isotype; clone 56c6, prediluted, Ventana Medical Systems, AZ) on BenchMark XT automated tissue staining systems (Ventana Medical Systems) followed by incubation with *UltraView* HRP-conjugated multimer antibody reagent (Igs; Ventana Medical Systems). Antigen detection was performed using *UltraView* diamino-benzidine chromogen (Ventana Medical Systems). Tissues were counterstained with Hematoxylin.

Quantification of confocal images

Co-localization of αSMA, FSP1 and F4/80 expression with GFP^+ in stromal cells was quantified using fluorescence confocal microscopy (n=6 mice, 5-6 sections each). The size of all the images analyzed was 1024 x 1024 pixels.

Cell Lines and PCR Array

Lewis lung carcinoma (LLC-1) cells were purchased from ATCC. Another metastatic lung cancer cell line
(LA-P0297) was established from spontaneous tumors that arose in FVB mice in our laboratory (1). The cancer cells have a mean diameter of 20 μm. We isolated carcinoma-associated fibroblasts (CAFs) from human breast cancer tissue obtained from the

Department of Surgery at Massachusetts General Hospital and maintained cells in DMEM (ATCC) supplemented with 10% calf serum. Total RNA samples were isolated from cultured CAFs using TRIzol (Invitrogen). Expression profile of 84 key genes was determined using Human Angiogenesis PCR array plate (SABiosciences).

Tissue Preparation and Fluorescence Immunohistochemistry

Mice were perfusion fixed by infusion of 4% paraformaldehyde through the left ventricle, and lungs were post fixed for 2 h in 4% paraformaldehyde, followed by overnight incubation in 30% sucrose in PBS at 4 °C and subsequent embedding in freezing media. For immunohistochemical characterization of GFP-positive stromal cells, tissue sections were stained using anti-F4/80, anti-αSMA(α-smooth muscle actin), and anti-FSP1 (fibroblast-specific protein 1) (S100A4) antibodies. Tissue sections were incubated (i)24h at 4 °C with biotin-conjugated anti-F4/80 antibodies (Serotec), followed by1-hincubation witha1:200 dilution ofCy3-conjugated streptavidin (Molecular Probes); (ii) 2 h at room temperature using a primary Cy3-conjugated anti-mouse α SMA antibody (Sigma); or (iii) 24 h at 4°C using a rabbit polyclonal anti-FSP1 (Abcam), followed by 1-h incubation at room temperature with a Cy3-conjugated anti-rabbit antibody (Jackson Immunor- esearch). For human CAF identification, tissues were incubated for 30 min at room temperature using the monoclonal mouse, anti-human vimentin clone 3B4 antibody (#M7020; DAKO), or incubated 1 h at 37 °C using a monoclonal mouse anti-human HLA-ABC antigen clone W6/32 (#R7000; DAKO), both followed by 1-h incubation at room temperature with an FITC-labeled anti-mouse antibody.

Immunohistochemical Analysis of Brain Metastases from Carcinoma and Glioblastoma Patients

H&E sections of each clinical case were reviewed by a trained neuropathologist (M.S.). The following morphological criteria were applied in identifying benign fibroblasts on H&E sections: spindle shape, low nuclear/cytoplasmic ration, even chromatin pattern, and absence of atypical mitotic figures. For CD31/αSMA double staining, the sections were incubated with prediluted CD31 antibody (#N1596; DAKO) for 1 h at room

temperature, and antigen detection was performed using Mouse EnVision Polymer. Next, sections were incubated with anti-αSMA 1:5,000 (catalog no. M0850; Sigma) in 5% NHS/PBS overnight at 4 °C, and double stain alkaline phosphatase polymer(DAKO) was used to retrieve the antigen for 30 min at room temperature. Tissues were counterstained using hematoxylin and coverslipped with Faramount fixation. Immunostaining for CD10 was performed using anti-CD10 antibody (IgG1 isotype; clone 56c6, prediluted; Ventana Medical Systems) on BenchMark XT automated tissue staining systems (Ventana Medical Systems), followed by incubation with UltraView HRP-conjugated multimer antibody reagent (Igs; Ventana Medical Systems). Antigen detection was performed using UltraView diamino-benzidine chromogen (Ventana Medical Systems).

Statistical Analysis

Data are expressed as mean ± SEM, and statistical analysis was performed using the Student's t test (two-tailed with unequal variance). For survival data analysis, we generated Kaplan-Meier plots (JMP, version 5.0.1.2, SAS, Cary, NC) with failure defined as the need to sacrifice animals due to signs of advanced metastatic disease. Statistical differences were calculated using Log-Rank test. For all analyses, a p value of less than 0.05 was considered statistically significant.

References

1. Talmadge JE, Fidler IJ. AACR centennial series: the biology of cancer metastasis: historical perspective. *Cancer Res.* Jul 15 2010;70(14):5649-5669.

2. Hiratsuka S, Nakamura K, Iwai S, et al. MMP9 induction by vascular endothelial growth factor receptor-1 is involved in lung-specific metastasis. *Cancer Cell.* Oct 2002;2(4):289-300.

3. Kaplan RN, Riba RD, Zacharoulis S, et al. VEGFR1-positive haematopoietic bone marrow progenitors initiate the pre-metastatic niche. *Nature.* Dec 8 2005;438(7069):820-827.

4. Kim S, Takahashi H, Lin WW, et al. Carcinoma-produced factors activate myeloid cells through TLR2 to stimulate metastasis. *Nature.* Jan 1 2009;457(7225):102-106.

5. Duda DG, Fukumura D, Munn LL, et al. Differential transplantability of tumor-associated stromal cells. *Cancer Res.* Sep 1 2004;64(17):5920-5924.

6. Fidler IJ. The relationship of embolic homogeneity, number, size and viability to the incidence of experimental metastasis. *Eur J Cancer.* Mar 1973;9(3):223-227.

7. Liotta LA, Saidel MG, Kleinerman J. The significance of hematogenous tumor cell clumps in the metastatic process. *Cancer Res.* Mar 1976;36(3):889-894.

8. Fidler IJ. The pathogenesis of cancer metastasis: the 'seed and soil' hypothesis revisited. *Nat Rev Cancer.* Jun 2003;3(6):453-458.

9. Ruiter DJ, van Krieken JH, van Muijen GN, de Waal RM. Tumour metastasis: is tissue an issue? *Lancet Oncol.* Feb 2001;2(2):109-112.

10. Sahai E. Illuminating the metastatic process. *Nat Rev Cancer.* Oct 2007;7(10):737-749.

11. Updyke TV, Nicolson GL. Malignant melanoma cell lines selected in vitro for increased homotypic adhesion properties have increased experimental metastatic potential. *Clin Exp Metastasis.* Oct-Dec 1986;4(4):273-284.

12. Kristjansen PEG, Roberge S, Lee I, Jain RK. Tissue-Isolated Human Tumor Xenografts in Athymic Nude-Mice. Nov 1994;48(3):389-402.

13. Swartz MA, Kristensen CA, Melder RJ, et al. Cells shed from tumours show reduced clonogenicity, resistance to apoptosis, and in vivo tumorigenicity. *British Journal of Cancer.* Nov 1999;81(5):756-759.

14. Wagers AJ, Sherwood RI, Christensen JL, Weissman IL. Little evidence for developmental plasticity of adult hematopoietic stem cells. *Science.* Sep 27 2002;297(5590):2256-2259.

15. Arbiser JL, Raab G, Rohan RM, et al. Isolation of mouse stromal cells associated with a human tumor using differential diphtheria toxin sensitivity. *Am J Pathol.* Sep 1999;155(3):723-729.

16. Padera TP, Stoll BR, Tooredman JB, Capen D, di Tomaso E, Jain RK. Pathology: cancer cells compress intratumour vessels. *Nature.* Feb 19 2004;427(6976):695.

17. Podsypanina K, Du YC, Jechlinger M, Beverly LJ, Hambardzumyan D, Varmus H. Seeding and propagation of untransformed mouse mammary cells in the lung. *Science.* Sep 26 2008;321(5897):1841-1844.

18. van Deventer HW, Wu QP, Bergstralh DT, et al. C-C chemokine receptor 5 on pulmonary fibrocytes facilitates migration and promotes metastasis via matrix metalloproteinase 9. *Am J Pathol.* Jul 2008;173(1):253-264.

19. Al-Mehdi AB, Tozawa K, Fisher AB, Shientag L, Lee A, Muschel RJ. Intravascular origin of metastasis from the proliferation of endothelium-attached tumor cells: a new model for metastasis. *Nat Med.* Jan 2000;6(1):100-102.

20. Duda DG, Cohen KS, Kozin SV, et al. Evidence for incorporation of bone marrow-derived endothelial cells into perfused blood vessels in tumors. *Blood.* Apr 1 2006;107(7):2774-2776.

21. Huang P, Duda DG, Jain RK, Fukumura D. Histopathologic findings and establishment of novel tumor lines from spontaneous tumors in FVB/N mice. *Comp Med.* Jun 2008;58(3):253-263.

22. O'Reilly MS, Holmgren L, Shing Y, et al. Angiostatin: a novel angiogenesis inhibitor that mediates the suppression of metastases by a Lewis lung carcinoma. *Cell.* Oct 21 1994;79(2):315-328.

23. Kristjansen PE, Roberge S, Lee I, Jain RK. Tissue-isolated human tumor xenografts in athymic nude mice. *Microvasc Res.* Nov 1994;48(3):389-402.

24. Swartz MA, Kristensen CA, Melder RJ, et al. Cells shed from tumours show reduced clonogenicity, resistance to apoptosis, and in vivo tumorigenicity. *Br J Cancer.* Nov 1999;81(5):756-759.

Supplementary figures and legends

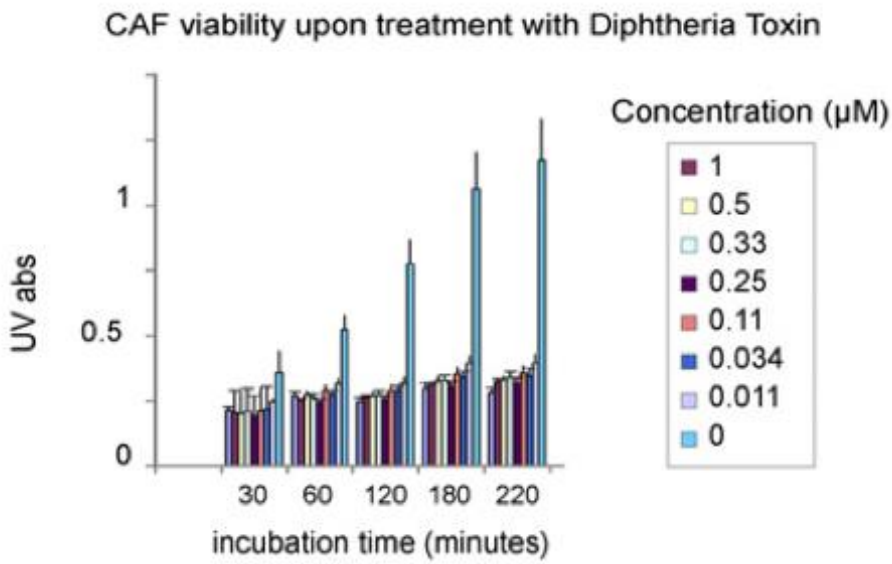

Fig S1| In vitro effect of Diphteria toxin on human CAFs. WST-1 cell survival/proliferation assay for DT treatment of human CAFs. The histogram plot shows that DT depletes human cells even at very low doses (0.011μM).

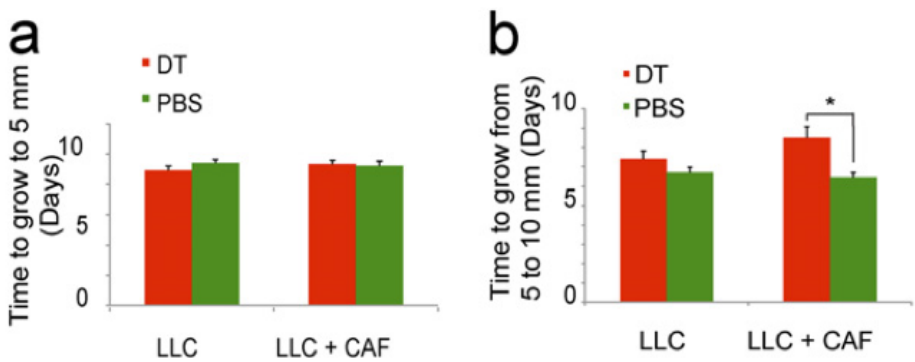

Figure S2| In vivo growth of LLC1 tumors after implantation of LLC1 cells alone or coimplantation of LLC1 cells with CAFs: effect of DT treatment. (A) Tumor growth after coimplantation of CAFs with LLC1 cells was not significantly different from after implantation of LLC1 alone. (B) Depletion of CAFs with DT treatment significantly delayed the established tumor growth only in the coimplanted group.

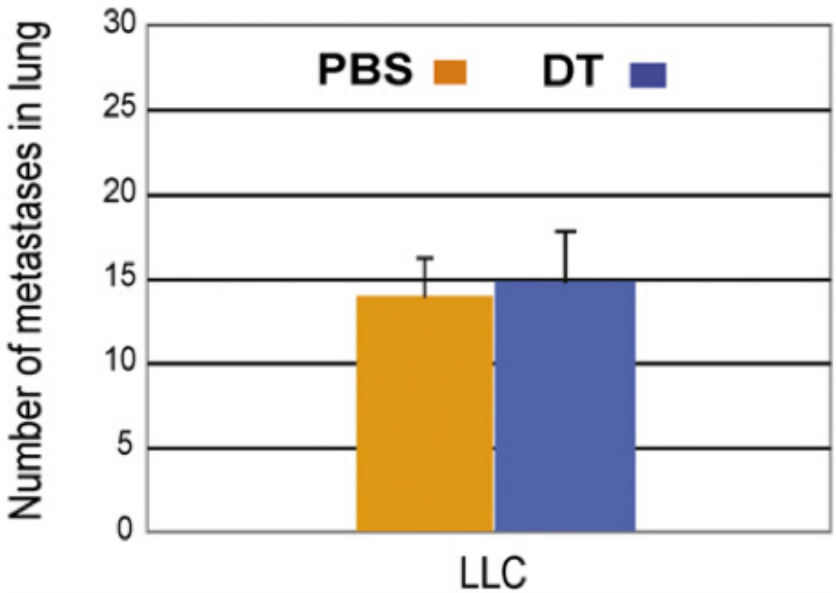

Fig S3| Effect of DT treatment on metastasis in LLC1 alone implantation model. DT treatment 1 day after primary LLC1 tumor resection does not affect metastasis.

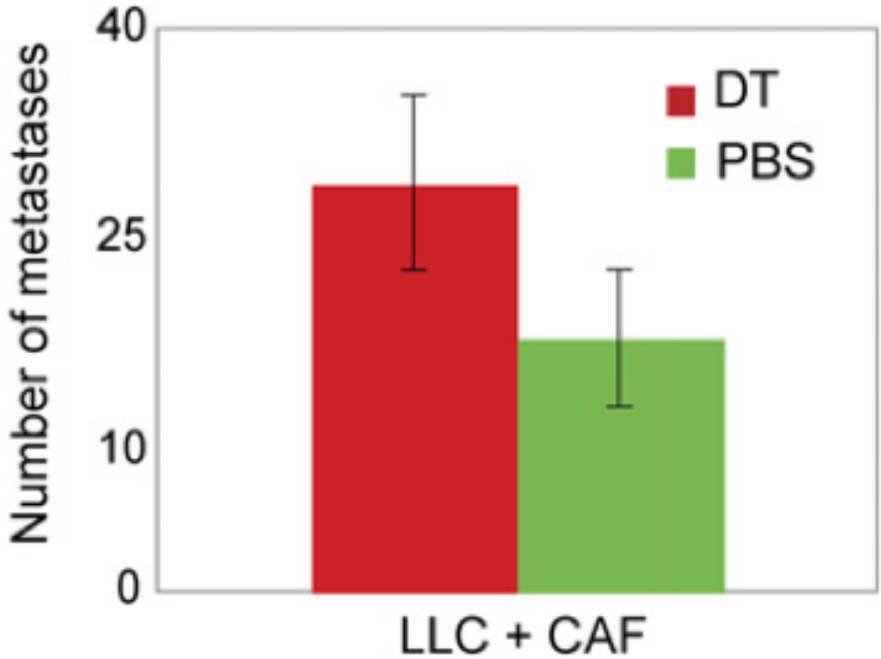

Fig S4|Metastasis formation after i.v. infusion of LLC1 cells with CAFs: effect of diphtheria toxin (DT) treatment. Depletion of CAFs with DT after i.v. infusion of LLC1 and CAFs does not affect metastasis formation.

Table S1. Size distribution of heterotypic cell fragments

Diameter (μm)	No. of clumps with GFP^+ cells per h per tumor (n = 5 mice), mean ± SEM (% of total)
<50	152 ± 52 (77)
50–99	23 ± 15 (12)
100–149	18 ± 9 (9)
150–200	5 ± 5 (3)
Total	198 ± 116

Table S2. Gene expression profile in CAFs using a 96-gene PCR array

Gene (symbol)	Ct value	Comments
Angiopoietin-like 4 (*ANGL4*)	22.19	Identified as a player in lung metastatic colonization
Alanyl aminopeptidase (*ANPEP*)	22.32	Proangiogenic factor
Monocyte-chemoattractant protein 1 (MCP-1) (*CCL2*)	24.24	Proangiogenic and prometastasis chemokine
Sphingosine-1-phosphate receptor 1 (*S1PR1*)	24.58	Receptor involved in angiogenesis, cell–cell adhesion and migration
Basic fibroblast growth factor (*FGF2*)	21.39	Proangiogenic growth factor
Hepatocyte growth factor (*HGF*)	24.39	Proangiogenic and migration factor
Hypoxia-inducible factor 1 alpha (*HIF1A*)	20.95	Proangiogenic signaling factor
Inhibitor of differentiation gene 3 (*ID3*)	21.21	Proangiogenic signaling factor
Interleukin 6 (*IL6*)	24.69	Proangiogenic inflammatory cytokine
Interleukin 8 (*IL8*)	23.3	Proangiogenic inflammatory cytokine
Integrin alpha v (*ITGAV*)	22.86	Receptor involved in angiogenesis, cell–cell adhesion and migration
Gellatinase A (*MMP2*)	20.82	Proangiogenic enzyme
Neuropilin 1 (*NRP1*)	21.45	Receptor involved in angiogenesis and migration
Sphingosine kinase 1 (*SPHK1*)	23.53	Lipid kinase that catalyzes formation of S1P and induces MMP1, Erk, and Ets1
Thrombospondin 1 (*THBS1*)	17.58	Endogenous antiangiogenic factor
Tissue inhibitor of metalloproteinase 1 (*TIMP1*)	17.22	Negative regulator of MMPs
Tissue inhibitor of metalloproteinase 2 (*TIMP2*)	20.33	Negative regulator of MMPs
Vascular endothelial growth factor A (*VEGFA*)	22.93	Proangiogenic growth factor
Vascular endothelial growth factor C (*VEGFC*)	22.95	Proangiogenic growth factor
B2M (control)	25.35	Housekeeping gene
HPRT1 (control)	26.08	Housekeeping gene
RPL13A (control)	21.87	Housekeeping gene
GAPDH (control)	18.99	Housekeeping gene
ACTB (control)	19.32	Housekeeping gene

Data are shown for the genes with a Ct value of <25 and for housekeeping genes.

Editors' choice

Science 24 December 2010

BIOMEDICINE

Travel Assistance

Tumor metastases are a major cause of death from solid tumors. Evidence from preclinical models suggests that tumor cells do not metastasize alone but rather are assisted by specific host cells that modify the microenvironment of the target organ so that it can support the survival and growth of newly arriving tumor cells. Two independent studies of lung metastasis in mice converge on this theme. Kowanetz *et al.* show that tumor cells secrete granulocyte colony-stimulating factor, a protein that expands and mobilizes bone marrow cells of a specific type called $Ly6G^+Ly6C^+$ granulocytes and facilitates their homing into the lung before the arrival of tumor cells. Upon accumulation in the lungs, these granulocytes then secrete proteins that enhance the invasive properties of tumor cells, including matrix metalloproteinases and Bv8, a protein that stimulates tumor cell migration. Duda *et al.* provide evidence that the stability of circulating metastatic tumor cells is enhanced when they "co-travel" with stromal cells derived from the primary tumor, such as fibroblasts. Once these cellular clumps reach the lung, the stromal cells appear to provide an early growth advantage to the tumor cells. Further exploration of the cells and signaling molecules identified in these studies could lead to therapies that prevent or inhibit metastases. — PAK

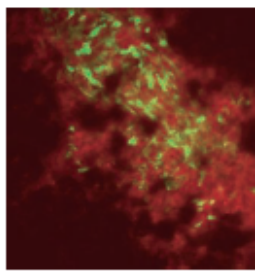

Stromal cells (green) accompany metastasizing tumor cells (red).

Proc. Natl. Acad. Sci. U.S.A. **107**, 21248; 21677 (2010).

PART II **TARGETING THE STROMA - ANTIANGIOGENIC TREATMENT**

Chapter 6

Combined targeting of HER2 and VEGFR2 for effective treatment of HER2-amplified breast cancer brain metastases

David P Kodack
Euiheon Chung
Hiroshi Yamashita
Joao Incio
Annique MMJ Duyverman
Youngchui Song
Christian T Farrar
Yuhui Huang
Eleanor Ager
Walid Kamoun
Shom Goel
Matija Snuderl
Alisha Lussiez
Lotte Hiddingh
Sidra Mahmood
Bakhos A Tannous
April F Eichler
Dai Fukumura
Jeffrey Engelman
Rakesh K Jain

Edwin L. Steele Laboratory for tumor Biology, Department of Radiation Oncology, Massachusetts General Hospital and Harvard Medical School, Boston, USA

Proc Natl Acad Sci U S A. 2012 Nov 6;109(45):E3119-27

Abstract

Brain metastases are a serious obstacle in the treatment of patients with human epidermal growth factor receptor-2 (HER2)–amplified breast cancer. Although extracranial disease is controlled with HER2 inhibitors in the majority of patients, brain metastases often develop. Because these brain metastases do not respond to therapy, they are frequently the reason for treatment failure. We developed a mouse model of HER2-amplified breast cancer brain metastasis using an orthotopic xenograft of BT474 cells. As seen in patients, the HER2 inhibitors trastuzumab and lapatinib controlled tumor pro- gression in the breast but failed to contain tumor growth in the brain. We observed that the combination of a HER2 inhibitor with an anti–VEGF receptor-2 (VEGFR2) antibody significantly slows tumor growth in the brain, resulting in a striking survival benefit. This benefit appears largely due to an enhanced antiangiogenic effect: Combination therapy reduced both the total and functional micro- vascular density in the brain xenografts. In addition, the combination therapy led to a marked increase in necrosis of the brain lesions. Moreover, we observed even better antitumor activity after combin- ing both trastuzumab and lapatinib with the anti-VEGFR2 antibody. This triple-drug combination prolonged the median overall survival fivefold compared with the control-treated group and twofold com- pared with either two-drug regimen. These findings support the clinical development of this three-drug regimen for the treatment of HER2-amplified breast cancer brain metastases.

Introduction

Approximately 25% of human breast cancers demonstrate amplification of the human epidermal growth factor receptor-2 (HER2) protooncogene. Patients with HER2-positive breast cancer are at a high risk of developing brain metastases, with a frequency as high as 50% in patients succumbing to advanced disease [1-4]. A combination of factors explains this phenomenon, including the proclivity of HER2-positive tumor cells to colonize the brain and improved control of extracranial disease with the anti-HER2 monoclonal antibody trastuzumab (Genentech/Roche) enabling patients to live long enough to develop brain metastases [3, 5]. Although systemic disease is under control in many of these patients, their associated brain metastases appear resistant to trastuzumab [2, 6, 7]. Furthermore, lapatinib (GlaxoSmithKline), a small-molecular-weight HER2 kinase inhibitor, thought to penetrate the blood–brain barrier better compared with trastuzumab, has shown only a modest response in patients with recurrent or progressive brain metastases [8-10]. Thus, alternative strategies are desperately needed to treat patients with metastatic disease [11].

Angiogenesis is critical to breast cancer progression and metastasis, and adversely affects prognosis [12, 13]. VEGF is one of the most potent angiogenic factors [14]. In patients with meta- static breast cancer, the anti-VEGF antibody bevacizumab (Genentech/Roche), in combination with paclitaxel, prolonged progression-free survival but not overall survival compared with paclitaxel alone [15]. In addition, the use of bevacizumab with trastuzumab and chemotherapy in HER2-positive metastatic breast cancer has shown some promise in phase II trials [16]. However, there remain no data on the efficacy of bevacizumab in the context of brain metastases because these patients have often been excluded from clinical trials due to fear of an increased risk of cerebral hemorrhage after anti-VEGF therapy. However, retrospective analysis has shown this potential risk may not be significant [17]. Currently, clinical trials are underway to evaluate the efficacy of bevacizumab in patients with HER2-positive disease (http://clinicaltrials.gov identifier NCT01004172). However, the effects of dual blockade of VEGF and HER2 in brain metastases have not been examined in preclinical models.

We have previously shown that trastuzumab alone can act as an antiangiogenic mixture in a leptomeningeal metastasis model of HER2-overexpressing breast cancer through a reduction in proangiogenic factors and an increase in an antiangiogenic factor [18]. These effects were transient, however, and were counter- acted by the compensatory production of VEGF from host stromal cells, perhaps to rescue angiogenesis. Indeed, carcinoma-associated fibroblasts as well as immune cells can produce significant amounts of VEGF in breast cancer models [19, 20] These overcome trastuzumab resistance by inhibiting the activity of the compensatory VEGF production by stromal cells, resulting in a significantly greater antiangiogenic effect. This hypothesis is consistent with the finding that targeting both HER2 and VEGF in orthotopic breast cancer xenografts results in better growth delay than targeting either agent alone [21, 22]. Furthermore, the phase II study of bevacizumab in combination with trastuzumab and capecitabine as first-line treatment for HER2-positive locally recurrent or metastatic breast cancer showed an overall response rate of 73% [16]. Herein, we developed a model of HER2-amplified breast cancer brain metastases. Although the brain metastases were resistant to single-agent lapatinib or trastuzumab, we observed that the combination of trastuzumab, lapatinib, and an anti- murine VEGFR2 antibody, DC101 [ImClone Systems/Eli Lilly and Company [23]], resulted in a markedly delayed progression of these brain metastases. These studies point to a new thera- peutic approach for patients with HER2-amplified breast cancer brain metastases.

Results

Mouse Model That Recapitulates the Differential Response of Intra- cranial and Extracranial HER2-Amplified Breast Cancers to HER2 Inhibitors. We used a previously established technique to monitor metastatic tumor growth sensitively and noninvasively in the brain in real-time [24]. HER2-amplified BT474 cells were infected with a lentivirus leading to expression of both Gaussia luciferase (Gluc) and cerulean fluorescent protein (CFP). This facilitates noninvasive monitoring of BT474-Gluc tumor growth in the brain parenchyma after direct injection (a) by measuring Gluc activity in the bloodstream (Gluc is secreted by tumor cells into the bloodstream) and (b) through the cranial window using intravital fluorescence microscopy, respectively. Fig. 1A illustrates a brain metastatic lesion as seen with bioluminescence imaging and intravital multiphoton microscopy. The BT474-Gluc brain lesion depicted by bioluminescence represents the ap-proximate tumor size on initiation of treatment (Fig. 1A, Left). Intravital multiphoton microscopy illustrates the brain lesion boundary (Fig. 1A, Center) and the abnormality of the tumor vasculature (Fig. 1A, Right). Blood Gluc activity correlated well with BT474-Gluc tumor volume as measured by intravital microscopy (Fig. S1A). Blood Gluc activity also correlated with tumor volume measured using MRI and bioluminescence (Fig. S1 B and C). Furthermore, analysis of tumor volume ex vivo using multispectral fluorescent imaging supports the correlation between blood Gluc activity and tumor volume (Fig. S1D). Thus, blood Gluc activity was used to monitor tumor size and response to treatment. We first tested the effects of anti-HER2 therapies on the growth of established BT474-Gluc tumors growing in the mammary fat pad (primary) and in the brain parenchyma (metastases). Treatment was initiated when brain metastatic tumors reached ~10 mm3 in volume [corresponding to a blood Gluc activity of 10 Relative Light Units per second (RLU/s)], as illustrated in Fig. 1A. Although BT474-Gluc tumors in the mammary fat pad responded well to trastuzumab or lapatinib treatment, both HER2 inhibitors failed to control BT474-Gluc tumor growth in the brain parenchyma (Fig. 1 B and C). Thus, this mouse model closely mirrors the discordant effects of therapy in patients with metastatic HER2-positive breast cancer.

Dual inhibition of HER2 and VEGFR2 significantly slows brain metastatic tumor growth and extends mouse survival

Based on our previous findings proposing VEGF as a mechanism of resistance to trastuzumab in HER2-amplified breast cancer brain metastases, we tested if the addition of an anti-VEGF pathway inhibitor to anti-HER2 therapy could control tumor growth better than anti-HER2 therapy alone (Fig. 2). Consistent with our findings above, either trastuzumab or lapatinib monotherapy slowed brain metastatic BT474-Gluc tumor growth by only a few days compared with control-treated tumors (Fig. 2 A and B, respectively). The minimal overall survival benefit of either monotherapy was consistent with its modest effect on tumor growth: trastuzumab prolonged average survival by 7 d (1.4-fold compared with control; Fig. 2A), and lapatinib prolonged average survival by 3 d (1.2-fold compared with control; Fig. 2B). At the time of euthanasia, the size of the brain metastatic tumor was consistent among mice and occupied nearly an entire hemisphere of the brain. Thus, mouse survival in our model was considered to reflect brain metastatic tumor burden. Treatment with the antimurine VEGFR2 antibody DC101 exhibited a significant delay in tumor growth, corresponding to an improvement in survival between 2.3- and 2.4-fold greater than control-treated mice (Fig. 2 A and B, respectively; $P < 0.001$). Intriguingly, the combination of trastuzumab (Fig. 2A) or lapatinib (Fig. 2B) with DC101 showed a substantial delay in BT474-Gluc brain metastatic growth. The combination of trastuzumab and DC101 prolonged mouse survival to a median of 47.5 d, almost threefold greater than control-treated mice (additional 31.5 d; $P < 0.01$ compared with DC101 monotherapy). The combination of lapatinib and DC101 prolonged mouse survival to a median of 47 d, 3.4-fold greater than control-treated mice (additional 33 d; $P < 0.001$ compared with DC101 monotherapy). The impressive tumor growth delay witnessed by the combination of trastuzumab and DC101 was confirmed using MRI (Fig. 3A), bioluminescent imaging (Fig. 3B), and postmortem ex vivo multispectral brain imaging (Fig. S2), further validating the reliability of blood Gluc activity in monitoring brain metastatic BT474-Gluc tumor growth.

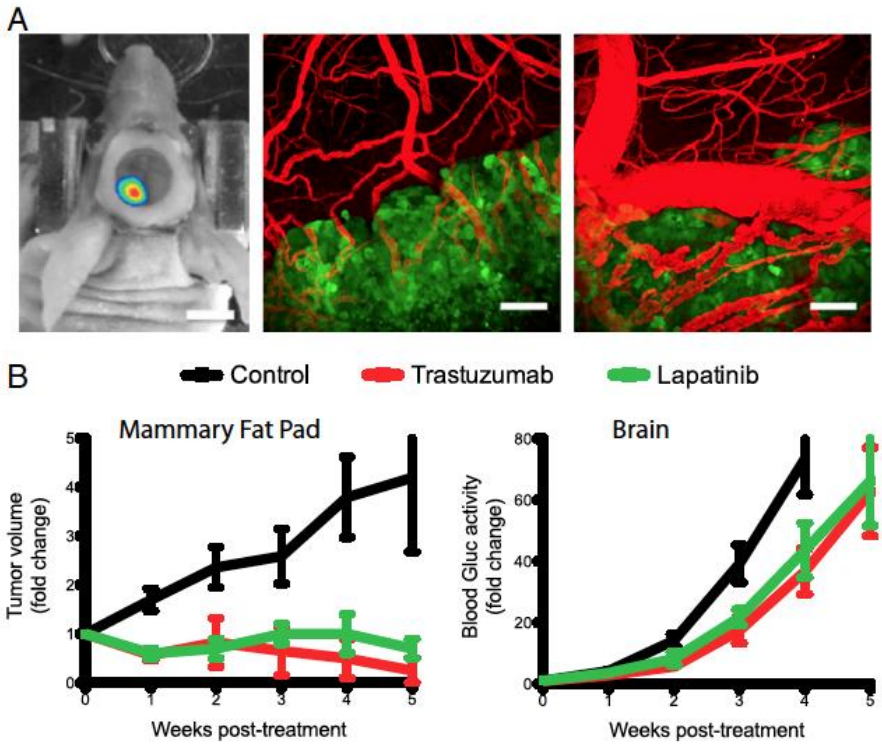

Fig. 1. Imaging of the breast cancer brain metastasis model and the effect of anti-HER2 therapies on tumor growth. (A) Imaging of an established BT474-Gluc tumor after direct injection into the brain parenchyma. The cranial window was used for intravital microscopy. (Left) Representative bioluminescence image of the tumor symbolizes its approximate size at treatment initiation. (Scale bar: 5 mm.) Intravital multiphoton microscopy images illustrate the brain metastatic lesion boundary (center) and the abnormality of the tumor vasculature (Right). (Scale bars: 100 μm.) Tumor cells expressing CFP are green, and blood vessels (red) are contrast-enhanced by i.v. injection of tetramethylrhodamine dextran (2,000,000 molecular weight). (B) Effect of trastuzumab (red, 5 mg/kg twice a week) or lapatinib (green, 100 mg/kg daily) on the growth of BT474-Gluc breast cancer cells when growing in the mammary fat pad (Left) or brain parenchyma (Right). Tumor growth curves for each treatment group are shown. Data are expressed as the mean ± SEM. (Left) BT474-Gluc mammary fat pad tumors were allowed to reach ~75 mm3 in volume before treatment initiation; the y axis is the fold-change of tumor volume (n = 6–8 mice). (Right) BT474-Gluc brain metastatic tumors were allowed to reach a blood Gluc activity of roughly 10 RLU/s, corresponding to a volume of ~10 mm3, before treatment initiation; the y axis is the fold-change of blood Gluc activity (n = 8–13 mice). (Treatment was initiated for BT474-Gluc brain metastatic tumors at ~10 mm3 in all subsequent experiments. Data are expressed as the mean ± SEM in all subsequent figures.)

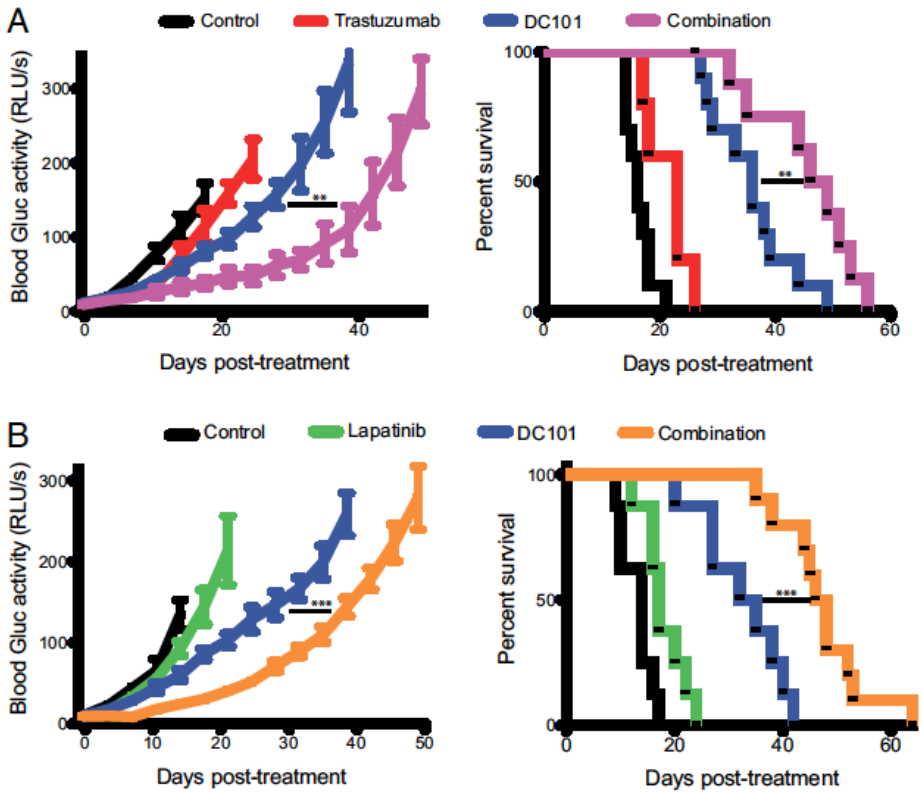

Fig. 2. Effects of anti-HER2 and anti-VEGFR2 therapies, and their combination on breast cancer growth in the brain parenchyma and mouse survival. Trastuzumab and lapatinib were dosed as previously mentioned, and DC101 was dosed at 40 mg/kg via i.p. injection twice a week. Tumor size was monitored twice a week via blood Gluc activity (Left), and animal survival was ascertained (Right). (A) Tumor growth plot (Left) and Kaplan–Meier survival plot (Right) of brain metastatic tumor-bearing mice treated with control (black), trastuzumab (red), DC101 (blue), or trastuzumab and DC101 (magenta) (n = 8–10 mice; except in the case of trastuzumab treatment, where n = 5 mice). **P < 0.01. (B) Tumor growth plot (Left) and Kaplan–Meier survival plot (Right) of brain metastatic tumor-bearing mice treated with control (black), lapatinib (green), DC101 (blue), or lapatinib and DC101 (orange) (n = 8–10 mice). ***P < 0.001. (Final tumor growth points occur when at least 3 mice are still alive.)

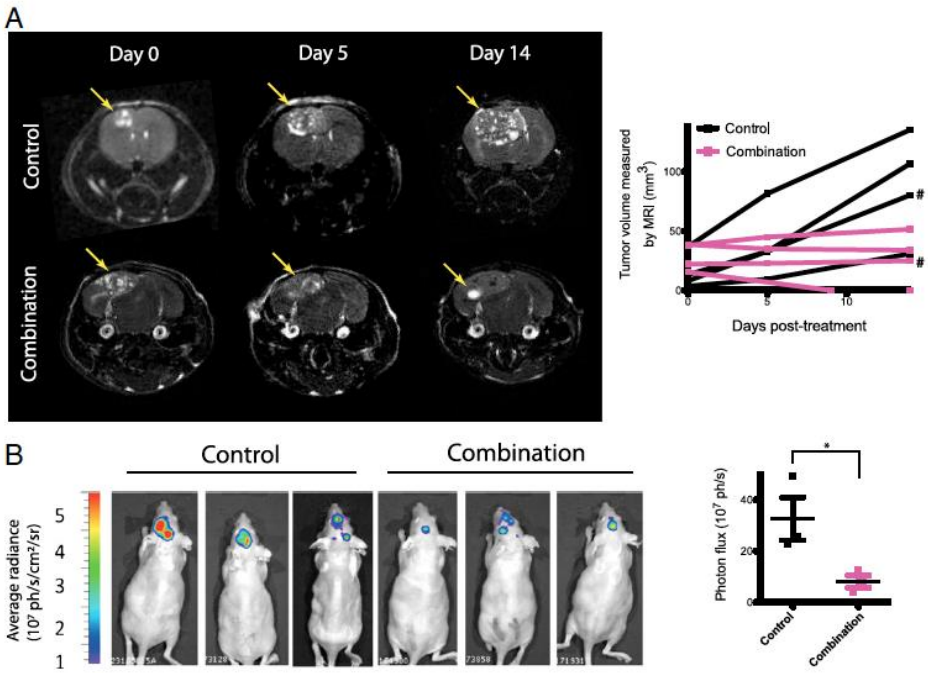

Fig. 3. Imaging of metastatic breast cancer growth in the brain parenchyma and response to the combination of anti-HER2 and anti-VEGFR2 therapy. (A) MRI analysis of control or trastuzumab and DC101 treatment on BT474-Gluc metastatic tumors in the brain. MRI tumor volume was measured on days 0, 5, and 14 of treatment. (Left) Representative MRI of control- and combination-treated tumors is shown. (Right) Tumor volume, calculated using MRI, is plotted for each individual mouse (# corresponds to the tumors illustrated by the MRI scans in A). (B) Bioluminescence imaging analysis of control or trastuzumab and DC101 treatment on metastatic BT474-Gluc tumors in the brain. (Left) Images of control- and combination-treated tumors 14 d after treatment initiation are shown. (Right) Average bioluminescence signal for the three control- and three combination-treated tumors is depicted. *P < 0.05.

Combination of anti-HER2 and anti-VEGFR2 therapies induces tumor necrosis through antivascular effects

To investigate the mechanism(s) for the effect of the combination treatment groups, we evaluated the histology of brain metastatic tumor tissues collected after 15 d of treatment with control IgG, trastuzumab, lapatinib, DC101, or the combination of each HER2 inhibitor with DC101. Immunohistochemical analysis revealed no obvious difference in tumor cell proliferation or apoptosis in viable tumor tissue from the six different

treatment groups (Fig. S3). In addition, analysis of tumor tissue collected after 4 or 8 d of treatment revealed no difference in tumor cell proliferation or apoptosis between groups. However, we found a clear difference in the necrotic fraction of tumor tissue between treatment groups after 15 d of treatment (Fig. 4 and Fig. S4). There was a significant increase in necrotic area in tumors treated with DC101 compared with control- or anti-HER2–treated tumors: 7–8% in control- or anti-HER2–treated tumors vs. 21 ± 1.5% in DC101-treated tumors ($P < 0.001$). This necrotic fraction was even higher within the combination-treated tumors: 28 ± 1.8% of the tumor area in the trastuzumab and DC101-treated mice and 27 ± 1.8% in the lapatinib and DC101-treated mice ($P < 0.01$ and $P < 0.05$, respectively, compared with DC101 monotherapy).

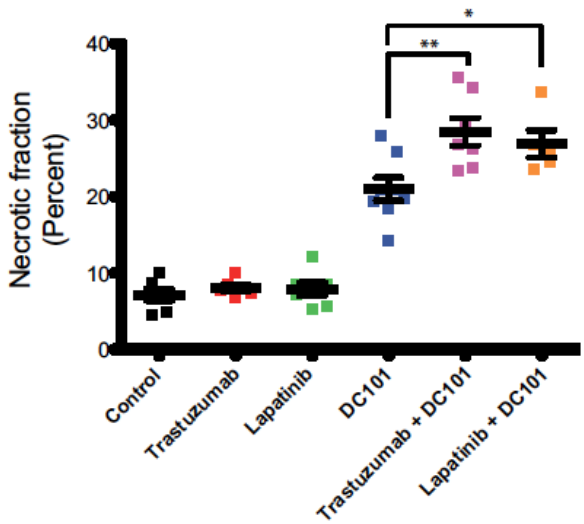

Fig. 4. Effects of the indicated treatments on the necrotic fraction of the tumor. The percentage of necrotic area in the total tumor area for each BT474-Gluc tumor was determined 15 d after treatment initiation using an in-house MATLAB program. **$P < 0.01$; *$P < 0.05$. DC101 vs. control, trastuzumab, or lapatinib ($P < 0.001$). Representative H&E-stained sections used for quantification of the necrotic area are shown in Fig. S4.

These findings indicate an enhanced antiangiogenic effect induced by the combination treatment groups, and thus led us to investigate their effects on the tumor vasculature. To this end, we stained brain metastatic lesions from all six treatment groups for both the endothelial cell marker CD31 and perfusion marker biotinylated-lectin, infused into the bloodstream 5 min before tumor tissue collection. HER2 inhibitors did not have a significant effect on the total or functional microvascular density (MVD) compared with control-treated tumors, which make up 5.09% and 3.88% of the viable tumor area, respectively (Fig. 5 and Fig. S5A). Mice treated with DC101 showed a decrease in the area of both total and functional viable tumor MVD to 2.75% and 1.84%, respectively, a decrease of ~50% compared with control-treated mice ($P < 0.001$). Finally, the combination treatments of trastuzumab and DC101 or lapatinib and DC101 revealed a steeper reduction in the total and functional tumor MVD compared with DC101 monotherapy. The combination of trastuzumab and DC101 decreased total and functional tumor MVD to 1.30% and 0.87% of viable tumor area, respectively, an approximate 75% reduction compared with control-treated tumor tissues ($P < 0.05$, compared with DC101 monotherapy). Meanwhile, the combination of lapatinib and DC101 decreased total and functional tumor MVD to 1.46% and 1.06%, respectively, an approximate 72% decrease compared with control-treated tumors ($P < 0.05$, compared with DC101 monotherapy). A similar trend was found in tumor tissues collected after 8 d of treatment (Fig. S5 B and C). These data demonstrate that combined anti-VEGFR2 and anti-HER2 therapies lead to a marked decrease in MVD and increased tumor necrosis.

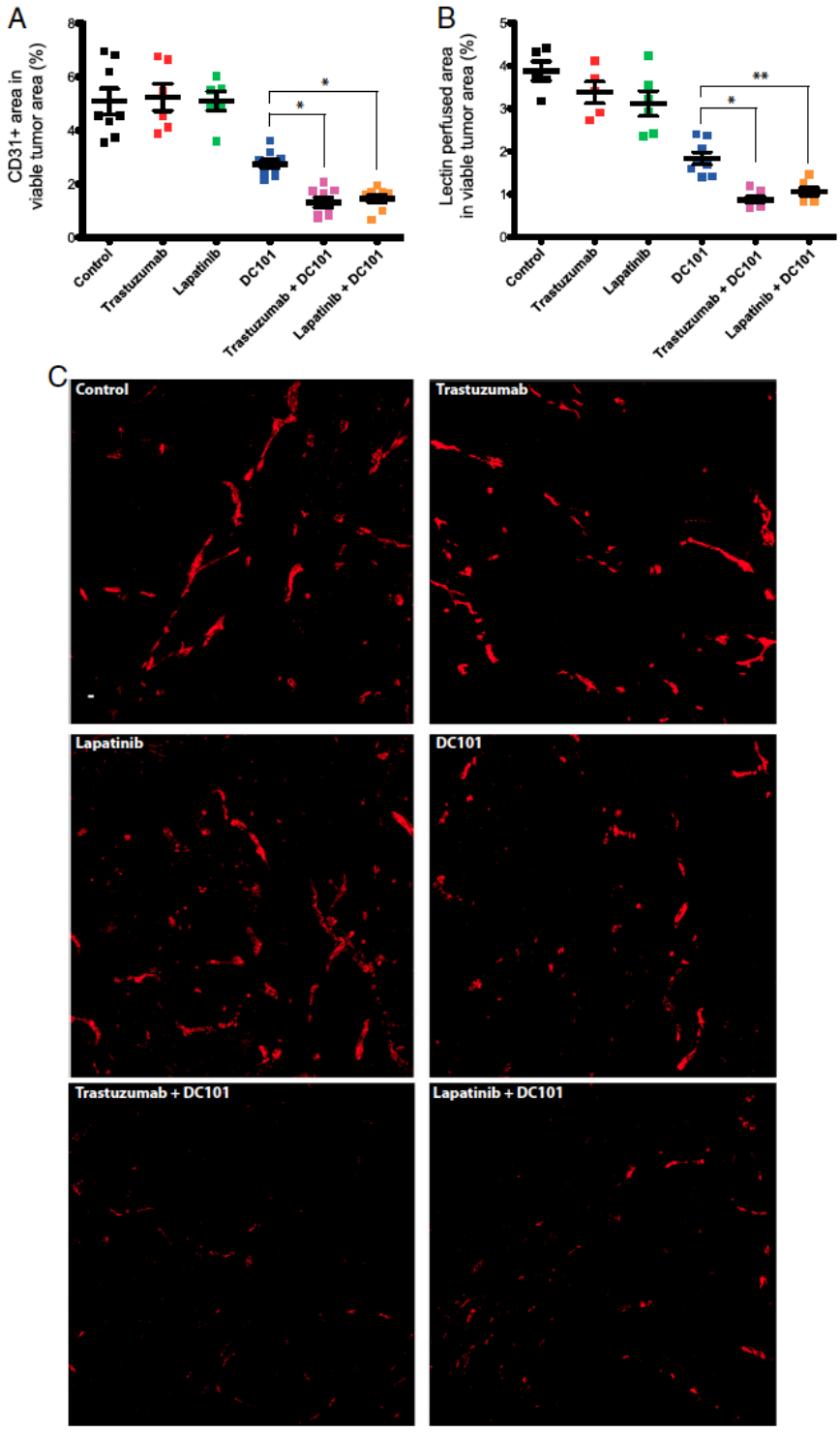
A
CD31+ area in viable tumor area (%)
0
2
4
6
8
*
*
Control
Trastuzumab
Lapatinib
DC101
Trastuzumab + DC101
Lapatinib + DC101
B
Lectin perfused area in viable tumor area (%)
0
1
2
3
4
5
*
**
Control
Trastuzumab
Lapatinib
DC101
Trastuzumab + DC101
Lapatinib + DC101
C
Control
Trastuzumab
Lapatinib
DC101
Trastuzumab + DC101
Lapatinib + DC101

Fig. 5. Effects of the indicated treatments on blood vessels. CD31-positive blood vessel area (A) and lectin-positive perfused blood vessel area (B) in the viable regions of BT474-Gluc tumors 15 d after treatment initiation. Tissues were analyzed by an in-house MATLAB program. *P < 0.05; **P < 0.01. DC101 vs. control, trastuzumab, or lapatinib (P < 0.001). (C) Representative images of CD31-positive endothelial cells in the viable tumor tissue. (Scale bar: 100 μm.) (Representative images of lectin-positive blood vessels in the viable tumor tissue are shown in Fig. S5A).

Delivery of HER2 inhibitors, NK cell infiltration, or direct tumor cell cytotoxicity does not mediate the reduction in metastatic tumor growth caused by the combination of HER2 and VEGFR2 inhibitors

We next investigated the possibility that the anti-VEGFR2 antibody augmented the capacity for the HER2 inhibitors to suppress signaling in the brain metastases. After 3 d of lapatinib, but not trastuzumab, treatment, we observed a significant decrease in phosphorylation of HER2 as well as downstream AKT and ERK in BT474-Gluc brain metastases (Fig. S6A). Consistent with this, after 3 d of lapatinib treatment, we found its concentration to be ~14.5 μM within the brain metastatic tumor (Fig. S6B). Although this concentration is one-third of that reached in tumors growing in the mammary fat pad, it is at least 500-fold greater than the in vitro IC50 for this cell line [25]. Interestingly, however, after 15 d of lapatinib treatment, this suppression of HER2 activation was no longer present (Fig. S7B). Western blot and immunohistochemical analysis showed that neither combination treatment group (neither trastuzumab and DC101 nor lapatinib and DC101) significantly altered the activation status of HER2 after 15 d of treatment, although a trend toward a modest decrease in HER2 activation was suggested (Fig. S7). In addition to direct signaling inhibition, another mechanism proposed for trastuzumab's efficacy is antibody-dependent cell cytotoxicity, mediated by natural killer (NK) cells [26]. Although the mechanism of trastuzumab in slowing BT474-Gluc mammary fat pad tumors was not mediated by NK cells (Fig. S8A), we found a significant increase in NK cells within the brain metastatic tumor after DC101 treatment alone or with trastuzumab (Fig. S8B). Therefore, we tested if NK cell depletion using the NK1.1 antibody (clone PK136; BioXCell) could alter tumor response to this combination therapy. Treatment with the NK1.1 antibody for 7 d resulted in a >99% and 95% reduction in NK cells in the

peripheral blood and spleen of nude mice, respectively (Fig. S8C). Untreated BT474-Gluc tumor growth in the brain parenchyma of nude mice was not altered due to the absence of NK cells, and the effect that the combination of trastuzumab and DC101 had on tumor growth and survival in nude mice lacking NK cells was no different from that in WT NK cell-competent nude mice (Fig. S8D). These findings are consistent with clinical data showing a lack of association between Fcγ receptor genotypes and trastuzumab efficacy [27]. Finally, DC101 had no direct effect, either alone or in combination with trastuzumab or lapatinib, on the growth of BT474-Gluc cells in vitro (Fig. S9). Taken together, these data indicate that the enhanced benefit of the anti-HER2 and anti-VGEFR2 combination therapy in this model is not primarily due to enhanced inhibition of HER2 activity, increased NK cell-mediated cytotoxicity, or direct cytotoxicity.

Dual HER2 targeting with trastuzumab and lapatinib delays brain metastatic tumor growth better than either monotherapy

Preclinical and clinical evidence suggests the combination of trastuzumab and lapatinib acts synergistically compared to either agent alone. One report attributes this to the marked downregulation of the protein survivin, leading to enhanced tumor cell apoptosis following the combination of the two agents [28]. Another report shows incomplete inhibition of the HER2 kinase after lapatinib monotherapy, and the addition of trastuzumab better suppresses HER3 phosphorylation by blocking ligand-independent interactions between HER2 and HER3 [29]. In agreement, we found better growth suppression of BT474-Gluc cells in vitro with the combination compared with either monotherapy (Fig. S10A). Furthermore, these preclinical results are supported by clinical data in both the preoperative primary and metastatic settings [30, 31]. Because these findings are limited to extracranial sites (primary and metastasis), we asked if the same tumor growth delay would occur in the brain metastasis setting. Of note, we consistently observed increased phosphorylation of HER2 in BT474-Gluc cells growing in the brain compared with the mammary fat pad (Fig. S10B). Although short-term (3 d) treatment with lapatinib significantly reduced HER2 phosphorylation in the brain, it could do so only to the level of that observed in the untreated mammary fat pad (Fig. S10B), and this effect disappeared after 15 d of treatment (Fig. S7B). We hypothesized that more

pronounced HER2 inhibition with the combination of trastuzumab and lapatinib would be beneficial to these brain metastases with increased HER2 activation. Consistent with the data from extracranial disease, we show a beneficial effect of combining trastuzumab and lapatinib compared with either monotherapy in our model of brain metastasis (Fig. 6A). Once again, we observed very little effect on tumor growth with either trastuzumab or lapatinib monotherapy, resulting in a 1.2-fold and 1.3-fold increase in median overall survival, respectively (a median of 31 d and 32 d, respectively, compared with 25 d in control-treated mice). However, the combination of two anti-HER2 agents shows a significant delay in tumor growth,
leading to an increase in median survival 1.8-fold greater than in control-treated mice (44 d compared with 25 d; $P < 0.001$ compared with either monotherapy).

Triple combination of trastuzumab, lapatinib, and DC101 produces a significant delay in tumor growth and improvement in mouse survival in our model of HER2-positive breast cancer brain metastasis

We next examined the efficacy of combining two anti-HER2 therapies with DC101. Remarkably, we found a more dramatic tumor growth delay in mice treated with the triple combination compared with the combination treatment of any two drugs (Fig. 6B). This delay in tumor growth was accompanied by a dramatic increase in survival. In this particular experiment, control mice lived for a median of 22.5 d. Mice treated with the combination of trastuzumab and lapatinib lived 2.2-fold longer than control mice (a median of 49 d). Mice treated with the combination of trastuzumab and DC101 or lapatinib and DC101 lived 2.6-fold or 2.3-fold longer, respectively, than control-treated mice (a median of 58 d or 52.5 d, respectively). Meanwhile, mice treated with the triple combination lived fivefold longer than control-treated mice (a median of 113 d; $P < 0.001$ compared with any double-treatment group). It is important to note that two of nine mice receiving triple combination therapy were euthanized after a significant loss in weight despite their brain metastatic tumors being relatively small. The reason for this is not clear, but toxicity associated with the three-drug regimen could be involved. Additionally, although the triple combination had a dramatic effect on overall survival and the growth of the brain metastases, all tumors eventually escaped from therapy.

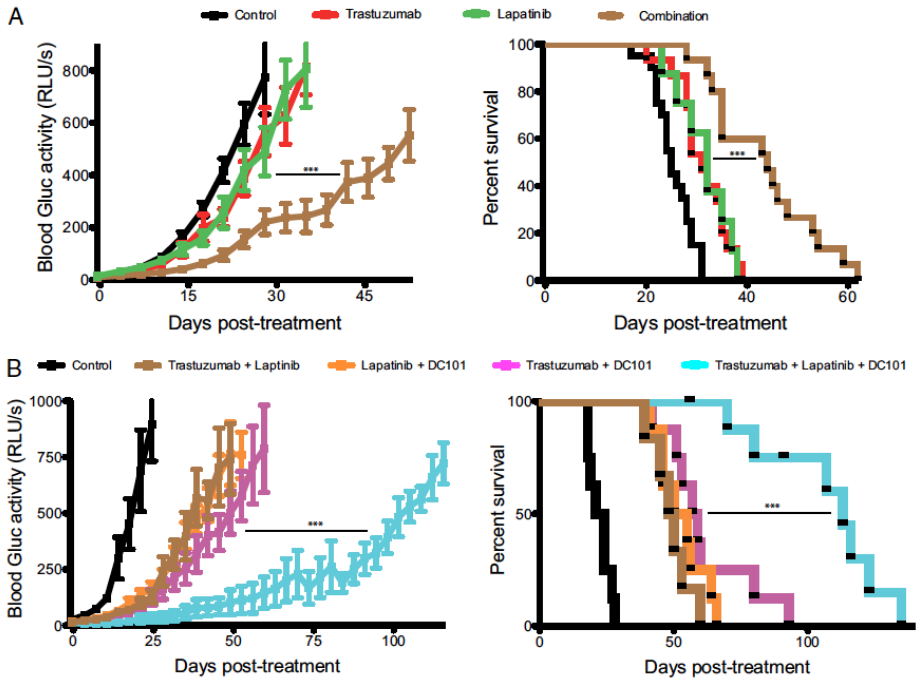

Fig. 6. Effects of dual HER2 targeting with and without anti-VEGFR2 therapy on BT474-Gluc brain metastatic tumors. (A) Tumor growth plot (Left) and Kaplan–Meier survival plot (Right) of tumor-bearing mice treated with control (black), trastuzumab (red), lapatinib (green), or trastuzumab and lapatinib (brown) (n = 8–20 mice). ***P < 0.001. (B) Tumor growth plot (Left) and Kaplan–Meier survival plot (Right) of tumor-bearing mice treated with control (black); trastuzumab and DC101 (magenta); lapatinib and DC101 (orange); trastuzumab and lapatinib (brown); and the triple combination of trastuzumab, lapatinib, and DC101 (cyan) (n = 6–9 mice). ***P < 0.001. (Final tumor growth points occur when at least three mice are still alive.)

Discussion

Studies of HER2-positive breast cancer metastasis to the brain have been severely hampered by the lack of clinically relevant laboratory models [11, 32-34]. We describe here a metastatic model that faithfully replicates the clinical response to treatment: failure of a HER2-dependent tumor growing in the brain to respond to anti-HER2 therapy. Although our direct brain parenchymal tumor implantation model lacks several earlier steps in the metastatic cascade [35], it allows for consistent tumor volume at treatment initiation as well as real-time evaluation of therapeutic efficacy using imaging and blood surrogate marker evaluation. The blood surrogate marker correlated not only with tumor volume, as estimated with intravital microscopy using the transparent cranial window model, but with tumor volume measurements made by MRI, bioluminescence, and ex vivo multispectral imaging. The reason for the differential tumor growth and response to anti-HER2 therapy when tumors are growing at these two different sites, as observed both in our laboratory model and in patients, has been elusive. Surprisingly, we witnessed increased phosphorylation of HER2 in tumor cells growing in the brain compared with the mammary fat pad. This increased HER2 activity could explain a mechanism of resistance, because the reduction in phosphorylation with lapatinib treatment reached a level only equal to that of untreated mammary fat pad tumors. In addition, the effect of lapatinib disappeared after 15 d of treatment. Increased HER2 activity in the brain metastatic tumors could also explain the reason why the combination of trastuzumab and lapatinib is more beneficial than monotherapy. Future studies will be needed to test whether more intense and/or prolonged HER2 inhibition is associated with better response. Our data provide a strong rationale for the development of anti-VEGF therapy for brain metastases from HER2-positive breast cancer. Murine VEGFR2 blockade significantly reduced tumor MVD and increased tumor necrosis and survival on its own. In combination with HER2 inhibition, VEGFR2 blockade showed an even more dramatic response. Moreover, the combination of VEGFR2 blockade with dual inhibition of HER2 showed the most impressive benefits, although there is the potential for increased toxicity. Although the exact mechanism for the triple combination is not entirely clear, we propose that the antiangiogenic benefit seen with an anti-HER2 agent and VEGFR2

blockade is synergizing with the direct tumor cell cytotoxicity induced by two anti-HER2 agents. A clinical trial studying the efficacy of carboplatin and bevacizumab in progressive breast cancer brain metastasis is currently underway (http://clinicaltrials.gov identifier NCT01004172). In this trial, patients with HER2-positive disease will also be treated with HER2 inhibitors, which may provide clinical evidence for the approach presented here. Some of these drug combinations have been previously tested in patients with HER2-amplified breast cancer, and there is a growing body of experience with the use of anti-VEGF therapies for primary brain tumors [12, 36]. Therefore, our findings could be readily translated into the clinic to increase survival in patients with brain metastatic HER2-amplified breast cancer whose systemic disease is responding to therapy. Moreover, future studies will be needed to determine how these brain metastases eventually escape from this triple combination therapy.

A recent study by our group confirmed better growth inhibition in primary breast tumors with the standard dose of DC101 (40mg/kg) compared with lower doses, owing to a superior antiangiogenic effect [37]. However, the study also reported an added benefit of immune therapy only when combined with a low dose of DC101 (10 mg/kg), but not with the standard dose, mediated through "normalization" of the tumor vasculature. Future studies must be done to determine the optimal dose of anti-VEGFR2 therapy when combined with anti-HER2 therapies in the brain metastatic setting to achieve the greatest tumor growth delay. Finally, it is important to mention that treatment of breast cancer brain metastases with anti-VEGF pathway therapy did not result in an increased invasive phenotype, similar to what is observed after anti-VEGF therapy in primary brain tumors, especially after tumor hypoxia [36]. Several theories could explain this phenomenon. Because BT474 cells are not invasive in nude mice, even when growing in the mammary fat pad, this phenomenon could be limited to this particular breast cancer cell line. To address this issue, future studies should investigate the invasiveness of a more aggressive breast cancer cell line when growing in the brain microenvironment after anti-VEGF therapy.

Another reason for the lack of invasiveness in response to anti-VEGF therapy in our model could be because breast cancer cells do not disseminate after colonizing the brain. Could it be that the brain is the last metastatic stop for breast cancer cells, even in a

hypoxic environment? If so, is this due to the unique brain microenvironment? Tracking the dissemination of breast cancer cells after growth in the brain would address this hypothesis.

Materials and methods

Cell Lines, Infections, and Culture

BT474 cells were transduced with an expression cassette encoding Gluc and CFP separated by an internal ribosomal entry site, using a lentiviral vector as previously described [24, 38]. CFP positive BT474 cells (BT474-Gluc) were sorted with a FACSAria cell sorter (BD Biosciences). BT474-Gluc cells were maintained in RPMI 1640 supplemented with 10% (vol/vol) FBS (Atlanta Biologics).

Mammary fat pad and brain metastatic xenografts

Female nude mice (8–9 wk of age) were ovariectomized and implanted with a 0.36-mg, 60-d release 17β-estradiol pellet (Innovative Research of America) the day before implantation of tumor cells and every 60 d thereafter. For the mammary fat pad model, 1 ± 106 BT474-Gluc cells were suspended in a 50-μL mixture of
PBS and Matrigel Matrix High Concentration (BD Biosciences) at a 1:1 ratio before injection. For injection into the brain, the head of the mouse was fixed with a stereotactic apparatus and the skull over the left hemisphere of the brain was exposed via skin incision. Using a high-speed air-turbine drill (CH4201S; Champion Dental Products) with a burr tip size of 0.5 mm in diameter, three sides of a square (~2.5 mm in length, each side) were drilled through the skull until a bone flap became loose. Using blunt tweezers, the bone flap was pulled back, exposing the brain parenchyma. Roughly 10 μL of a BT474-Gluc cell suspension, at a concentration of 2.5 Å~ 107 cells/mL in PBS, was injected into the brain parenchyma using an insulin syringe. The bone flap was then placed back into position in the skull and sealed using histocompatible cyanoacrylate glue, and the skin atop the skull was sutured closed. All animal procedures were performed according to the guidelines of the Public Health Service Policy on Human Care of Laboratory Animals and in accordance with a protocol approved by the Institutional Animal Care and Use Committee of Massachusetts General Hospital.

Tumor size monitoring and survival analysis

Tumor size was measured twice a week by measuring the activity of secreted Gluc in the blood. Measurement of blood Gluc was performed as described previously [24]. Briefly, blood was drawn from a slight nick in a tail vein of the mouse. Thirteen microliters of blood was collected and mixed with 3 μL of 50 mM EDTA, and was then stored at −20 °C. Blood was transferred to an opaque 96-well plate, and Gluc activity was measured using coelenterazine (CTZ; Nanolight) as a substrate and a plate luminometer (Centro XS LB960; Berthold Technologies). The luminometer was set to inject 100 μL of 50 μg/mL CTZ in PBS automatically, and photon counts were acquired for 1 s. All treatments were started when the blood Gluc activity reached ~10 RLU/s, which corresponds to a tumor volume around 10 mm3 (Fig. S1). For survival analysis, mice were euthanized when exhibiting signs of prolonged distress or neurological impairment or when they lost more than 20% of their body weight, defined as the survival end point.

Reagents and treatments

Trastuzumab (Genentech) and lapatinib (GlaxoSmithKline) were obtained from the Massachusetts General Hospital pharmacy. Trastuzumab was administered at a concentration of 5 mg/kg body weight twice a week by i.p. injection. Each lapatinib tablet was ground and dissolved in sterile water with 0.5% Tween 80 (Sigma–Aldrich) to a concentration of 10 mg/mL and administered at a concentration of 100 mg/kg of body weight once a day by oral gavage. DC101, a generous gift from Imclone Systems (Eli Lilly and Company) was administered at a concentration of 40 mg/kg of body weight twice a week by i.p. injection. The control treatment for lapatinib was 0.5% Tween 80 (10 μL/g), the control treatment for trastuzumab was 5 mg/kg of body weight of a nonspecific human IgG (Jackson ImmunoResearch Laboratories, Inc.), and the control treatment for DC101 was 40 mg/kg of body weight of a nonspecific rat IgG (Jackson ImmunoResearch Laboratories, Inc.).

Quantification of necrotic tumor area

Mouse brain with tumor tissue was cross-coronally sectioned through the center, fixed in 4% paraformaldehyde overnight, and embedded in paraffin. Ten-micometer sections were stained with H&E. Tumors were evaluated by a trained neuropathologist (M.S.), and areas of necrosis were designated. A custom-written MATLAB (MathWorks) program was used to determine the fraction of necrotic area in the tumor. The majority of tumors had a viable rim; thus, the total tumor area could be determined. The area of necrosis was then quantified with respect to the full cross-sectional tumor area.

Quantification of blood vessel and lectin perfusion area

Before euthanasia, mice were injected with 2.5 μg of biotinylated-lectin per gram of body weight into the heart and allowed to circulate for 5 min. For immunofluorescence staining, mouse brains were fixed for 8 h in 4% (vol/vol) formaldehyde in PBS at 4 °C, followed by incubation in 30% sucrose in PBS at 4 °C for 48 h and subsequent mounting in freezing media [Optimal Cutting Temperature (OCT); Tissue-Tek]. Brains were sectioned every 20 μm. For endothelial cell identification, tissue sections were incubated overnight at 4 °C with an anti-CD31 antibody (2.5 μg/mL, clone 2H8; Millipore), followed by incubation with a 1:200 dilution of an Alexa 649-conjugated anti-Armenian hamster antibody for 1 h at room temperature. For identification of perfused blood vessels, tissue sections were incubated for 1 h at room temperature with a 1:200 dilution of Alexa 546-conjugated streptavidin. Tissues were mounted with 4′-6-diamidino-2-phenylindole–containing mounting media (Vectashield; VectorLabs). Quantification of the stained area was performed using an in-house MATLAB program.

References

1. Brufsky AM, Mayer M, Rugo HS, et al. Central nervous system metastases in patients with HER2-positive metastatic breast cancer: incidence, treatment, and survival in patients from registHER. *Clin Cancer Res.* Jul 15 2011;17(14):4834-4843.

2. Leyland-Jones B. Human epidermal growth factor receptor 2-positive breast cancer and central nervous system metastases. *J Clin Oncol.* Nov 1 2009;27(31):5278-5286.

3. Lin NU, Winer EP. Brain metastases: the HER2 paradigm. *Clin Cancer Res.* Mar 15 2007;13(6):1648-1655.

4. Pestalozzi B. Trastuzumab does not increase the incidence of central nervous system (CNS) relapses in HER2-positive early breast cancer: the HERA trial experience. *Cancer Research.* 2011;71(24, Suppl 3):P4-17-01.

5. Palmieri D, Bronder JL, Herring JM, et al. Her-2 overexpression increases the metastatic outgrowth of breast cancer cells in the brain. *Cancer Res.* May 1 2007;67(9):4190-4198.

6. Sledge GW, Jr. HER2011: the changing face of HER2-positive breast cancer. *Clin Breast Cancer.* Mar 2011;11(1):9.

7. Stemmler HJ, Kahlert S, Siekiera W, Untch M, Heinrich B, Heinemann V. Characteristics of patients with brain metastases receiving trastuzumab for HER2 overexpressing metastatic breast cancer. *Breast.* Apr 2006;15(2):219-225.

8. Geyer CE, Forster J, Lindquist D, et al. Lapatinib plus capecitabine for HER2-positive advanced breast cancer. *N Engl J Med.* Dec 28 2006;355(26):2733-2743.

9. Lin NU, Carey LA, Liu MC, et al. Phase II trial of lapatinib for brain metastases in patients with human epidermal growth factor receptor 2-positive breast cancer. *J Clin Oncol.* Apr 20 2008;26(12):1993-1999.

10. Lin NU, Dieras V, Paul D, et al. Multicenter phase II study of lapatinib in patients with brain metastases from HER2-positive breast cancer. *Clin Cancer Res.* Feb 15 2009;15(4):1452-1459.

11. Eichler AF, Chung E, Kodack DP, Loeffler JS, Fukumura D, Jain RK. The biology of brain metastases-translation to new therapies. *Nat Rev Clin Oncol.* Jun 2011;8(6):344-356.

12. Folkman J. Angiogenesis: an organizing principle for drug discovery? *Nat Rev Drug Discov.* Apr 2007;6(4):273-286.

13. Kumar S, Ghellal A, Li C, et al. Breast carcinoma: vascular density determined using CD105 antibody correlates with tumor prognosis. *Cancer Res.* Feb 15 1999;59(4):856-861.

14. Dvorak HF. Vascular permeability factor/vascular endothelial growth factor: a critical cytokine in tumor angiogenesis and a potential target for diagnosis and therapy. *Journal of Clinical Oncology.* Nov 1 2002;20(21):4368-4380.

15. Miller K, Wang M, Gralow J, et al. Paclitaxel plus bevacizumab versus paclitaxel alone for metastatic breast cancer. *N Engl J Med.* Dec 27 2007;357(26):2666-2676.

16. Martin M, Makhson A, Gligorov J, et al. Phase II study of bevacizumab in combination with trastuzumab and capecitabine as first-line treatment for HER-2-positive locally recurrent or metastatic breast cancer. *Oncologist.* 2012;17(4):469-475.

17. Besse B, Lasserre SF, Compton P, Huang J, Augustus S, Rohr UP. Bevacizumab safety in patients with central nervous system metastases. *Clin Cancer Res.* Jan 1 2010;16(1):269-278.

18. Izumi Y, Xu L, di Tomaso E, Fukumura D, Jain RK. Tumour biology: herceptin acts as an anti-angiogenic cocktail. *Nature.* Mar 21 2002;416(6878):279-280.

19. Fukumura D, Xavier R, Sugiura T, et al. Tumor induction of VEGF promoter activity in stromal cells. *Cell.* Sep 18 1998;94(6):715-725.

20. Harmey JH, Dimitriadis E, Kay E, Redmond HP, Bouchier-Hayes D. Regulation of macrophage production of vascular endothelial growth factor (VEGF) by hypoxia and transforming growth factor beta-1. *Ann Surg Oncol.* Apr-May 1998;5(3):271-278.

21. du Manoir JM, Francia G, Man S, et al. Strategies for delaying or treating in vivo acquired resistance to trastuzumab in human breast cancer xenografts. *Clin Cancer Res.* Feb 1 2006;12(3 Pt 1):904-916.

22. Le XF, Mao W, Lu C, et al. Specific blockade of VEGF and HER2 pathways results in greater growth inhibition of breast cancer xenografts that overexpress HER2. *Cell Cycle.* Dec 2008;7(23):3747-3758.

23. Witte L, Hicklin DJ, Zhu Z, et al. Monoclonal antibodies targeting the VEGF receptor-2 (Flk1/KDR) as an anti-angiogenic therapeutic strategy. *Cancer Metastasis Rev.* Jun 1998;17(2):155-161.

24. Chung E, Yamashita H, Au P, Tannous BA, Fukumura D, Jain RK. Secreted gaussia luciferase as a biomarker for monitoring tumor progression and treatment response of systemic metastases. *PLoS One.* 2009;4(12):e8316.

25. Konecny GE, Pegram MD, Venkatesan N, et al. Activity of the dual kinase inhibitor lapatinib (GW572016) against HER-2-overexpressing and trastuzumab-treated breast cancer cells. *Cancer Res.* Feb 1 2006;66(3):1630-1639.

26. Spector NL, Blackwell KL. Understanding the mechanisms behind trastuzumab therapy for human epidermal growth factor receptor 2-positive breast cancer. *J Clin Oncol.* Dec 1 2009;27(34):5838-5847.

27. Hurvitz SA, Betting DJ, Stern HM, et al. Analysis of Fcgamma receptor IIIa and IIa polymorphisms: lack of correlation with outcome in trastuzumab-treated breast cancer patients. *Clin Cancer Res.* Jun 15 2012;18(12):3478-3486.

28. Xia W, Gerard CM, Liu L, Baudson NM, Ory TL, Spector NL. Combining lapatinib (GW572016), a small molecule inhibitor of ErbB1 and ErbB2 tyrosine kinases, with therapeutic anti-ErbB2 antibodies enhances apoptosis of ErbB2-overexpressing breast cancer cells. *Oncogene.* Sep 15 2005;24(41):6213-6221.

29. Garrett JT, Olivares MG, Rinehart C, et al. Transcriptional and posttranslational up-regulation of HER3 (ErbB3) compensates for inhibition of the HER2 tyrosine kinase. *Proc Natl Acad Sci U S A.* Mar 22 2011;108(12):5021-5026.

30. Blackwell KL, Burstein HJ, Storniolo AM, et al. Overall survival benefit with lapatinib in combination with trastuzumab for patients with human epidermal growth factor receptor 2-positive metastatic breast cancer: final results from the EGF104900 Study. *J Clin Oncol.* Jul 20 2012;30(21):2585-2592.

31. Guarneri V, Frassoldati A, Bottini A, et al. Preoperative chemotherapy plus trastuzumab, lapatinib, or both in human epidermal growth factor receptor 2-positive operable breast cancer: results of the randomized phase II CHER-LOB study. *J Clin Oncol.* Jun 1 2012;30(16):1989-1995.

32. Cruz-Munoz W, Kerbel RS. Preclinical approaches to study the biology and treatment of brain metastases. *Semin Cancer Biol.* Apr 2011;21(2):123-130.

33. Fidler IJ. The role of the organ microenvironment in brain metastasis. *Semin Cancer Biol.* Apr 2011;21(2):107-112.

34. Kienast Y, von Baumgarten L, Fuhrmann M, et al. Real-time imaging reveals the single steps of brain metastasis formation. *Nat Med.* Jan 2010;16(1):116-122.

35. Bos PD, Zhang XH, Nadal C, et al. Genes that mediate breast cancer metastasis to the brain. *Nature.* Jun 18 2009;459(7249):1005-1009.

36. Carmeliet P, Jain RK. Molecular mechanisms and clinical applications of angiogenesis. *Nature.* May 19 2011;473(7347):298-307.

37. Huang Y, Yuan J, Righi E, et al. Vascular normalizing doses of antiangiogenic treatment reprogram the immunosuppressive tumor microenvironment and enhance immunotherapy. *Proc Natl Acad Sci U S A.* Oct 23 2012;109(43):17561-17566.

38. Wurdinger T, Badr C, Pike L, et al. A secreted luciferase for ex vivo monitoring of in vivo processes. *Nat Methods.* Feb 2008;5(2):171-173.

Supplemental information

Cranial window, intravital multiphoton microscopy, and tumor volume calculation

Cranial windows were implanted into nude mice as previously described [1]. Intravital imaging of normal and angiogenic vessel morphology was performed using custom-built multiphoton laser scanning microscopy instrumentation. To contrast-enhance functional blood vessels, angiography was performed after i.v. injection of 0.1 mL rhodamine-dextran (10 mg/mL, 2,000 kDa). For intravital tumor volume calculation, BT474-Gaussia luciferase (Gluc) tumors were measured twice a week by intravital fluorescent microscopy. Using an in-house MATLAB (MathWorks) program, an ellipse was fitted to the cerulean fluorescent protein (tumor) signal and the short and long axes were calculated. Tumor volume was calculated based on a half ellipse, using the following equation:

$$\text{Tumor volume} = ((\text{long axis}) \times (\text{short axis}) \times ((\text{long axis} + \text{short axis})/2) \times \pi/6)/2$$

MRI

MRI-based measurement of tumor growth was performed similar to the technique used by Kamoun et al. [2]. All experiments were performed on a 9.4-T magnet (Magnex Scientific Ltd.) equipped with a gradient coil with a 60-mm inner diameter (Resonance Research) and interfaced with an MRI console (Bruker BioSpin). The gradient coil has a maximum strength of 1,500 mT/m and a rise time of 100 μs. Images were acquired using a home-built mouse head birdcage coil. Mice were positioned on a custom-made mouse cradle and anesthetized with 1.5% (vol/vol) isoflurane in a 50:50 O2/medical air mixture with total flow rate of 1,200 mL/min. T2-weighted RARE images were acquired to assess the tumor volume. The image acquisition parameters were as follows: echo time/repetition time = 10/3,000 ms; rapid acquisition relaxation enhanced factor = 16, four averages; field of view = 1.92 cm; matrix = 128 x 128 (in-plane resolution = 150 μm); 0.5-mm slice thickness; and 11 image slices. Tumor volume was determined manually from the T2 hyperintense tumor regions of the brain.

Bioluminescence imaging

Individual animals were anesthetized, and bioluminescence imaging (BLI) was performed immediately after retroorbital injection of coelenterazine (CTZ) solution (at a concentration of 4 mg/kg of body weight). An In Vivo Imaging System (IVIS Lumina II; Caliper Life Sciences) was used for bioluminescence image recording. The image acquisition time was 30 s at a precise 30-s time point after retroorbital injection. (Because Gluc has flash kinetics, imaging at a consistent time after CTZ injection is critical.) Postprocessing and quantification were performed using Living Image Software 3.0 (Caliper Life Sciences) coupled to the IVIS system. Image analysis was done similar to the technique used by Chung et al. [3].

Ex vivo multispectral fluorescent imaging

The same mice used for the MRI analysis, bearing BT474-Gluc tumors treated with either control IgGs or the combination of trastuzumab and DC101, were killed immediately after the last imaging sequence. The entire brain was collected and fixed in 4% formaldehyde. After 24 h, the brain was sectioned into 1-mm slices. The tumor area was revealed in each section by spectral unmixing using the Maestro System (Cambridge Research and Instrumentation). Tumor volume was calculated by integration of the tumor areas, knowing that each section is 1 mm thick.

Histology and immunostaining

Before embedding tissues in paraffin, mouse brains were fixed for 8 h in 4% formaldehyde in PBS at 4 °C, followed by washes in PBS and storage at 4 °C. Phosphorylation of human epidermal growth factor receptor-2 (HER2) was visualized with an anti–phospho-HER2 antibody (Tyr1221/Tyr1222, clone 6B12; Cell Signaling Technology) diluted at 1:320 in SignalStain Diluent (Cell Signaling Technology) and incubated overnight, followed by incubation with SignalStain Boost IHC Detection Reagent (HRP, rabbit; Cell Signaling Technology) for 1 h at room temperature (RT). Identification of proliferating cells was done using a Ki67 antibody (clone MIB-1; Dako)

supplied at the working concentration and incubated for 1 h at RT, followed by incubation with mouse EnVision polymer (Dako) for 30 min at RT. Identification of apoptotic cells was accomplished using an antibody to cleaved caspase 3 (clone 5A1E; Cell Signaling Technology) diluted 1:50 and incubated overnight. Liquid DAB+
(Dako) was used to detect HRP-conjugated anti-mouse and antirabbit secondary antibodies, followed by mounting in Permount.

Western blotting

Tumor tissues were resuspended in 1% Nonidet P-40 lysis buffer (15 mM Tris, 10 mM EDTA, 10 mM EGTA) with protease and phosphatase inhibitors, and incubated on ice for 10 min. After cell lysis, lysates were centrifuged at 14,000 rpm (~18,000 x g) for 10 min at 4 °C. The protein concentration of the supernatant was measured before boiling in Laemmli buffer. Western blot analysis was conducted after separation by SDS/PAGE electrophoresis and transferred to nitrocellulose membranes. Immunoblotting was performed according to the antibody manufacturers' recommendations. The anti–phospho-HER2, anti-posphoAkt, anti-Akt, anti-phospho-ERK, and anti-ERK antibodies wereobtained from Cell Signaling Technologies, and the anti-HER2 antibody was obtained from Calbiochem (EMD Chemicals).

Fluorescence-activated cell sorting and quantification of tumor natural killer cells, and depletion of natural killer cells

For the quantification of natural killer (NK) cells within the tumor, tumor- bearing mice were intracardially perfused with PBS. Tumor tissues were harvested, minced, and digested at 37 °C for 60 min with complete DMEM containing collagenase type 1A (1,500 U/mL), hyaluronidase (1,000 UI/mL), and DNase (2 mg/mL). The digestion mixtures were filtered through 70-μm cell strainers. Single-cell suspensions were incubated with rat anti-mouse CD16/CD32 monoclonal antibodies and then stained, washed, and resuspended in cold buffer (1% BSA, 0.1% NaN3 in PBS). 7-Aminoactinomycin D (eBioscience) was added to the stained tubes (5 μL per tube) to exclude dead cells. Flow cytometry data were acquired on an LSRII flow cytometer (Becton Dickinson Biosciences)

and analyzed with FACSDiva software (Becton Dickinson Biosciences). Appropriate fluorochrome-conjugated, isotype-matched control IgGs were used in all experiments. The anti-mouse antibodies CD45-phycoerythrin (PE)-Cy7 and NK1.1-PE (Becton Dickson Biosciences) were used. For the depletion of NK cells in mice, the NK1.1 antibody (clone PK136; BioXCell) was administered at a concentration of 4 mg/kg of NK1.1 antibody was 4 mg/kg of body weight of a nonspecific mouse IgG (Jackson ImmunoResearch Laboratories, Inc.).

In vitro cell growth assay

A total of 3,000 BT474-Gluc cells were seeded in RPMI +5% FBS in a 96-well plate and allowed to adhere overnight. Cells were treated the following day, and growth was measured 5 d after treatment addition. Cell growth was measured using the CellTiter-Glo Luminescent Cell ViabilityAssay (Promega).

Statistical analysis

Data are expressed as the mean ± SEM unless otherwise noted. The principal statistical test was a one-way ANOVA, and Tukey's posttest was used to compare all pairs of columns. A t test (two-tailed with unequal variance) was used when only two variables were present in the analysis. Significant differences in tumor growth were accomplished by determining the time it took (in days) to reach a specific blood Gluc activity (specific for each experiment and illustrated on the tumor growth curve graph) (Fig. 2 A and B, Fig. 6 A and B, and Fig. S8D). The survival curves were estimated using the Kaplan–Meier method, and the median survival day was used when determining statistical difference. Statistical significance is defined throughout the main text and figure legends. GraphPad Prism was used for all statistical analysis.

References

1. Yuan F, Salehi HA, Boucher Y, Vasthare US, Tuma RF, Jain RK. Vascular permeability and microcirculation of gliomas and mammary carcinomas transplanted in rat and mouse cranial windows. *Cancer Res.* Sep 1 1994;54(17):4564-4568.

2. Kamoun WS, Ley CD, Farrar CT, et al. Edema control by cediranib, a vascular endothelial growth factor receptor-targeted kinase inhibitor, prolongs survival despite persistent brain tumor growth in mice. *J Clin Oncol.* May 20 2009;27(15):2542-2552.

3. Chung E, Yamashita H, Au P, Tannous BA, Fukumura D, Jain RK. Secreted gaussia luciferase as a biomarker for monitoring tumor progression and treatment response of systemic metastases. *PLoS One.* 2009;4(12):e8316.

Supplemental figures

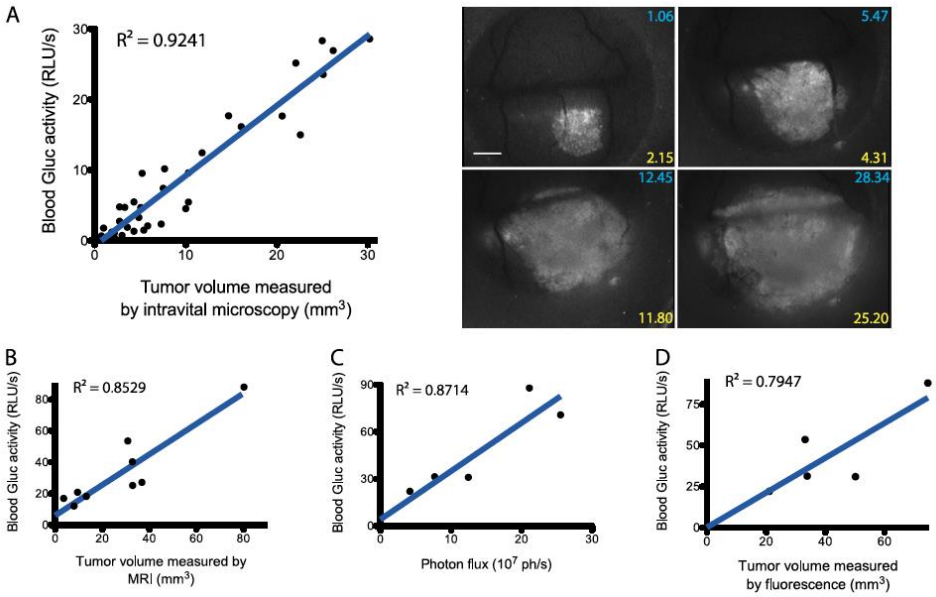

Fig. S1| Correlation of blood Gluc activity and tumor volume measurements. (A) Correlation of blood Gluc activity and tumor volume, measured using intravital microscopy. BT474-Gluc cells were injected into the brain parenchyma of mice with a cranial window. Tumors were imaged through the cranial window using a fluorescent microscope, and tumor length and width were obtained, from which volume was calculated. Blood was collected from the mice at the time of imaging. (Left) Blood Gluc activity is plotted against tumor volume, and linear regression analysis was performed using Prism software. Representative pictures are shown (Right), and inserted numbers correspond to the blood Gluc activity (Upper, blue) and the calculated tumor volume (Lower, yellow) (n = 8 mice, 44 separate measurements). (Scale bar: 1 mm.) (B) Correlation of blood Gluc activity and tumor volume, measured with MRI; representative images are shown in Fig. 3A (control-treated mice only; n = 4 mice, 9 separate measurements). (C) Correlation of blood Gluc activity and tumor volume, measured with bioluminescence imaging; representative images are shown in Fig. 3B (control-treated mice only; n = 5 mice). (D) Correlation of blood Gluc activity and tumor volume, measured by ex vivo multispectral fluorescent microscopy; representative images are shown in Fig. S2 (control-treated mice only; n = 5 mice).

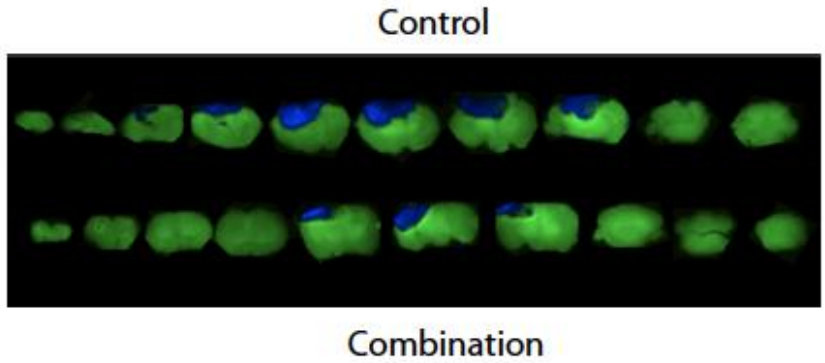

Fig. S2| Representative images of control-treated (Upper) or trastuzumab and DC101-treated (Lower) brain sections. Spectral unmixing reveals tumor (cerulean fluorescent protein, blue) and normal (autofluorescence, green) tissue. Each section is 1 mm thick. Images were obtained with the Maestro System.

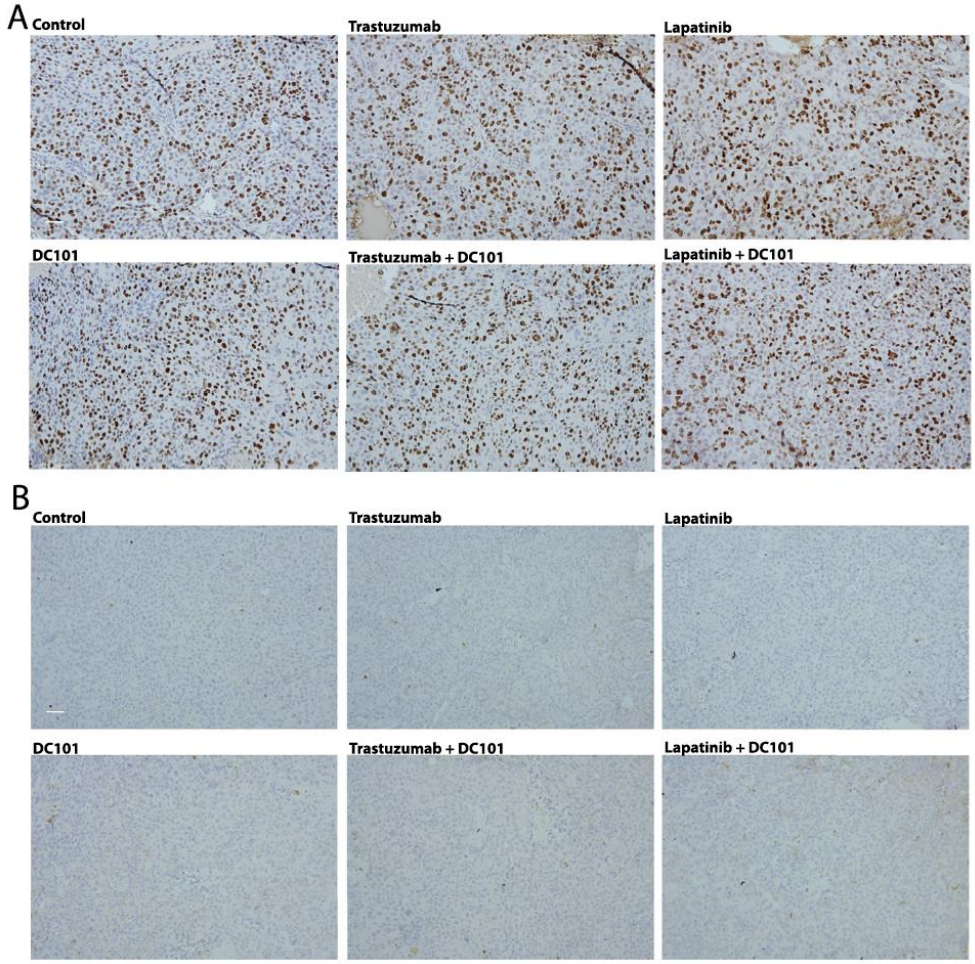

Fig. S3| Effect of the indicated treatments on cell proliferation and apoptosis. Immunohistochemical analysis of Ki67 (**A**) or cleaved caspase 3 (**B**) staining in tumor tissues harvested 15 d after the initiation of treatment and paraffin-embedded. (Scale bars: 50 μm.)

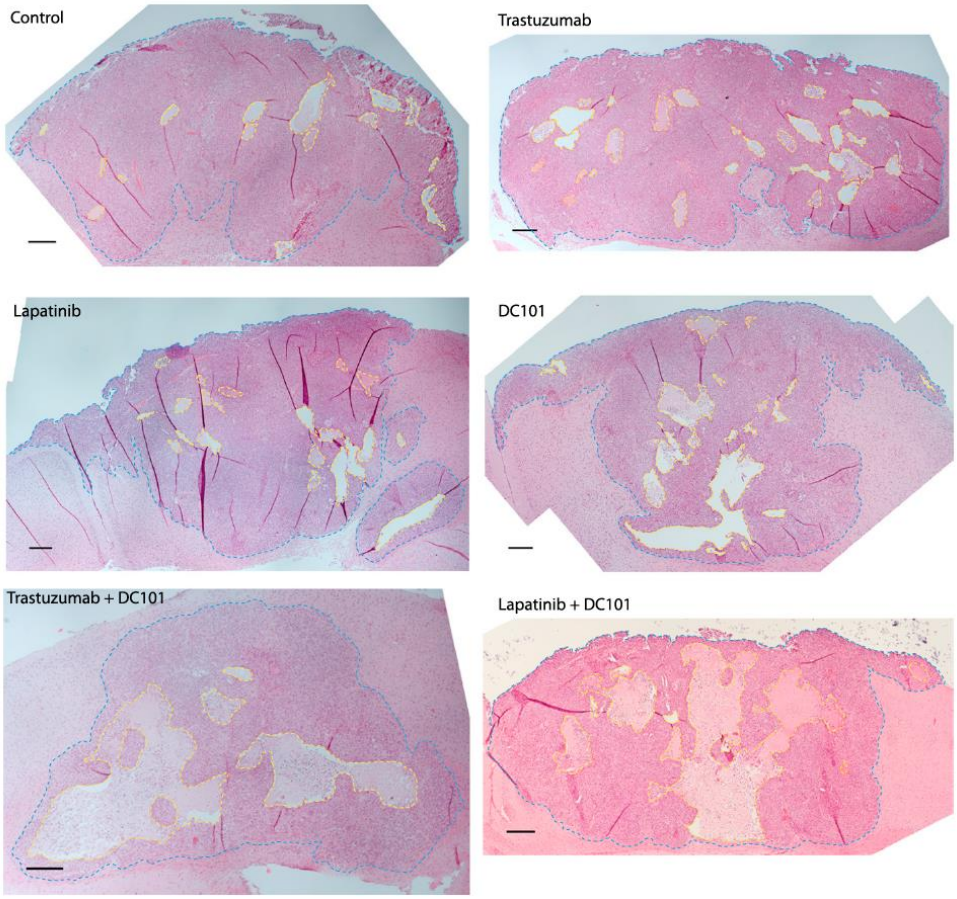

Fig. S4| Representative H&E-stained sections of BT474-Gluc brain metastatic tumor tissues used for the quantification of the necrotic area in Fig. 4. The borders of total tumor area and necrotic regions are highlighted in dotted blue and yellow lines, respectively. (Scale bars: 250 μm.)

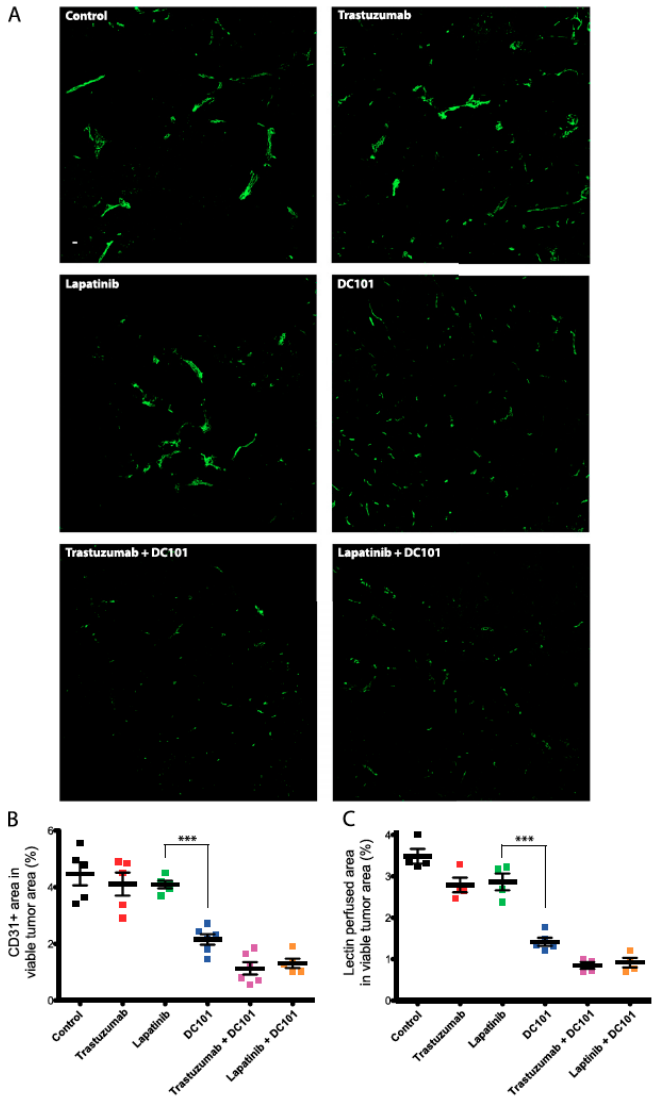

Fig. S5| Effect of the indicated treatments on the tumor vasculature. (**A**) Representative images of lectin-positive endothelial cells in the viable tumor tissue 15 d after the start of treatment. (Scale bar: 100 **μ**m.) (**B** and **C**) Effects of the indicated treatments on blood vessels in BT474-Gluc tumors 8 d after treatment initiation. (**B**) Percentage of CD31-positive blood vessel area within the viable tumor regions for each tumor was calculated using an in-house MATLAB program. (**C**) Before euthanasia, mice were injected with 2.5 μg of biotinylated-lectin per gram of body weight into the heart and allowed to circulate for 5 min. The area of lectin-positive blood vessels in the viable tumor regions for each tumor was calculated using an in-house MATLAB program. ***P < 0.001. DC101 vs. trastuzumab and DC101 or lapatinib and DC101, not statistically different.

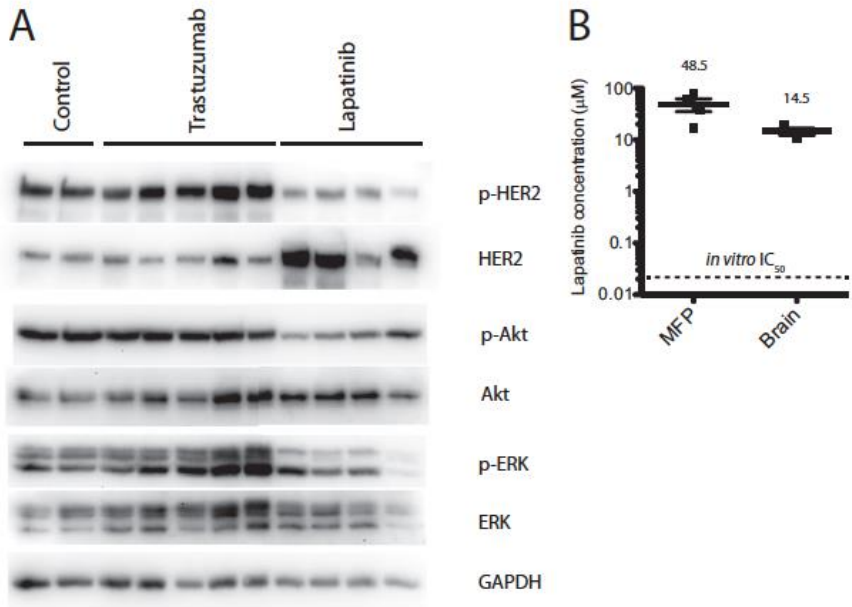

Fig. S6| Effect and delivery of the indicated treatments. (A) Effect of trastuzumab and lapatinib treatment on HER2, AKT, and ERK phosphorylation in BT474- Gluc tumors growing in the brain 3 d after treatment initiation. Tumor tissues were collected 2 h after the last treatment. Western blotting illustrates levels of HER2, AKT, and ERK phosphorylation and corresponding total protein levels, as well as for GAPDH as a loading control. (B) Concentration of lapatinib in BT474-Gluc mammary fat pad and brain metastatic tumors (not statistically different). The dotted line marks the reported in vitro IC50 of lapatinib for BT474 cells.

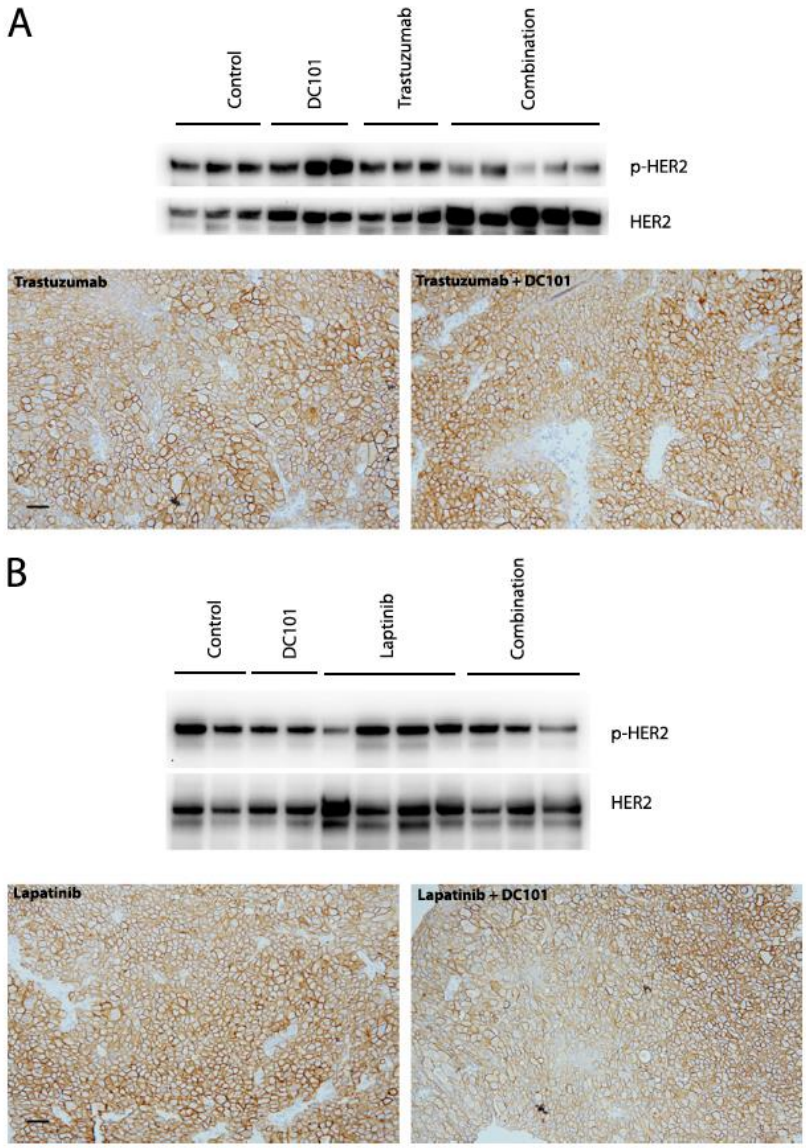

Fig. S7| Effect of anti-HER2 treatments alone or in combination with anti-VEGFR2 treatment on HER2 phosphorylation (p-HER2). Brain metastatic BT474-Gluc tumor tissues were harvested 15 d after the initiation of treatment with trastuzumab monotherapy and in combination with DC101 (A) or lapatinib monotherapy and in combination with DC101 (B). Tissues were either snap-frozen for protein lysis and Western blotting (Upper) or paraffin-embedded for immunohistochemistry (Lower). (Scale bars, 50 μm.)

Chapter 7

Edema control by cediranib, a vascular endothelial growth factor receptor–targeted kinase inhibitor, prolongs survival despite persistent brain tumor growth in mice

Walid S. Kamoun
Carsten D. Ley
Christian T. Farrar
Annique M M J Duyverman
Johanna Lahdenranta
Delphine A. Lacorre
Tracy Batchelor
Emmanuelle di Tomaso
Dan G Duda
Lance L. Munn
Dai Fukumura
A. Gregory Sorensen
Rakesh K. Jain

Edwin L. Steele Laboratory for tumor Biology, Department of Radiation Oncology, Stephen E. and Catherine Pappas Center for Neuro-Oncology, and A.A. Martinos Center for Biomedical Imaging, Massachusetts General Hospital; and Division of Health Sciences and Technology, Harvard Medical School, Boston, MA.

J Clin Oncol. 2009 May 20;27(15):2542-52

Abstract

Recent clinical trials of antivascular endothelial growth factor (VEGF) agents for glioblastoma showed promising progression-free and overall survival rates. However, available clinical imaging does not separate antitumor effects from antipermeability effects of these agents. Thus although anti-VEGF agents may decrease tumor contrast-enhancement, vascularity, and edema, the mechanisms leading to improved survival in patients remain incompletely understood. Our goal was to determine whether alleviation of edema by anti-VEGF agents alone could increase survival in mice. We treated mice bearing three different orthotopic models of glioblastoma with a VEGF-targeted kinase inhibitor, cediranib. Using intravital microscopy, molecular techniques, and magnetic resonance imaging (MRI), we measured survival, tumor growth, edema, vascular morphology and function, cancer cell apoptosis and proliferation, and circulating angiogenic biomarkers. We show by intravital microscopy that cediranib significantly decreased tumor vessel permeability and diameter. Moreover, cediranib treatment induced normalization of perivascular cell coverage and thinning of the basement membrane, as mirrored by an increase in plasma collagen IV. These rapid changes in tumor vascular morphology and function led to edema alleviation—as measured by MRI and by dry/wet weight measurement of water content—but did not affect tumor growth. By immunohistochemistry, we found a transient decrease in macrophage infiltration and significant but minor changes in tumor cell proliferation and apoptosis. Systemically, cediranib increased plasma VEGF and placenta growth factor levels, and the number of circulating CXCR4+CD45+ cells. However, by controlling edema, cediranib significantly increased survival of mice in the face of persistent tumor growth.
In conclusion, anti-VEGF agents may be able to improve survival of patients with glioblastoma, even without inhibiting tumor growth.

Introduction

In a recent phase II study, we showed that cediranib (AZD2171, Recentin; AstraZeneca Pharmaceuticals,
Wilmington, DE), a potent panvascular endothelial growth factor (VEGF) receptor tyrosine kinase inhibitor, can transiently normalize tumor vessels in recurrent glioblastoma, [1] causing rapid changes in tumor vessel structure and function and alleviating cerebral edema evaluated by magnetic resonance imaging (MRI). In addition, cediranib reduced tumor-associated contrast enhancement to less than one half of the pretreatment value and reduced tumor bulk and mass effect in the majority of patients. Similar antiedema effects and improvement in progression-free and overall survival have also been reported in other VEGF-targeted clinical trials of recurrent glioblastoma [2-4]. These encouraging findings have led to randomized phase II and III studies with anti-VEGF agents in combination with chemotherapy and as monotherapy. However, the underlying mechanisms for their success remain poorly understood. Although the antiedema effects of VEGF-targeted therapy are widely accepted, its contribution to the survival benefits remains unknown. Thus these clinical data raise an important question: Is controlling edema by anti-VEGF agents sufficient to increase survival? In patients, this determination is difficult because MRI-based determinations of tumor progression are confounded by changes in vascular permeability after anti-VEGF therapy [5, 6]. To address this question, we used intravital microscopy, histology, molecular and cellular marker analyses, and functional MRI to investigate the effects of cediranib in three orthotopic models of glioblastoma in mice (two human gliomas—U87 and U118—and a highly invasive rat glioma, CNS1).

Results

Methods

Animal models and cell lines

We implanted cranial windows into nude mice as previously described [7]. After 1 week, we implanted small fragments (0.2 to 0.3mm diameter) of U87 or U118 or CNS1 tumors superficially into the left cerebral cortex under the cranial window at a depth of 0.4 to 1 mm. To gain the ability to measure the tumor size in real-time, green fluorescence protein (GFP) was stably transfected into U87, U118, and CNS1 cells using a retroviral construct. All cell lines were maintained in DMEM medium with 10% fetal bovine serum. All experiments were approved by the Massachusetts General Hospital Subcommittee on Research Animal Care.

Tumor size monitoring and treatment protocols

U118-GFP, U87-GFP, and CNS1-GFP tumors were measured daily by intravital microscopy. Tumor size was measured by fitting an ellipse to the GFP signal (Appendix Fig A1). Tumor volume was calculated based on the equation:

$$\text{Tumor volume} = (\text{long axis}) \times (\text{short axis})^2 \times \pi/6 \quad (1)$$

After reaching a diameter of 2.5 mm (or to a volume 6 to 8 μl) for U87 and U118 and 2 mm for CNS1—defined as day 0—treatment was started with either cediranib, dexamethasone (Baxter Healthcare Corp, Deerfield, IL), or saline. Cediranib dissolved in 1% Tween was administered via oral gavage atthe dose of 6mg/kg each day [8]. Dexamethasone was administered intraperitoneally at a dose of 10 mg/kg each day. For all cediranib studies, mice bearing gliomas were treated until reaching the end point with cediranib or Tween. For all dexamethasone studies, mice bearing gliomas were treated every day until reaching the end point with dexamethasone or saline. For survival studies, lethargic mice or mice with severe neurologic symptoms were humanely euthanized.

Histology and immunostaining

Tumor-bearing mice were perfusion-fixed by infusion of 4% paraformaldehyde through the left ventricle. For immunofluorescence analysis, mouse brains were postfixed for 1 hour in 4% formaldehyde in phosphate buffered saline (PBS) followed by incubation in 30% sucrose in PBS overnight at 4°C and subsequent mounting in freezing media (OCT, Tissue-Tek, Torrance,CA). Brains were sectioned every 20μm and incubated for 4 hours at room temperature in a mixture of anti-CD31 antibody (2.5 μg/mL; clone2H8, Millipore Chemicon International, Temecula, CA) and either anti-NG2 antibody (2.5 μg/mL; Millipore), anti-CD13 antibody (1.7 μg/mL, clone R3-63, Serotec R3-63; AbD Serotec, Morphosys UK Ltd, Oxford, UK), antilaminin antibody (0.95μg/mL; Dako, Carpinteria, CA), or anti-collagen IV antibody (0.5 μg/mL; Millipore) in 0.2% Triton-X100% and 5% normal horse serum (NHS) in PBS. After several washes in PBS, tissue sections were incubated for 1 hour at room temperature with 1:400 dilutions of Cy5-conjugated antiarmenian hamster antibody and Cy3 conjugated antirat or antirabbit antibody in 0.2% Triton-X 100% and 5% NHS in PBS. After several washes in PBS, tissues were postfixed in formaldehyde and mounted with 4'-6-diamidino- 2-phenylindole–containing mounting media (Vectashield, VectorLabs, Burlingame, CA) for confocal microscopy. Brain sections were stained also for CD11b and F4/80 incubating allophycocyanin (CD11b, cloneM1/70) or phycoerythrin (F4/80, clone BM8) –conjugated primary antibodies (BD Biosciences Pharmingen, Franklin Lakes, NJ) for 1 hour at room temperature in 5% NHS in PBS. Apoptotic cells were detected using ApopTag Red In Situ Apoptosis Detection Kit following manufacturer's (Millipore) protocol. For the detection of cell proliferation, mice were injected intraperitoneally with 1 mg of 5-bromo-2-deoxyuridine (BrdU; Sigma-Aldrich, St Louis, MO) 24 hours before sacrifice. For the detection of the incorporated BrdU from the U87-bearing brain sections, antigen retrieval was performed by incubating tissue sections in pH6 citrate antigen retrieval solution (Dako) at 95°C for 10 minutes before staining sections with Alexa Fluor 546 conjugated anti-BrdU antibody (2μg/mL; clonePRB-1, InvitrogenMolecularProbes,Carlsbad,CA) for 1 hour at room temperature in 0.2%Triton-X100%and 5%NHS in PBS. Quantification of the stained area was performed using an in-house segmentation algorithm (MATLAB, The

Mathworks, Natick, MA). Analysis of vascular proximity was performed by fitting the intensity profile around the vessels (determined by CD31 staining) to an exponential function ($I = Ae^{-x/L} + C$), where I = pixel intensity, x = distance from vessels (1 to 10 μm), and L = characteristic length. This method was used for assessment of the perivascular cell proximity to the vessel wall, as well as basement membrane thickness.

MRI-based measurement of permeability, edema, and tumor growth

All magnetic resonance images were acquired on a 9.4 Tesla MRI scanner (Bruker Biospin, Billerica, MA). Animals were anesthetized with a 50:50 mixture of O2 and medical air plus 1.5% isoflurane and placed prone in a cradle. Either a custom-built 1-cm transmit/receive surface coil, positioned on the head of the animals, or a transmit/receive birdcage mouse-head coil were used to acquire the images. T2-weighted rapid acquisition with relaxation enhancement (RARE) images were acquired to assess the tumor volume. The acquisition parameters
were as follows: TE = 10, RARE factor = 16, TR = 3,000 msec, NA = 4, 11 image slices, 0.5-mm slice thickness, 150-μm in-plane resolution. Tumor volume was determined from the T2 hyperintense regions of the brain, measured using an in-house segmentation algorithm (MATLAB). T2 relaxation maps were generated from multiecho spin-echo images and used to assess tumor edema. Acquisition parameters were as follows:
TE " 10 msec, 10 echoes, TR " 2,500 msec, 11 image slices, 0.5 mm slice thickness, 150 mm in-plane resolution, NA " 2. Voxelwise exponential fitting of the image signal intensity as a function of echo-time was performed
(MATLAB) to determine T2 relaxation time maps. Tumor blood vessel permeability (Ktrans) was assessed from Dynamic Contrast Enhanced (DCE) magnetic resonance images. The DCE sequence consisted of a T1-weighted gradient-echo sequence with TE " 2.5 msec, TR = 50msec, flip angle = 35°, FOV = 1.92 cm, matrix = 96 X 96 (in-plane resolution = 200 μm), 0.5-mm slice thickness, one image slice, 70 to 100 repetitions, temporal resolution = 4.8 seconds. A total of 50 to 100 μL of 100 mmol/L Gd-DTPA (0.2 to 0.4 mmoles/kg) was injected approximately 30 seconds after commencement of the DCE

imaging sequence. The signal intensity in the tumor region of interest (ROI) was analyzed using an in-house written MATLAB program, which models the tumor signal enhancement using the two-compartment model of Tofts et al [9], to extract the volume transfer constant (Ktrans), the volume of the extravascular extracellular space (n_e), and the flux rate constant between the extravascular extracellular space and the blood plasma (k_{ep}). Briefly, the time dependence of tumor ROI signal intensity was fit to the equation:

$$S(t) = M_0 \frac{(1 - e^{-TR * R1(t)}) * \sin(\alpha)}{1 - \cos(\alpha) * e^{-TR * R1(t)}}$$

$$R1(t) = R1(0) + r1 * C_t(t)$$

$$C_t(t) = \frac{K_{trans}}{k_{ep}} C_p(0) \cdot (1 - e^{-k_{ep} \cdot t}) \quad (2)$$

Intravital multiphoton laser scanning microscopic analysis of vessel diameter, density, and relative hematocrit analysis

In vivomultiphoton laser scanning microscopic analysis of glioblastoma vessels was performed as described previously [10].The tumor area was identified by analysis of GFP constitutively expressed by U87, U118, and CNS1. Vessel angiography was performed after intravenous injection of 0.1 mL of 10mg/mL fluorescein isothiocyanate-dextran (500,000MW; Sigma). Hematocrit analysis was performed after injection of 150 μL of 50% hematocrit fluorescent RBCs (1,1'-dioctadecyl-3,3,3',3'-tetramethylindodicarbocyanine perchlorate, DiD; Invitrogen). Two adjacent areas were imaged by acquiring three dimensional stacks (resolution, 2.4X2.4X2.5μm/pixel). Tumor volume was segmented using an in-house algorithm (MATLAB). Vessels were traced as described [11].Hematocrit analysis was performed by scanning through a line perpendicular to the vessel direction and extracting RBC velocity and flux. Hematocrit was calculated based on the equation:

$$Ht = \frac{MCV \times flux}{\frac{d^2}{\pi \frac{}{4}} V_{rbc}}$$

For vessels with velocity lower then10μm/s, relative hematocrit was measured by counting the number of RBCs in the vessel in a snapshot.

Water content analysis by Dry/Wet weight measurements

Anesthetized mice were euthanized by cervical dislocation and the brains were collected. Brains were dissected into several compartments: tumor, ipsilateral hemisphere, and contralateral hemisphere. Tissues were weighed immediately and dried in a vacuum for up to 2 weeks. Weights were collected throughout the drying period until the final dry weight was established. Water content was calculated as follows:

Water content = (wet weight) – dry weight)/wet weight (4)

Statistical analysis

Data are expressed as mean ± standard error of the mean. The principal statistical test was the *t* test (two-tailed with unequal variance). We analyzed the experiments involving multiple comparisons using repeated measures
multivariate analysis of variance followed by posthoc within and between groups hypothesis testing (SYSTAT 12; SYSTAT Soft Inc, Chicago, IL). We used the nonparametric log-rank test for survival studies.We considered a P value of less than .05 to be statistically significant.

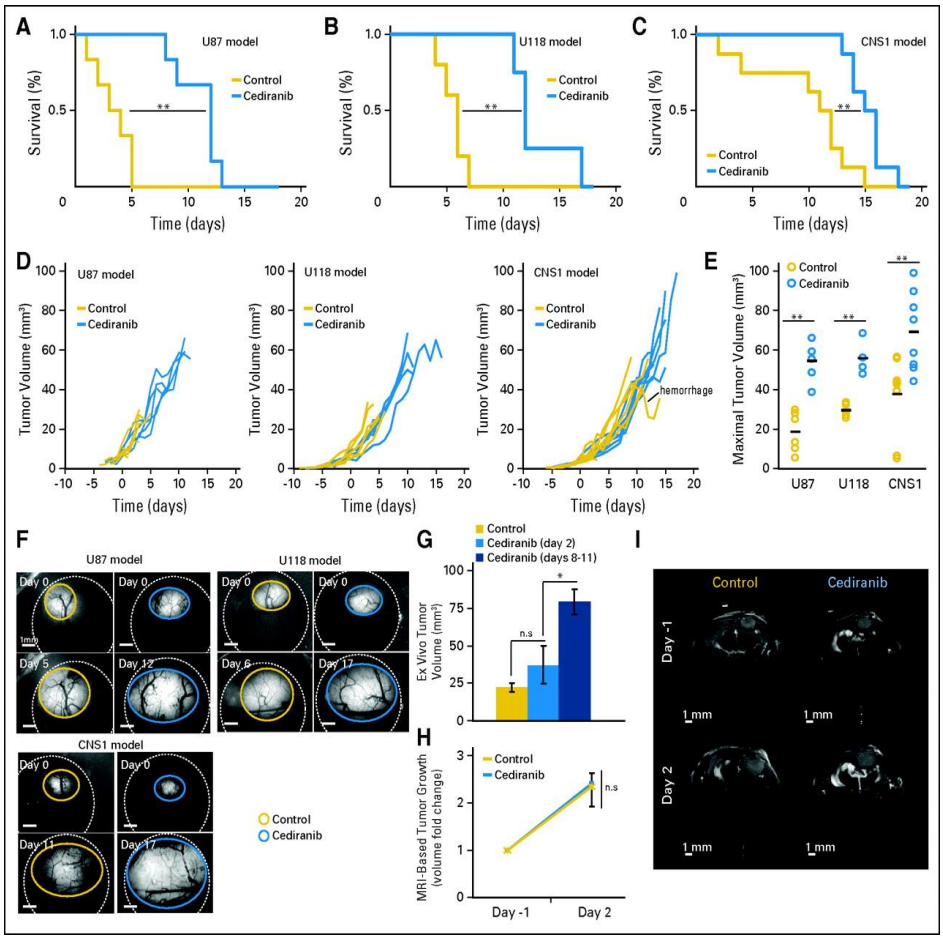

Fig 1| Cediranib treatment leads to increased survival without effects on tumor growth. Cediranib (6 mg/kg of body weight per day) treatment leads to statistically significant survival benefit in U87 (A; **P < .001, n = 6), U118 (B; **P < .01, n = 4), and CNS1 (C; **P < .01, n = 8). (D) Single animal tumor growth curves acquired by fluorescence microscopic imaging show the lack of growth delay after cediranib treatment. (E) Maximal tumor volume (measured at end point). Cediranib-treated animals survived with statistically significantly larger U87 (**P < .001, n = 6), U118 (**P < .001, n = 4), and CNS1 (**P < .001, n = 8) tumors. (F) Representative intravital fluorescence microscopic image of U87, U118, and CNS1 at first and last time points. (G) U87 tumor volume measured ex vivo at day 2 and day 8 to 11 in control and cediranib-treated animals shows the lack of tumor growth delay with cediranib treatment at day 2 (P (> .05, n = 5) (H) Cediranib treatment does not affect U87 tumor growth assessed by magnetic resonance imaging (volumes measured on T2 weighted stacks 0.15 mm XY resolution X 0.5 mm Z resolution; n = 3) (I) Representative T2-weighted single brain slices of cediranib- and control-treated animals bearing U87 tumors.

Results

Monotherapy with cediranib significantly increases survival of mice with glioma

GFP-expressing U87, U118, and CNS1 tumors were orthotopically grown into the cerebral cortex of nude mice bearing cranial windows. We started treatment when gliomas reached a diameter of 2 to 2.5 mm, measured by intravital microscopy. Cediranib increased survival in all the tumor models (Figs 1A through 1C), even though tumor growth was not affected at the dose used (Figs 1Dthrough 1I). Because cediranib-treated mice had longer survival without a delay in tumor growth, their tumors were twice as large as those in the control group at the experiment end point (Fig 1E). Untreated mice tended to die suddenly, despite their healthy appearance and relatively small tumor size. In contrast, mice treated with cediranib survived longer and slowly became cachectic and had to be euthanized.

Mechanism of action of cediranib monotherapy is alleviation of edema

Although multifactorial, one of the major causes of death of patients with glioblastoma is cerebral herniation (seen in more than 60% of patients), which is primarily caused by cerebral edema and intracranial hypertension [12]. The clinical effects of cerebral edema have been extensively studied in preclinical models of vasogenic and cytotoxic edemas. Cerebral physiology was found to be hypersensitive to increase in water content, which leads to intracranial hypertension, clinical deterioration, andmorbidity [13-15]. A major contributor to this edema is increased vascular permeability and accumulation of inflammatory cells (macrophages). Cediranib inhibits both VEGF receptor 2 (VEGFR2) signaling in endothelial cells (a major determinant of vascular Permeability [16]) and VEGF receptor 1 (VEGFR1) signaling (a key pathway in monocyte/macrophage recruitment to tumors [17]). Hence we hypothesized that the survival benefits seen in our models are primarily due to the alleviation of cerebral edema by cediranib. To investigate the mechanisms of cediranib survival benefit, we focused on the U87model, in which the cancer cells do not express functional VEGF receptors (data not shown). We assessed edema directly by the dry/wet weight ratio of

the brain ex vivo (Fig 2A) and indirectly using MRI-T2 maps in vivo (Fig 2B). Cediranib significantly decreased tumor water content at day 2, but this effect was transient, reverting to control levels at day 8 through 11 (Fig 2A). This suggests that cediranib could no longer control cerebral edema caused by the tumor enlargement at later time points.

Brain edema alleviation can increase survival despite tumor enlargement

To determine whether a transient decrease in edema alone is sufficient to increase survival, we treated a separate cohort of tumor bearing mice with dexamethasone, a corticosteroid commonly used to alleviate cerebral edema in patients with glioma. Dexamethasone treatment induced a modest enhancement of survival but also did not inhibit tumor growth (Figs 2D and 2F). Interestingly, the survival benefit provided by dexamethasone was not as pronounced as that of cediranib: the dexamethasone group had smaller tumors at end point than those in the cediranib-treated group. This is similar to an earlier report in which vascular normalization in an animal glioma model after dexamethasone treatment was also noted [18]. Next, we investigated the mechanisms by which cediranib treatment led to a more pronounced survival benefit.

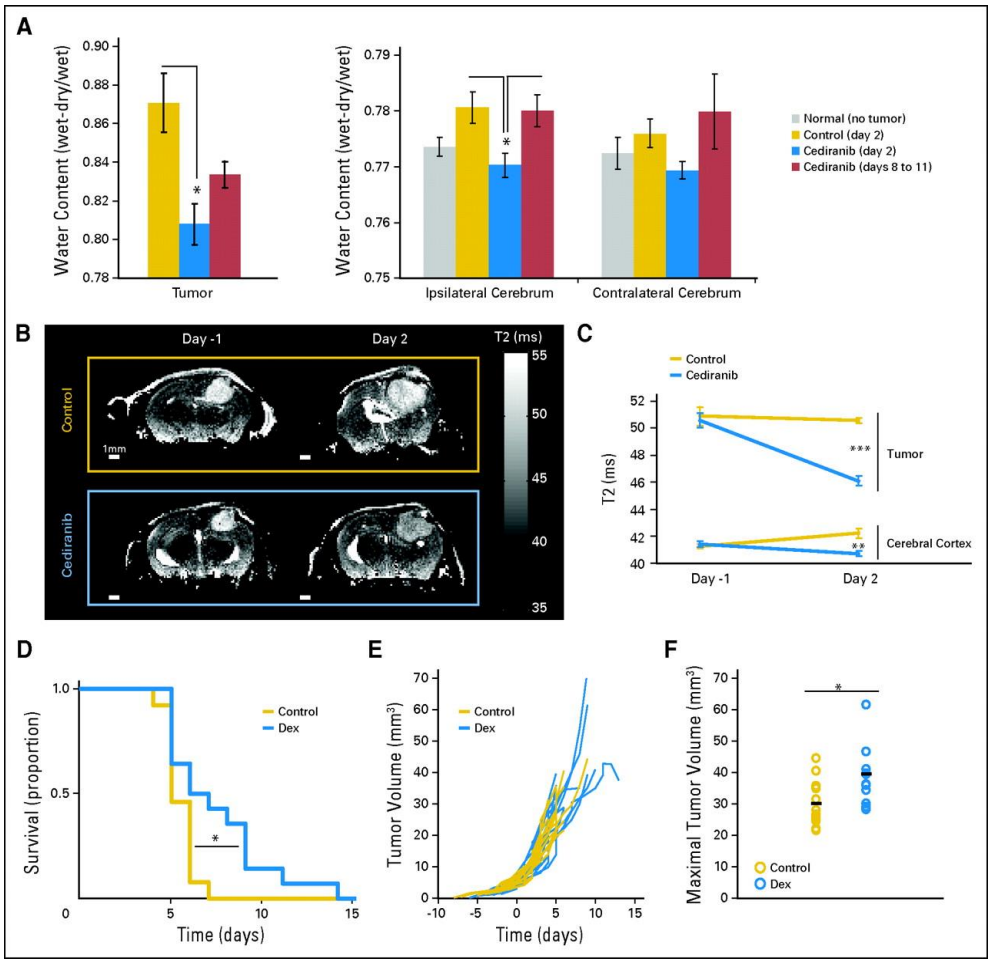

Fig 2.| Cediranib decreases glioblastoma-induced edema, and corticosteroid-mediated edema control increases survival without affecting tumor growth. (A) Water content measured by dry/wet weight ratio in the tumor and ipsilateral and contralateral cerebrum. Cediranib significantly decreased tumor and ipsilateral water content (*P < .05, n = 5). (B) Representative T2 maps of single brain slices used to evaluate edema (T2 correlates with water content). (C) Quantification of T2 in the tumor and the cerebral cortex. Cediranib significantly decreased T2 signal in the tumor (***P < .001) and the cerebral cortex (**P < .01). (D) Dexamethasone (Dex) (10 mg/kg each day) treatment leads to a statistically significant survival benefit (*P < .05, n = 14). (E) Individual tumor growth curves acquired by fluorescence microscopic imaging showing the lack of growth delay after Dex treatment. (F) Maximal tumor volume (measured at end point). Dex-treated animals survived with significantly larger tumors (*P < .05, n = 14).

Edema alleviation is caused by decreased glioblastoma vascular permeability associated with vascular normalization

To determine whether cediranib normalizes tumor vasculature in our models, we measured changes in the tumor vascular morphology and function after cediranib treatment. Similar to patients with glioblastoma, postcontrast MRI showed that cediranib significantly decreased Ktrans—a parameter dependent on vascular permeability—in the glioblastoma xenografts (Fig 3A). Furthermore, intravital microscopy measurements demonstrated that cediranib significantly decreased tumor vessel permeability and diameter, as well as vascular hemoconcentration (elevated hematocrit, Figs 3B through 3E and 4), all hallmarks of tumor vascular normalization [19]. Given the decrease in vessel diameter seen with intravital microscopic measurements after cediranib, we sought further evidence of normalization of the structure of glioblastoma vessels. Fluorescence immunohistochemistry showed that cediranib increased the proximity of perivascular to endothelial cells without significant changes in the extent of perivascular cell coverage (Figs 5A and 6). In addition, cediranib
treatment led to thinning of the vascular basement membrane (Fig 5B), similar to that seen after anti-VEGFR2 antibody therapy [20], and an increase in plasma collagen IV at day 2 (Appendix Fig A3). Additionally, cediranib-mediated vascular normalization was limited to a time window after which most of the functional and morphologic vascular parameters reverted to the abnormal phenotype. Specifically, at later time points, all normalization parameters reversed—including vascular permeability, vessel diameter, basement membrane thickness, and hemoconcentration—except for pericyte proximity

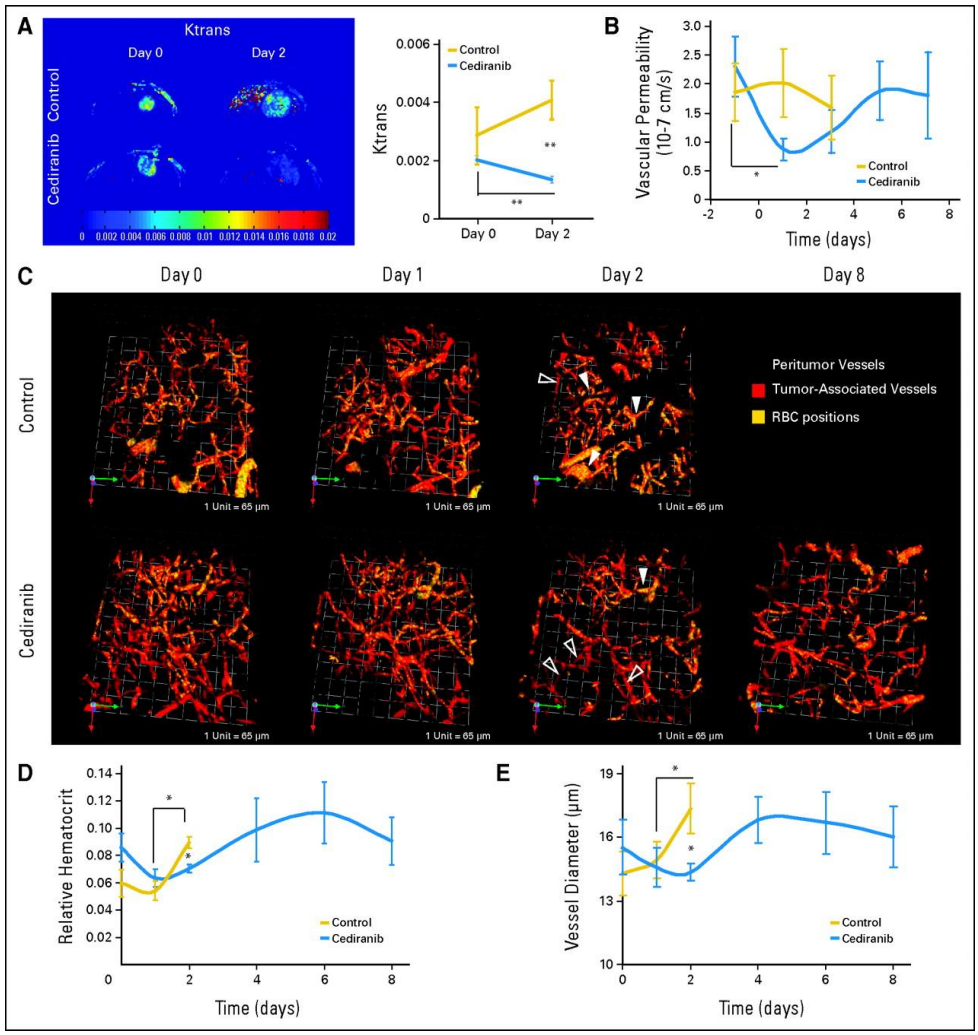

Fig 3| Cediranib treatment normalizes glioma vessel morphology and function. (A) Cediranib treatment (6 mg/kg each day) leads to a statistically significant decrease in Ktrans (arbitrary units, $^{**}P < .05$, n = 4). (B) Cediranib significantly decreases vascular permeability measured by intravital microscopy ($^{*}P < .05$, n = 12). (C) Representative multiphoton laser scanning microscopy (MPLSM) three-dimensional reconstruction of the tumor (red) and peritumor vessels (gray) superimposed with RBC positions acquired through analysis of injected fluorescently labeled RBC. Control animals have predominantly hemoconcentrated vessels (closed arrows). Cediranib-treated animals have predominantly low hematocrit vessels (open arrows). (D) Mean and SE of tumor vessel relative hematocrit measured by MPLSM. Cediranib significantly decreases relative hematocrit ($^{*}P < .05$, n = 4). (E) Cediranib transiently but significantly decreases vessel diameter measured by MPLSM ($^{*}P < .05$ n = 4).

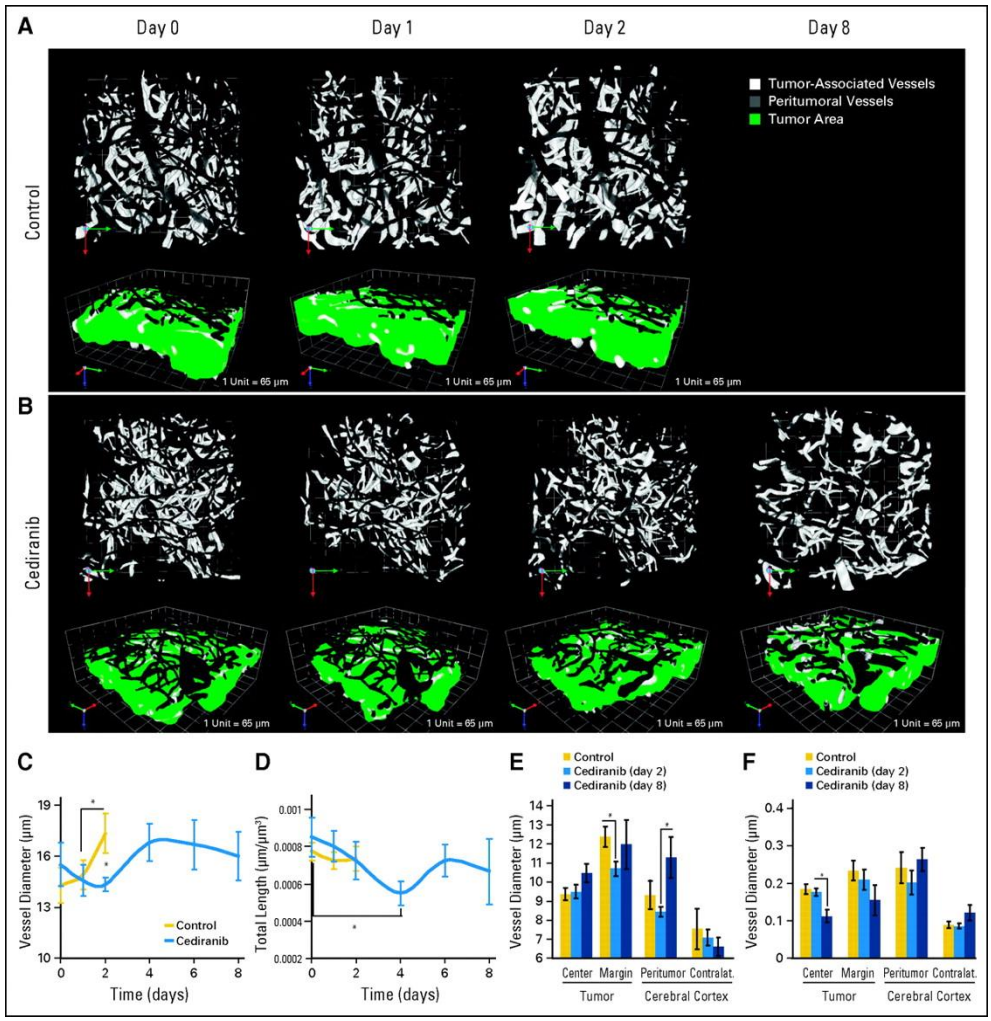

Fig 4| Cediranib decreases vessel diameter at early time points and decreases vessel density at later time points. (A, B) Representative multiphoton laser scanning microscopic (MPLSM) three-dimensional reconstruction of the tumor (white) and peritumor vessels (gray) showing the effects of (A) control versus (B) cediranib treatment on vessel diameter. (C) Cediranib transiently but significantly decreases vessel diameter measured by MPLSM (*P < .05, n = 4). (D) Cediranib significantly decreases vessel density (length) measured by MPLSM (*P < .05, n = 4). (E) Cediranib decreases vessel diameter at the tumor margin at day 2 (measured by immunostaining for CD31 endothelial staining; *P < .05, n = 9). (F) Cediranib decreases microvascular density at the tumor center at day 8 (measured by immunostaining for CD31; *P < .05, n = 9).

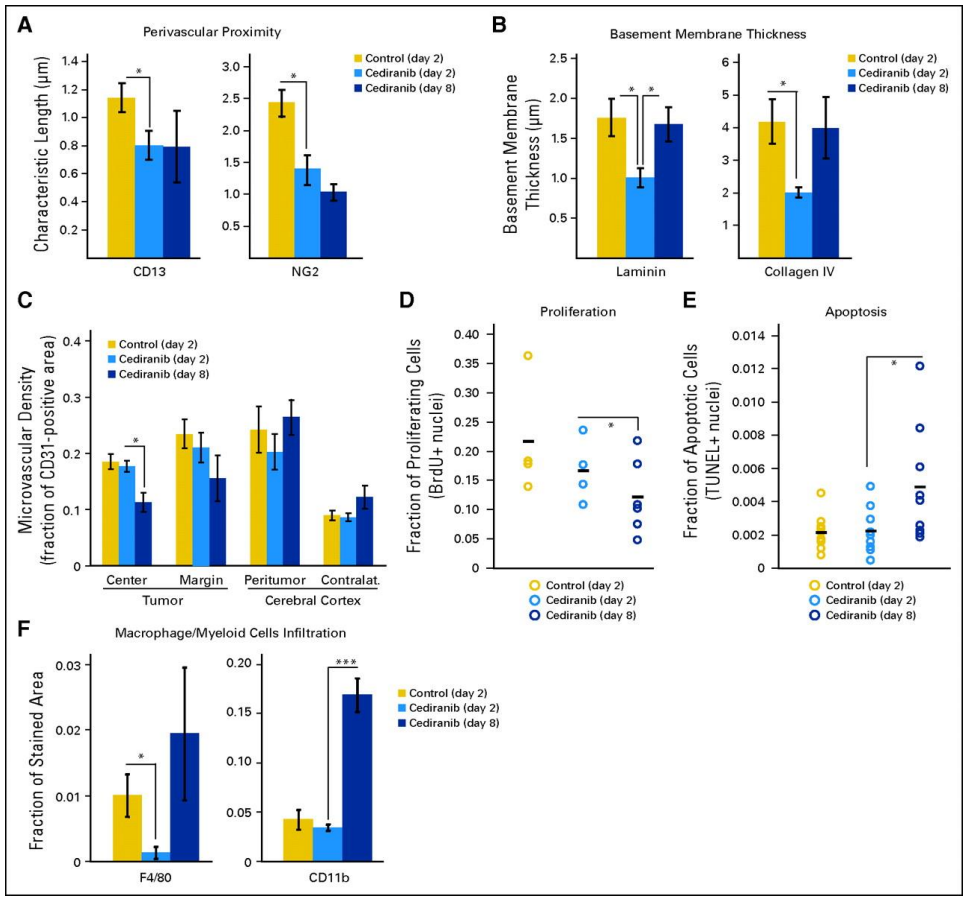

Fig 5| Cediranib treatment decreases macrophage infiltration and normal vessel wall structure; at day 8, microvascular density is decreased, tumor cell proliferation is decreased, and apoptosis is increased. (A) Cediranib decreases the characteristic length describing the distance between perivascular cells and the vessel wall (measured by immunostaining for CD13, **P* < .05, n = 5; and NG2, **P* < .05, n = 9). (B) Cediranib transiently but significantly decreases basement membrane thickness at day 2 (measured by immunostaining for laminin and collagen IV; **P* < .05, n = 5). (C) Cediranib decreases microvascular density at the tumor center at day 8 (measured by immunostaining for CD31 endothelial staining; **P* < .05, n = 9). (D) A total of 1 mg/mouse of 5-bromo-2-deoxyuridine (BrdU) was injected intraperitoneally 24 hours before the end point. The fraction of nuclei with incorporated BrdU is quantified and plotted for each animal. Cediranib significantly decreased proliferation only at day 8 (**P* < .05, n = 4). (E) Terminal deoxynucleotidyl transferase–mediated (TUNEL) staining was used to assess apoptosis of tumor cells. The fraction of TUNEL-positive nuclei was plotted for each animal. Cediranib significantly increased apoptosis at day 8 (**P* < .05, n = 9). (F) Cendiranib transiently but significantly decreases macrophages infiltration at day 2 (measured by immunostaining for F4/80; **P* < .05, n = 5). Myeloid cells infiltration is significantly increased at day 8 (measured by immunostaining for CD11b; ***P* < .0001, n = 5).

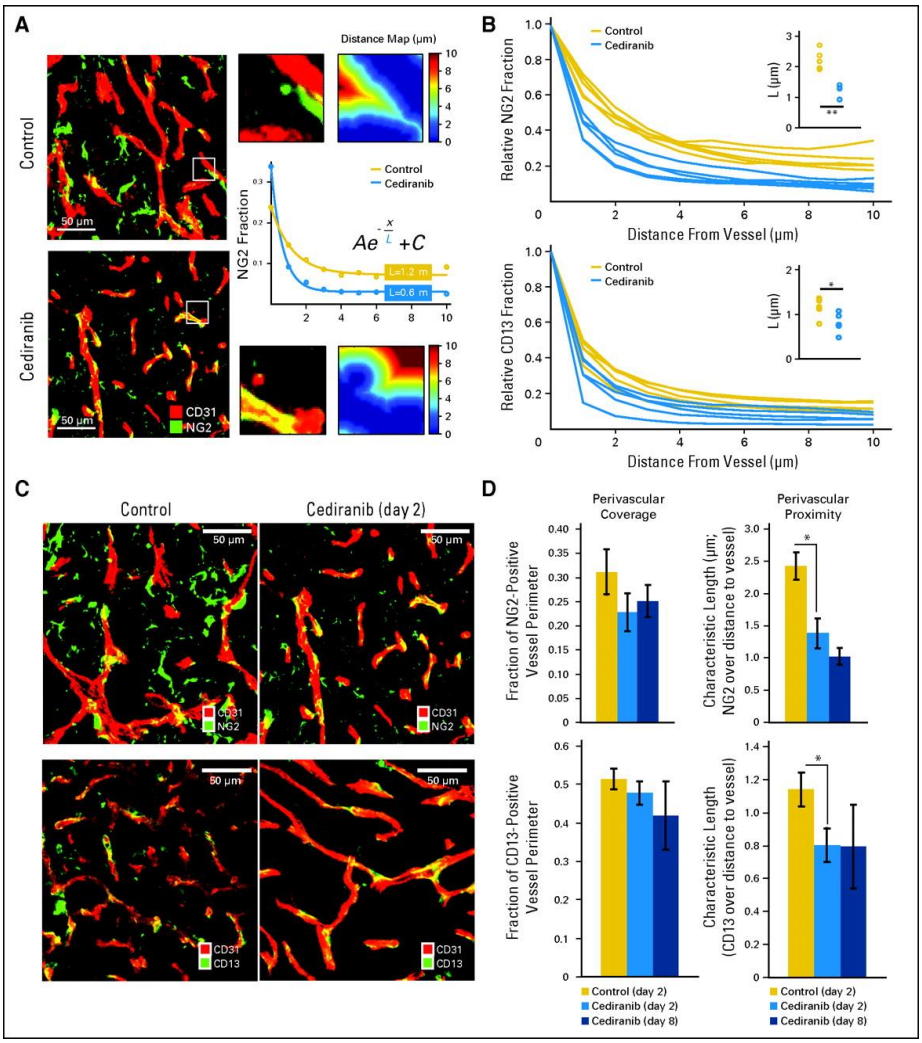

Fig 6| Quantification of pericyte coverage and proximity. (A) Representative immunohistochemistry fields of CD31- (endothelial marker) and NG2- (pericyte marker) stained tumor vessels. The fraction of NG2-positive pixels was analyzed at various distances from the vessel wall (1 μm to 10 μm), and the data were fit to an exponential function, yielding the quantity L, the characteristic extension of stain from the wall. (B) The fraction of NG2- or CD13- (pericyte marker) positive pixels was analyzed at various distances from the vessel wall. The average signal for each animal (based on five areas) is plotted, showing a difference between cediranib-treated and control animals. (C) Representative field of CD31- (endothelial marker) and NG2- (top panels) or CD13- (bottom panels) stained tumor vessels with control or cediranib treatment at day 2. (D) Cediranib significantly decreased pericyte distance from endothelial cells without changing the extent of perivascular cell coverage (NG2, $P < .05$, n = 9; CD13, $P < .05$, n = 5).

Transient nature of the vascular normalization and edema control may be caused by activation of inflammatory mechanisms independent of VEGF and angiogenesis

In contrast to early time points, when cediranib normalized vessel function without detectable pruning of vessels, extended cediranib treatment decreased microvascular density in the center of the tumors (Fig 5C). This was associated with a modest but significant increase in tumor cell apoptosis and decrease in tumor cell proliferation (Figs 5D and 5E). However, the ratio of proliferating to apoptotic tumor cells remained high (more than 20-fold), explaining the sustained tumor growth rate. This result is consistent with other reports, in which a reduction of microvascular density was achieved without significant reduction of tumor growth [21]. In addition, immunohistochemical analyses showed that cediranib significantly reduced macrophage infiltration (Fig 5F). This effect might be due to direct VEGFR1 blockade by cediranib and/or could be secondary to normalization of the tumor vessels and environment. However, infiltration of macrophages as well as other myeloid cells significantly increased at later time points during cediranib treatment (Fig 5F). The accumulation of these inflammatory cells may be involved in the escape from vascular normalization and edema control at the later time points [22]. Finally, preclinical studies have also suggested that antiangiogenic therapy (eg, sunitinib) exerts systemic effects, causing elevation in multiple circulating angiogenic markers, which can promote tumor growth [17, 23, 24]. In clinical studies, we found that cediranib increased circulating angiogenic markers in patients with recurrent glioblastoma [1]. In mice with U87 gliomas, we found that cediranib significantly increased the plasma levels of both mouse and human (tumor-derived) placenta growth factor and human VEGF but not mouse VEGF. Cediranib also rapidly increased the number of circulating CXCR4+CD45+ cells (Appendix Fig A2). Future studies should establish whether activation of systemic inflammatory and/or angiogenic markers are causally related to the persistent growth of gliomas through antiangiogenic treatment.

Discussion

In summary, our results show that cediranib decreases edema by normalizing tumor vasculature, increasing survival in brain tumor models—even in the face of persistent glioblastoma growth. We hypothesize that this may be a "class effect" of agents that target theVEGF signaling pathway, including tyrosine kinase inhibitors and antibodies. Moreover, our preclinical observations regarding reduction in vascular permeability, vessel diameter, and vasogenic cerebral edema mirror the clinical findings with cediranib monotherapy inpatients with recurrent glioblastoma obtained by vascular MRI. In the latter study, we also observed extensions of progression-free and overall survival, relative to historical controls, in patients with rapid decreases in vascular permeability after cediranib treatment [25]. However, our observations in preclinical model systems do not exclude thepossibility that anti-VEGF therapy in human tumors may improve survival by mechanisms beyond alleviation of edema. In fact, thevascular normalization window induced by anti-VEGF therapeutics may enhance the sensitivity of tumors to the cytotoxic effects of ionizing radiation and chemotherapy by a number of potential mechanisms [8, 19, 20, 26]. Collectively, these results highlight the need for novel antiangiogenic and antitumor strategies to combat tumor resistance to anti-VEGF therapies and the need for methods to distinguish antitumor, antiedema, and antivascular effects in patients.

References

1. Batchelor TT, Sorensen AG, di Tomaso E, et al. AZD2171, a pan-VEGF receptor tyrosine kinase inhibitor, normalizes tumor vasculature and alleviates edema in glioblastoma patients. *Cancer Cell.* Jan 2007;11(1):83-95.

2. Cloughesy TF, Prados MD, Wen PY, et al. A phase II, randomized, non-comparative clinical trial of the effect of bevacizumab alone or in combination with irinotecan (CPT-11) on 6-month progression free survival in recurrent, treatment-refractory glioblastoma *J Clin Oncol.* 2008;26S:abstract 2010b.

3. Pope WB, Lai A, Nghiemphu P, Mischel P, Cloughesy TF. MRI in patients with high-grade gliomas treated with bevacizumab and chemotherapy. *Neurology.* Apr 25 2006;66(8):1258-1260.

4. Vredenburgh JJ, Desjardins A, Herndon JE, 2nd, et al. Phase II trial of bevacizumab and irinotecan in recurrent malignant glioma. *Clin Cancer Res.* Feb 15 2007;13(4):1253-1259.

5. Norden AD, Young GS, Setayesh K, et al. Bevacizumab for recurrent malignant gliomas: efficacy, toxicity, and patterns of recurrence. *Neurology.* Mar 4 2008;70(10):779-787.

6. Sorensen AG, Batchelor TT, Wen PY, Zhang WT, Jain RK. Response criteria for glioma. *Nat Clin Pract Oncol.* Nov 2008;5(11):634-644.

7. Yuan F, Salehi HA, Boucher Y, Vasthare US, Tuma RF, Jain RK. Vascular permeability and microcirculation of gliomas and mammary carcinomas transplanted in rat and mouse cranial windows. *Cancer Res.* Sep 1 1994;54(17):4564-4568.

8. Wedge SR, Kendrew J, Hennequin LF, et al. AZD2171: a highly potent, orally bioavailable, vascular endothelial growth factor receptor-2 tyrosine kinase inhibitor for the treatment of cancer. *Cancer Res.* May 15 2005;65(10):4389-4400.

9. Tofts PS, Brix G, Buckley DL, et al. Estimating kinetic parameters from dynamic contrast-enhanced T(1)-weighted MRI of a diffusable tracer: standardized quantities and symbols. *J Magn Reson Imaging.* Sep 1999;10(3):223-232.

10. Brown EB, Campbell RB, Tsuzuki Y, et al. In vivo measurement of gene expression, angiogenesis and physiological function in tumors using multiphoton laser scanning microscopy. *Nat Med.* Sep 2001;7(9):1069-1069.

11. Tyrrell JA, di Tomaso E, Fuja D, et al. Robust 3-D modeling of vasculature imagery using superellipsoids. *IEEE Trans Med Imaging.* Feb 2007;26(2):223-237.

12. Silbergeld DL, Rostomily RC, Alvord EC, Jr. The cause of death in patients with glioblastoma is multifactorial: clinical factors and autopsy findings in 117 cases of supratentorial glioblastoma in adults. *J Neurooncol.* Apr 1991;10(2):179-185.

13. Manley GT, Fujimura M, Ma T, et al. Aquaporin-4 deletion in mice reduces brain edema after acute water intoxication and ischemic stroke. *Nat Med.* Feb 2000;6(2):159-163.

14. Papadopoulos MC, Manley GT, Krishna S, Verkman AS. Aquaporin-4 facilitates reabsorption of excess fluid in vasogenic brain edema. *FASEB J.* Aug 2004;18(11):1291-1293.

15. Thiagarajah JR, Papadopoulos MC, Verkman AS. Noninvasive early detection of brain edema in mice by near-infrared light scattering. *J Neurosci Res.* Apr 15 2005;80(2):293-299.

16. Dvorak HF. Vascular permeability factor/vascular endothelial growth factor: a critical cytokine in tumor angiogenesis and a potential target for diagnosis and therapy. *Journal of Clinical Oncology.* Nov 1 2002;20(21):4368-4380.

17. Fischer C, Jonckx B, Mazzone M, et al. Anti-PlGF inhibits growth of VEGF(R)-inhibitor-resistant tumors without affecting healthy vessels. *Cell.* Nov 2 2007;131(3):463-475.

18. Badruddoja MA, Krouwer HG, Rand SD, Rebro KJ, Pathak AP, Schmainda KM. Antiangiogenic effects of dexamethasone in 9L gliosarcoma assessed by MRI cerebral blood volume maps. *Neuro Oncol.* Oct 2003;5(4):235-243.

19. Jain RK. Normalization of tumor vasculature: an emerging concept in antiangiogenic therapy. *Science.* Jan 7 2005;307(5706):58-62.

20. Winkler F, Kozin SV, Tong RT, et al. Kinetics of vascular normalization by VEGFR2 blockade governs brain tumor response to radiation: role of oxygenation, angiopoietin-1, and matrix metalloproteinases. *Cancer Cell.* Dec 2004;6(6):553-563.

21. Svensson A, Backman U, Fuchs D, Christofferson R, Azarbayjani F. Angiogenesis can be reduced without significant reduction of tumor growth. *Anticancer Res.* Nov-Dec 2007;27(6B):3883-3889.

22. Shojaei F, Ferrara N. Refractoriness to antivascular endothelial growth factor treatment: role of myeloid cells. *Cancer Res.* Jul 15 2008;68(14):5501-5504.

23. Ebos JM, Lee CR, Christensen JG, Mutsaers AJ, Kerbel RS. Multiple circulating proangiogenic factors induced by sunitinib malate are tumor-independent and correlate with antitumor efficacy. *Proc Natl Acad Sci U S A.* Oct 23 2007;104(43):17069-17074.

24. Shaked Y, Henke E, Roodhart JM, et al. Rapid chemotherapy-induced acute endothelial progenitor cell mobilization: implications for antiangiogenic drugs as chemosensitizing agents. *Cancer Cell.* Sep 9 2008;14(3):263-273.

25. Batchelor TT, Sorensen AG, di Tomaso E, et al. A multidisciplinary phase II study of AZD2171 (cediranib), an oral pan-VEGF receptor tyrosine kinase inhibitor, in patients with recurrent glioblastoma. *Proceedings of the AACR Annual Meeting.* 2008:Abstract 5531.

26. Padera TP, Kuo AH, Hoshida T, et al. Differential response of primary tumor versus lymphatic metastasis to VEGFR-2 and VEGFR-3 kinase inhibitors cediranib and vandetanib. *Mol Cancer Ther.* Aug 2008;7(8):2272-2279.

Supplemental information

Measurement of plasma soluble molecules

Peripheral blood was obtained from mice bearing orthotopic U87 tumors at baseline (pretreatment) and 2 and 8 days after cediranib treatment. Blood was collected in an EDTA-containing Vacutainer and spun down, and plasma was aliquoted and frozen immediately. Plasma analysis was carried out for circulating human vascular endothelial growth factor (VEGF) and PlGF using multiplex array plates from Meso-Scale Discovery (Gaithersburg, MD) and for mouse collagen IV, VEGF, and PlGF using enzyme-linked immunosorbent assay kits from Exocell Inc (Philadelphia, PA) and R&D System (Minneapolis, MN). Every sample was run in duplicate.

$CD45^+CXCR4^+$ hematopoietic precursor enumeration by flow cytometry

Flow cytometric analysis was performed after immunostaining of whole blood samples with rat anti-mouse CD45-peridinin-chlorophyll-protein complex and CXCR4-phycoerythrin antibodies (BD Biosciences Pharmingen, Franklin Lakes, NJ). $CXCR4^+CD45^+$ cells were enumerated as a fraction of blood circulating $CD45^+$ cells using an LSR-II flow cytometer (BD Biosciences).

Supplementary figures

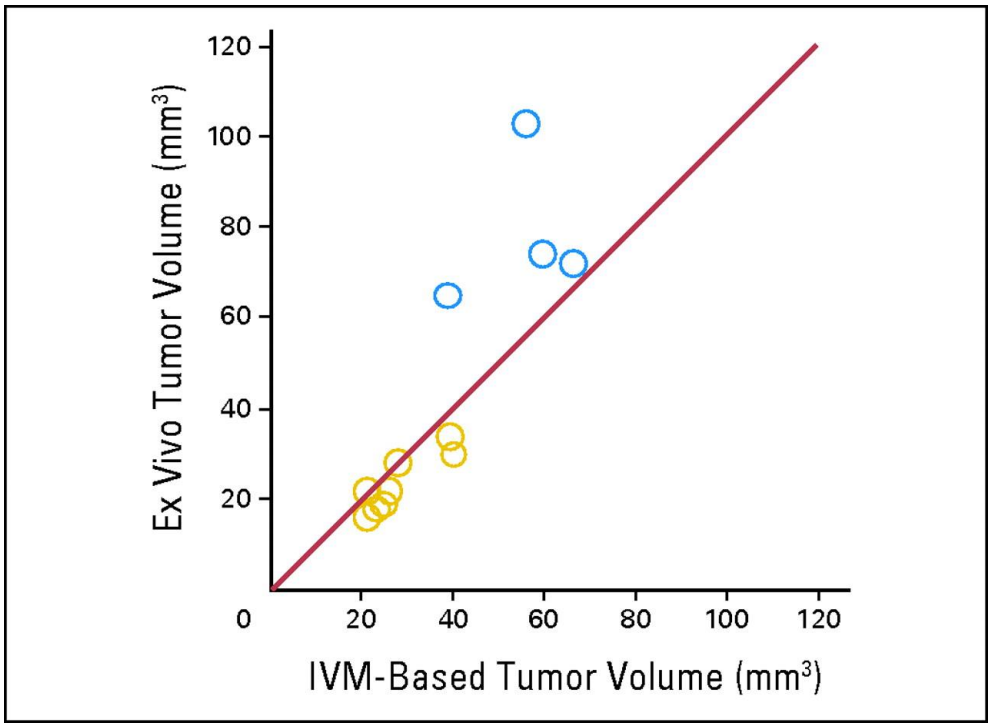

Fig A1| Validation of intravital measurements (IVM) of tumor volume. To validate the accuracy of the tumor volume estimation, we compared tumor volume measurements based on fluorescence microscopy imaging to actual tumor weights measured ex vivo. This comparison was performed for U87 tumors and showed that the green fluorescence protein–based estimations are highly accurate for small tumor volumes (approximately 20 μL reached at day 2, yellow circles, ie, when the comparisons with untreated tumors were performed), but showed a tendency to underestimate the tumor volume for larger tumor sizes (reached at day 8 after cediranib treatment, blue circles).

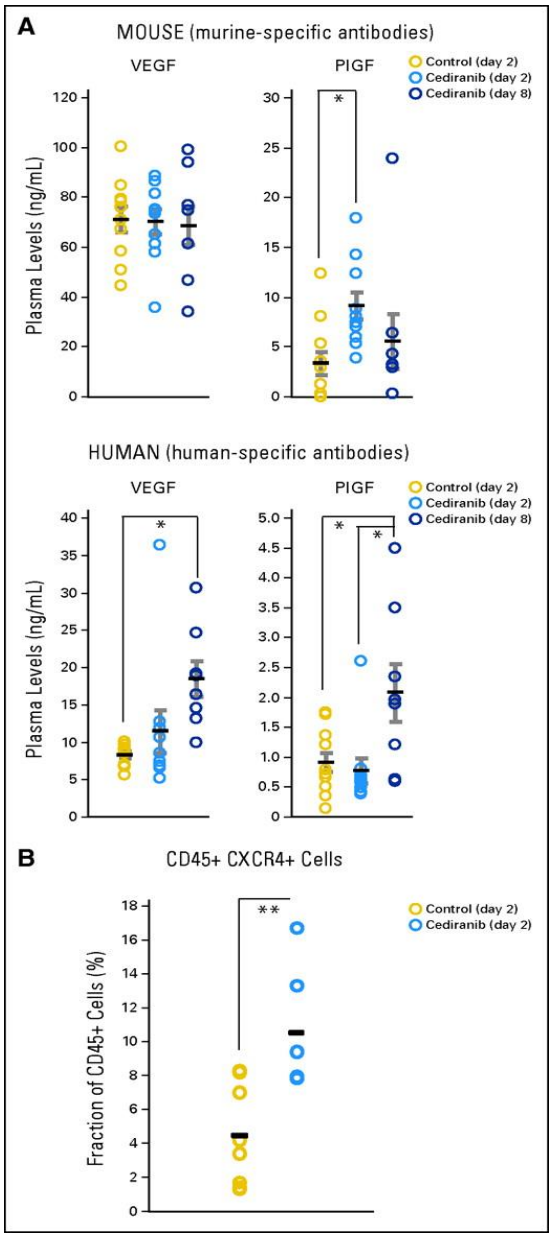

Fig A2| Systemic effects of cediranib treatment. Levels of human- and mouse-derived vascular endothelial growth factor (VEGF) and placenta growth factor (PlGF) in plasma of mice with orthotopic U87 gliomas, plotted for control treatment (day 2) and cediranib treatment (at days 2 and 8). Cediranib significantly increased the plasma levels of both mouse and human (tumor-derived) PlGF (*$P < .05$) and human VEGF (*$P < .05$), as well as the number of circulating $CXCR4^{+}CD45^{+}$ cells (**$P < .01$).

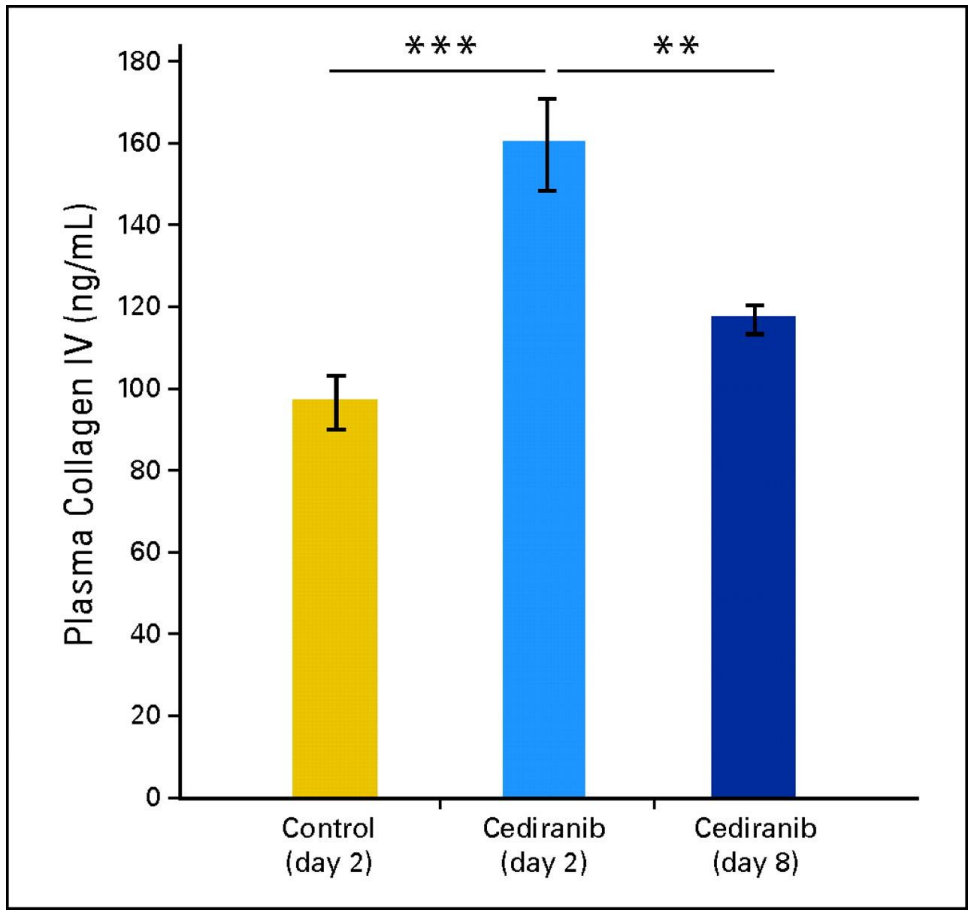

Fig A3| Changes in plasma collagen IV levels mirror thinning of the basement membrane. We hypothesized that the thinning of the vascular basement membrane owing to vascular normalization would increase the level of circulating collagen IV. Indeed, cediranib significantly increased the plasma levels of collagen IV at day 2 (***P < .001 cediranib day 2 *v* control). Collagen IV levels were decreased at day 8 (**P < .01 cediranib day 2 *v* cediranib day 8).

Chapter 8

Summary and general discussion

Until the 1960s surgery and radiotherapy dominated the field of cancer therapy. At that time it became clear that cure rates stabilized around 33%, even after radical local treatments. To combat these poor results, considered to be due to (micro) metastases, researchers set out to develop (adjuvant) systemic treatments [1]. In the following decades, multiple chemotherapies and targeted agents have been developed, which are used in today's clinic, either as mono- or combination therapies. These strategies have significantly improving response rates. However, we still we do not clearly understand how cancer cells learn to invade and create the metastases that are responsible for 90% of cancer mortality. Recently, we have become increasingly aware that the interplay between tumor cells and the host microenvironment plays a pivotal role in this process. It is the purpose of this thesis to unravel some of the involved mechanisms by answering the central questions as formulated in the introduction.

Part one:

I *Can we develop a set of animal models to mimic individual steps in the metastatic cascade and visualize stromal cells within these steps?*

To study distinct step of the metastasis in this thesis, we have developed two animal models that each represent part of the metastatic cascade as well as one model focusing on visualizing "passenger" stromal cells at a distant site. In **chapter 2** we describe the transient parabiosis skin transplantation model. In this model we use conjoint surgery to efficiently transplant the skin from a transgenic [ubiquitously expressing green fluorescent protein (GFP)] mouse in all cells except the bone marrow to a wild-type (non-GFP) mouse. The rationale was to transplant local skin stromal cells without contamination of immune (hematopoietic) cells during parabiosis. When we implanted tumors in this transgenic skin graft, the stromal cells recruited during tumor growth and progression were largely GFP+ [2]. This model was used to study spontaneously forming metastases from this tumor in distant organs and mimics the steps of spontaneous metastases from tumor shedding up to the outgrowth of micrometastases, taking

advantage of the fluorescent labeling of the passenger stromal cells. One limitation is that many of the current examples are ectopic tumor metastasis models. Another limitation is that the main focus is on mesenchymal stromal cells, rather than on immune cells, such as monocytes and macrophages. In **chapter 3** we present an isolated tumor perfusion model in mice specifically designed to study tumor cell and fragment shedding. In this renal perfusion model, (fluorescent/dsRed) tumors are implanted orthotopically or ectopically in the kidney of GFP transgenic mice. This model could also be adapted for other cancers such as the liver, ovarian or breast cancer. In this model, primary tumors are allowed to grow in a microenvironment where stromal cells express the GFP protein. To further analyze shedding from these tumors, the renal vein is cannulated and blood is collected and filtered, yielding single cells and tumor fragments for further studies [3]. Using the isolated tumor perfusion model, one might also quantify the result of treatments or genetic manipulation in this specific step of metastasis. Alternatively, one could use the collected cells/fragments for consecutive *in vivo* experiments in which the effect of drugs on tumor cell/clump shedding could be studied. In **chapter 4** we present a new model to study the interaction between stromal cells in the tumor microenvironment and tumor cells. The use of human carcinoma-associated fibroblasts (CAFs) enabled us to selectively deplete stroma cells using diphtheria toxin (which is highly toxic to human but not murine cells), without affecting mouse cancer cells or host-derived stromal cells [4]. The key advantage of this protocol over other existing methods is that one can obtain the ability to selectively deplete tumor stromal cells without affecting the microenvironment in the secondary site. One limitation is the fact that the model uses xenotransplantation of a human tumor in an immune-compromised mouse. This limitation could be overcome by developing transgenic models, if feasible, of tumor stromal cell depletion using genetic tools in syngeneic and orthotopic tumor models. Some of these animal models have been used in pre-clinical studies. For example, Zhang et al and Tian et al, developed transgenic mice expressing HSV-TK from the type I collagen promoter, enabling fibroblast apoptosis though treatment with ganciclovir [5, 6]. Iwano et al, generated transgenic mice expressing the suicide thymidine kinase gene, driven by the FSP1 promotor region. This model enables fibroblast elimination in the active phase of fibrogenesis [7]. These models might provide additional insights in tumor progression and metastases. However, the origin of

CAFs in the tumor microenvironment is known to be heterogeneous, for example through epithelial mesenchymal transition, activated by growth factors excreted by tumor cells or from bone marrow-derived stem cells, which might confound results in a selective depletion model.

II *Are stromal cell present in all steps of the metastatic cascade and can they mediate metastases formation?*

It has been well documented in literature that metastatic cancer cells preferentially grow in a secondary site with a permissive microenvironment [8-11]. In order to improve metastatic efficiency, it has been proposed that tumors create a congenial soil, by preparing a premetastatic niche using tumor-secreting factors [12-14]. In experimental metastasis models, it has been shown that metastatic cells can lodge to the lungs before their oncogenic transformation [15], and that metastatic cells form intravascular colonies in the lung, before invading the organ [16]. In **chapter 5**, we show that metastatic cells can actually bring their own soil from the primary tumor site to the lungs. Using the isolated tumor perfusion model [3], we collected cells shed by a primary tumor in the kidney of a mouse. Microscopic analysis revealed that stromal cells were present in fragments consisting of 6 or more cells and consecutive immunohistochemical assay showed markedly decreased apoptotic activity in these large clumps. Using an infusion models, we showed that tumor and stromal cells not only reside in the distant site two weeks after infusion, but also proliferate along with tumor resulting in a survival benefit in the heterogeneous sites. Next, we set out to characterize these tumor-associated fibroblasts. Using the previously described parabiosis skin transplant model [2] primary tumors were grown in a GFP positive skin transplant on a otherwise wild type mouse and GFP+ cells in the spontaneous metastases to the lungs were analyzed. Immunohistochemical assays showed colocalization of GFP with mesenchymal markers. Having demonstrated that host-stromal cells, predominantly fibroblasts, can be spontaneously shed and metastasize in clumps together with tumor cells and proliferate at the distant site, we next evaluated whether their selective depletion affects metastatic growth. To this end, we used human derived CAFs which can be selectively depleted by diphtheria toxin (DT) without

interfering with murine cell growth [4] and showed a decrease in the number of metastatic nodules in the CAF-depleted group, resulting in an increased survival of these mice. Given the known limitations of animal models to closely mimic human pathology, we next sought clinical relevance for this mechanism. To this end, we examined brain metastasis tissue samples from patients with a variety of primary tumors and compared them to primary malignant brain tumors (glioblastoma). Non-malignant brain tissue did not contain αSMA+ activated fibroblasts except for blood vessel-associated pericytes and smooth muscle cells. Nevertheless, we consistently detected benign-appearing αSMA+ stromal cells distributed focally within the brain metastases in the extravascular area in brain metastases of lung, breast, kidney and endometrial origin. Taken together, these results confirm the presence of host-derived stroma cells in all steps of the metastatic cascade and show a direct correlation with metastatic efficiency. Preexistence of a tissue-like structure containing fibroblasts as well as tumor cells may increase the viability of cancer cells in the circulation and the secondary site. In addition, these cells may support angiogenesis of metastatic nodules because CAFs express proangiogenic genes, including VEGF. The role of traveling stromal cells is likely to be most significant at the early stage of metastatic foci growth and their participation may be transient. Future studies should further evaluate the prevalence of this mechanism of metastasis in syngeneic and spontaneous animal models. The ectopic presence of tumor-associated fibroblasts in brain metastases in patients indicates a potential clinical relevance of this mechanism, which should also be explored further in future studies. It would be of interest to see whether evaluating circulating tumor clumps could complement circulating tumor cells studies [17]. Recent studies show that tumor-stroma interactions may not only affect tumor progression and patient prognosis, but also the response to chemotherapy or targeted therapy [18, 19], making neoadjuvant therapies of primary tumors a target to affect this process. *In vitro* and *in vivo* xenograft studies show a promising role for targeting fibroblast activation protein (FAP)[20, 21], but need to be validated in spontaneous (metastatic) tumor models. Also, identifying the adhesion molecules that are responsible for the adherence between the cancer cells and fibroblasts may provide new targets for antimetastasis therapy[22].

Part two:

III *Does the blood-brain-barrier affect HER2-targeted therapies in breast to brain metastases?*

Metastatic brain tumors account for the majority of intracranial neoplasms in adults and are a major cause of cancer mortality. These metastases originate predominantly from the lung (40-50%), breast (15-25%) and from melanoma (5-20%), and their frequency is increasing as systemic treatments gradually improve [23, 24]. After shedding from the primary tumor, tumor cells have to complete the previously discussed steps of the metastatic cascade before ultimately, they might enter the brain circulation. In this distant site, tumor cells are thought to arrest in the capillary bed[25], followed by early changes in the brain microenvironment [26]. In addition, stromal cells, such as fibroblast, originating from the primary site are involved in early metastatic outgrowth [27]. When metastatic tumors grow beyond a size of 2 mm, angiogenesis is induced within the brain parenchyma, which renders the BBB structurally and functionally compromised [28-30]. However, the disruption of the BBB is heterogeneous and barriers to drug delivery might still need to be overcome [31]. In **chapter 6** we study breast-to-brain metastases in a HER2 positive breast cancer cell line. To this end, we developed a novel animal model, enabling continuous monitoring of HER2+ tumor growth in the brain parenchyma using Gaussia luciferase (gluc) [32]. We first tested the effects of trastuzumab and lapatinib therapies on the growth of HER2 overexpressing breast tumors in the mammary fat pad and in the brain parenchyma. Although tumors in the mammary fat pad responded well to trastuzumab and lapatinib treatment, these inhibitors failed to control tumor growth in the brain. This indicates that the BBB and the brain microenvironment affect metastatic tumor growth within the brain. It is, however, important to note that although our direct brain parenchymal tumor implantation model allows for consistent tumor volume at treatment initiation as well as real-time evaluation of therapeutic efficacy using imaging and blood surrogate marker evaluation, it lacks early steps in the metastatic cascade such

as separation from primary tumor, invasion and release into blood vessels, and should ideally be reproduced in a spontaneous metastasis model.

IV *Does the addition of an antiangiogenic agent improve treatment outcome?*

The use of bevacizumab with trastuzumab and chemotherapy in HER2-positive metastatic breast cancer has shown some promise in phase II trials [33]. However, data on the efficacy of bevacizumab in the context of brain metastases are lacking, because these patients have often been excluded from clinical trials due to fear of an increased risk of cerebral hemorrhage after anti-VEGF therapy. The publication of reviews of large clinical datasets and two prospective clinical trials have substantially reduced this concern [34-36]. Nonetheless, the effects of dual blockade of VEGF and HER2 in brain metastases have not been examined in preclinical models. In **chapter 6** we study the effect of addition of an anti-VEGF pathway inhibitor to lapatinib and trastuzumab on HER2+ brain metastatic brain tumors. In concordance with the previously discussed results, lapatinib or trastuzumab monotherapy slowed tumor growth only by a few days. Trastuzumab prolonged survival by 7 days on average. DC101 (an anti-mouse VEGFR2 antibody) showed a significant delay in tumor growth. Even more marked was the response to combination treatment of DC101 and trastuzumab or lapatinib, resulting in an almost three fold increase in survival in the lapatinib/DC101 combination group. This impressive tumor growth delay was confirmed using MRI, bioluminescent imaging, and postmortem *ex vivo* multispectral brain imaging.

Preclinical and clinical evidence suggests a synergistic effect of the combination of trastuzumab and lapatinib. This is either attributed to a marked downregulation of the protein survivin, leading to enhanced tumor cell apoptosis following the combination of the two agents [37], or incomplete inhibition of the HER2 kinase after lapatinib monotherapy [38]. Two clinical trials support these results, but one of these is limited to an extracranial metastatic setting [39, 40]. Building on these results we asked if the synergistic effect of this combination would be influenced by the addition of a VEGFR2 inhibitor and found a remarkable response. In this particular experiment, mice treated with the combination of trastuzumab and lapatinib lived 2-fold longer than control mice, which

could be increased to about 2.5-fold by adding DC101. Meanwhile, mice treated with the triple combination lived 5-fold longer than control-treated mice. It is important, though, to note that 2 out of nine mice receiving triple-combination showed signs of toxicity and all tumors eventually escaped from therapy.

These results provide a strong rationale for the development of anti-VEGF therapy for brain metastases from HER2-positive breast cancer. Although the exact mechanism for the triple combination is not entirely clear, we propose that the antiangiogenic benefit seen with an anti-HER2 agent and VEGFR2 blockade is synergizing with the direct tumor cell cytotoxicity induced by two anti-HER2 agents. A clinical trial studying the efficacy of carboplatin and bevacizumab in progressive breast cancer brain metastasis is currently underway (http://clinicaltrials.gov identifier NCT01004172). In this trial, patients with HER2-positive disease will also be treated with HER2 inhibitors, which may provide clinical evidence for the approach presented here, as well as useful insight on toxicity associated with the combination of trastuzumab and bevacizumab. Notwithstanding these promising results, future studies will be needed to determine how these brain metastases eventually escape from this triple-combination therapy.

Regarding the signs of toxicity seen in the triple combination group in our experiment, special attention should be brought to this subject when translating to a clinical setting. Clinical trials with these drugs used as mono- or combination therapy provide extensive insight on their associated toxicities. Promising in this respect is the finding that combining trastuzumab and lapatinib did not increase the incidence of adverse effects compared with monotherapy [39].

V *What mechanisms contribute to the improved antitumor effect of antiangiogenic therapy in combination with HER2 inhibitors?*

In **chapter 6** we investigate the mechanisms behind the improved treatment outcomes described earlier. Immunohistochemical (IHC) analysis did not reveal any changes in tumor cell proliferation or apoptosis between groups. However, a significant increase in the necrotic fraction of tumor tissue was seen in the DC101 and the combination

treatment groups, indicating an enhanced antiangiogenic effect. Also, we found that HER2 inhibitors did not have an effect on micro-vascular density (MVD). Meanwhile, tumors treated with DC101 showed a decrease of both total and functional MVD of 50%, while tumors in the combination treatment groups showed an even steeper decrease of up to 75% compared to controls. We next set out to investigate if anti-VEGFR2 therapies enhance HER2 inhibitors ability to suppress signaling, and found that after three days of treatment with lapatinib (but not trastuzumab) a decrease in phosphorylation of the HER2/AKT/ERK pathway was induced. Another known trait of trastuzumab is its antibody-dependent cell cytotoxity (ADCC), mediated by natural killer (NK) cells[41]. Nevertheless, we did not find significant changes in primary or metastatic tumor growth, between any of the different treatment groups, for wild type mice compared to genetically or chemically NK-depleted mice.

Taken together, the enhanced benefit of the anti-HER2 and anti-VGEFR2 combination therapy is not primarily due to enhanced inhibition of HER2 activity, increased NK cell-mediated cytotoxicity, or direct cytotoxicity, but is a result of the antiangiogenic effect of VEGF. Finally, it is important to mention that in contrast to what is observed after anti-VEGF therapy in primary brain tumors, anti-VEGF treatment of breast cancer in the brain does not result in an increased invasive phenotype[42]. This could be because BT474 cells are not invasive in nude mice, not even in the primary setting, which maybe just attributable to this particular breast cancer cell line. To address this issue, future studies should investigate the invasiveness of more aggressive breast cancer cell lines when growing in the brain microenvironment after anti-VEGF therapy. Alternatively, this lack of invasiveness in response to anti-VEGF therapy could be because breast cancer cells do not further disseminate after colonizing the brain, even in a hypoxic environment. If so, this might be due to local cues in the brain microenvironment. Tracking the dissemination of breast cancer cells after growth in the brain would address this hypothesis.

VI *Can recovery of vascular function in glioblastoma improve outcome?*

Recent clinical trials of anti-vascular endothelial growth factor (VEGF) agents for glioblastoma show promising progression-free and overall survival rates. However, available clinical imaging does not separate antitumor effects from anti-permeability effects of these agents. Thus, although anti-VEGF agents may decrease tumor contrast-enhancement, vascularity, and vasogenic cerebral edema, the mechanisms leading to improved survival in patients remain incompletely understood. We addressed these studies in the work described in **chapter 7**. GFP-expressing U87, U118 (both murine), and CNS1 (a highly invasive rat glioma) tumors were orthotopically grown into the cerebral cortex of nude mice bearing cranial windows. Cediranib treatment did improve outcome in all tumor models, even though tumor growth was not affected by the dose used. As a result of longer survival without a delay in tumor growth, at the endpoint treated mice had tumors twice the size of the untreated ones. In previous preclinical studies cerebral physiology was found to be hypersensitive to increase in water content[43-45]. A major contributor to this edema is increased vascular permeability and accumulation of inflammatory (myeloid) cells. Cediranib inhibits both VEGFR2 and VEGFR1 signaling[46, 47]. To confirm that the survival benefits seen in our models are primarily due to the alleviation of cerebral edema by cediranib, brain edema was measured directly by the dry/wet weight ratio of the mouse brain *ex vivo*, and indirectly using MRI-T2 maps *in vivo*. Tumor water content decreased significantly at day 2 of treatment, but this effect was transient, reverting to control levels at day 8 through 11, suggesting that cediranib could no longer control cerebral edema caused by the tumor enlargement at later time points. Interestingly though, was the finding that dexamethasone, a corticosteroid used to relieve brain edema in glioma patients, could mimic these results to some extent, suggesting an additional mechanism of benefit for cediranib. In conclusion, anti-VEGF agents may be able to improve survival of patients with glioblastoma, even without inhibiting tumor growth. Building on these results, we suggest experiments to evaluate combination therapy of dexamethasone with cediranib to further prevent adverse effects of brain edema. Next, the antiedema effects of cediranib observed in our study raise the possibility that anti-VEGF therapies might prove beneficial for vasogenic brain edema secondary to

primary and metastatic brain tumors or other neurological diseases. Lastly, although the antiedema effects described in this study were transient, the vascular normalization window induced by anti-VEGF therapeutics may enhance the sensitivity of tumors to the cytotoxic effects of ionizing radiation and chemotherapy by a number of potential mechanisms [48-51]. This has led to the design of two recently published phase III clinical trials of bevacizumab with chemoradiation in glioblastoma [AVAglio study and Radiation Therapy Oncology Group (RTOG 0825 trial] [52, 53]. These nearly identical trials address the clinical benefit of addition of bevacizumab to the best standard treatment (radiotherapy and temozolomide) of primary glioblastoma and show a 3-4 month prolongation of progression free survival, but no effect on overall survival. Of interest is the discrepancy in findings where the AVAglio trial showed improvement in quality of life and performance status, in contrast to the RTOG 0825 trial that showed a worsening of quality of life and a decline in cognitive function. Unfortunately, the addition of bevacizumab to standard therapy in primary glioblastoma, has not led to an improvement of overall survival. Future trials exploring its activity in combination with newer agents targeted against the cancer cells or activating the immune system might be more beneficial.

VII *By which structural and functional changes does antiangiogenic therapy control edema?*

In patients with glioblastoma, postcontrast MRI shows that cediranib significantly decreases Ktrans a parameter dependent on vascular permeability. In **chapter 7**, we were able to mimic these results in a xenograft model. Intravital microscopy measurements demonstrated that cediranib significantly improves tumor vascular normalization, reflected as a decrease in tumor vessel permeability and diameter, as well as vascular hemoconcentration. However, cediranib-mediated vascular normalization was limited to a time window after which most of the functional and morphologic vascular parameters reverted to the abnormal phenotype. Specifically, at later time points, most normalization parameters such as vascular permeability, vessel diameter, basement membrane thickness, and hemoconcentration reversed, except for pericyte

proximity. At these late time points, cediranib treatment did decrease microvascular density in the center of the tumors, which was associated with a modest but significant increase in tumor cell apoptosis and a decrease in tumor cell proliferation. However, the ratio of proliferating to apoptotic tumor cells remained high, explaining the sustained tumor growth rate.

Earlier studies report that accumulation of inflammatory cells may be involved in the escape from vascular normalization. Granulocyte colony-stimulating factor (G-CSF) may promote tumor angiogenesis through a Bv8-dependent pathway that bypasses VEGF and renders tumors refractory to anti-VEGF therapy [54]. Our immunohistochemical analyses showed that cediranib significantly reduced macrophage infiltration at early time points, an effect that might be due to direct VEGFR1 blockade by cediranib and/or could be secondary to normalization of the tumor vessels and environment. However, infiltration of macrophages as well as other myeloid cells significantly increased at later time points during cediranib treatment. Future studies, designed to block the myeloid derived angiogenic pathway are needed to give more insight and possible targets to prevent escape from vascular normalization.

Finally, (pre)clinical studies have suggested that antiangiogenic therapy exerts systemic effects, causing elevation in multiple circulating angiogenic markers, such as interleukin-8, angiopoitins, and basic fibroblast growth factor, which leads to escape from vascular normalization and can promote tumor growth [47, 55-57]. In mice with U87 gliomas, we found that cediranib significantly increased the plasma levels of both mouse and human (tumor-derived) placenta growth factor and human VEGF but not mouse VEGF. Cediranib also rapidly increased the number of circulating CXCR4+ CD45+ cells. Future studies should establish whether activation of systemic inflammatory and/or angiogenic markers are causally related to the persistent growth of gliomas through antiangiogenic treatment. It would be of interest to examine the benefit of complementary anti-angiogenic therapies targeted at alternative proangiogenic pathways and elucidate the role of systemic effects of cediranib, both in experimental and clinical models.

References

1. DeVita VT, Jr. The evolution of therapeutic research in cancer. *N Engl J Med.* Apr 20 1978;298(16):907-910.

2. Duyverman AM, Kohno M, Duda DG, Jain RK, Fukumura D. A transient parabiosis skin transplantation model in mice. *Nat Protoc.* Apr 2012;7(4):763-770.

3. Duyverman AM, Kohno M, Roberge S, Fukumura D, Duda DG, Jain RK. An isolated tumor perfusion model in mice. *Nat Protoc.* Apr 2012;7(4):749-755.

4. Duyverman AM, Steller EJ, Fukumura D, Jain RK, Duda DG. Studying primary tumor-associated fibroblast involvement in cancer metastasis in mice. *Nat Protoc.* Apr 2012;7(4):756-762.

5. Zhang Y, Huang SZ, Wang S, Zeng YT. Development of an HSV-tk transgenic mouse model for study of liver damage. *FEBS J.* May 2005;272(9):2207-2215.

6. Tian B, Han L, Kleidon J, Henke C. An HSV-TK transgenic mouse model to evaluate elimination of fibroblasts for fibrosis therapy. *Am J Pathol.* Aug 2003;163(2):789-801.

7. Iwano M, Fischer A, Okada H, et al. Conditional abatement of tissue fibrosis using nucleoside analogs to selectively corrupt DNA replication in transgenic fibroblasts. *Mol Ther.* Feb 2001;3(2):149-159.

8. Condeelis J, Pollard JW. Macrophages: obligate partners for tumor cell migration, invasion, and metastasis. *Cell.* Jan 27 2006;124(2):263-266.

9. Fidler IJ. The pathogenesis of cancer metastasis: the 'seed and soil' hypothesis revisited. *Nat Rev Cancer.* Jun 2003;3(6):453-458.

10. Liotta LA, Kohn EC. The microenvironment of the tumour-host interface. *Nature.* May 17 2001;411(6835):375-379.

11. Paget S. The distribution of secondary growths in cancer of the breast. *Lancet.* 1889;1:571-573.

12. Hiratsuka S, Nakamura K, Iwai S, et al. MMP9 induction by vascular endothelial growth factor receptor-1 is involved in lung-specific metastasis. *Cancer Cell.* Oct 2002;2(4):289-300.

13. Kaplan RN, Riba RD, Zacharoulis S, et al. VEGFR1-positive haematopoietic bone marrow progenitors initiate the pre-metastatic niche. *Nature.* Dec 8 2005;438(7069):820-827.

14. Kim S, Takahashi H, Lin WW, et al. Carcinoma-produced factors activate myeloid cells through TLR2 to stimulate metastasis. *Nature.* Jan 1 2009;457(7225):102-106.

15. Podsypanina K, Du YC, Jechlinger M, Beverly LJ, Hambardzumyan D, Varmus H. Seeding and propagation of untransformed mouse mammary cells in the lung. *Science.* Sep 26 2008;321(5897):1841-1844.

16. Al-Mehdi AB, Tozawa K, Fisher AB, Shientag L, Lee A, Muschel RJ. Intravascular origin of metastasis from the proliferation of endothelium-attached tumor cells: a new model for metastasis. *Nat Med.* Jan 2000;6(1):100-102.

17. Yu M, Bardia A, Wittner BS, et al. Circulating breast tumor cells exhibit dynamic changes in epithelial and mesenchymal composition. *Science.* Feb 1 2013;339(6119):580-584.

18. Hale MD, Hayden JD, Grabsch HI. Tumour-microenvironment interactions: role of tumour stroma and proteins produced by cancer-associated fibroblasts in chemotherapy response. *Cell Oncol (Dordr).* Apr 2013;36(2):95-112.

19. Chen Y, Huang Y, Reiberger T, et al. Differential effects of sorafenib on liver versus tumor fibrosis mediated by stromal-derived factor 1 alpha/C-X-C receptor type 4 axis and myeloid differentiation antigen-positive myeloid cell infiltration in mice. *Hepatology.* Apr 2014;59(4):1435-1447.

20. Brennen WN, Rosen DM, Wang H, Isaacs JT, Denmeade SR. Targeting carcinoma-associated fibroblasts within the tumor stroma with a fibroblast activation protein-activated prodrug. *J Natl Cancer Inst.* Sep 5 2012;104(17):1320-1334.

21. Brennen WN, Isaacs JT, Denmeade SR. Rationale behind targeting fibroblast activation protein-expressing carcinoma-associated fibroblasts as a novel chemotherapeutic strategy. *Mol Cancer Ther.* Feb 2012;11(2):257-266.

22. Eke I, Cordes N. Focal adhesion signaling and therapy resistance in cancer. *Semin Cancer Biol.* Aug 10 2014.

23. Barnholtz-Sloan JS, Sloan AE, Davis FG, Vigneau FD, Lai P, Sawaya RE. Incidence proportions of brain metastases in patients diagnosed (1973 to 2001) in the Metropolitan Detroit Cancer Surveillance System. *J Clin Oncol.* Jul 15 2004;22(14):2865-2872.

24. Schouten LJ, Rutten J, Huveneers HA, Twijnstra A. Incidence of brain metastases in a cohort of patients with carcinoma of the breast, colon, kidney, and lung and melanoma. *Cancer.* May 15 2002;94(10):2698-2705.

25. Kienast Y, von Baumgarten L, Fuhrmann M, et al. Real-time imaging reveals the single steps of brain metastasis formation. *Nat Med.* Jan 2010;16(1):116-122.

26. Lorger M, Felding-Habermann B. Capturing changes in the brain microenvironment during initial steps of breast cancer brain metastasis. *Am J Pathol.* Jun 2010;176(6):2958-2971.

27. Duda DG, Duyverman AM, Kohno M, et al. Malignant cells facilitate lung metastasis by bringing their own soil. *Proc Natl Acad Sci U S A.* Nov 22 2010.

28. Bullitt E, Zeng D, Gerig G, et al. Vessel tortuosity and brain tumor malignancy: a blinded study. *Acad Radiol.* Oct 2005;12(10):1232-1240.

29. Izumi Y, Xu L, di Tomaso E, Fukumura D, Jain RK. Tumor biology - Herceptin acts as an anti-angiogenic cocktail. *Nature.* Mar 21 2002;416(6878):279-280.

30. Yuan F, Salehi HA, Boucher Y, Vasthare US, Tuma RF, Jain RK. Vascular permeability and microcirculation of gliomas and mammary carcinomas transplanted in rat and mouse cranial windows. *Cancer Res.* Sep 1 1994;54(17):4564-4568.

31. Eichler AF, Chung E, Kodack DP, Loeffler JS, Fukumura D, Jain RK. The biology of brain metastases-translation to new therapies. *Nat Rev Clin Oncol.* Jun 2011;8(6):344-356.

32. Chung E, Yamashita H, Au P, Tannous BA, Fukumura D, Jain RK. Secreted gaussia luciferase as a biomarker for monitoring tumor progression and treatment response of systemic metastases. *PLoS One.* 2009;4(12):e8316.

33. Martin M, Makhson A, Gligorov J, et al. Phase II study of bevacizumab in combination with trastuzumab and capecitabine as first-line treatment for HER-2-positive locally recurrent or metastatic breast cancer. *Oncologist.* 2012;17(4):469-475.

34. Besse B, Lasserre SF, Compton P, Huang J, Augustus S, Rohr UP. Bevacizumab safety in patients with central nervous system metastases. *Clin Cancer Res.* Jan 1 2010;16(1):269-278.

35. De Braganca KC, Janjigian YY, Azzoli CG, et al. Efficacy and safety of bevacizumab in active brain metastases from non-small cell lung cancer. *J Neurooncol.* Dec 2010;100(3):443-447.

36. Socinski MA, Langer CJ, Huang JE, et al. Safety of bevacizumab in patients with non-small-cell lung cancer and brain metastases. *J Clin Oncol.* Nov 1 2009;27(31):5255-5261.

37. Xia W, Gerard CM, Liu L, Baudson NM, Ory TL, Spector NL. Combining lapatinib (GW572016), a small molecule inhibitor of ErbB1 and ErbB2 tyrosine kinases, with therapeutic anti-ErbB2 antibodies enhances apoptosis of ErbB2-overexpressing breast cancer cells. *Oncogene.* Sep 15 2005;24(41):6213-6221.

38. Garrett JT, Olivares MG, Rinehart C, et al. Transcriptional and posttranslational up-regulation of HER3 (ErbB3) compensates for inhibition of the HER2 tyrosine kinase. *Proc Natl Acad Sci U S A.* Mar 22 2011;108(12):5021-5026.

39. Blackwell KL, Burstein HJ, Storniolo AM, et al. Overall survival benefit with lapatinib in combination with trastuzumab for patients with human epidermal growth factor receptor 2-positive metastatic breast cancer: final results from the EGF104900 Study. *J Clin Oncol.* Jul 20 2012;30(21):2585-2592.

40. Guarneri V, Frassoldati A, Bottini A, et al. Preoperative chemotherapy plus trastuzumab, lapatinib, or both in human epidermal growth factor receptor 2-positive operable breast cancer: results of the randomized phase II CHER-LOB study. *J Clin Oncol.* Jun 1 2012;30(16):1989-1995.

41. Spector NL, Blackwell KL. Understanding the mechanisms behind trastuzumab therapy for human epidermal growth factor receptor 2-positive breast cancer. *J Clin Oncol.* Dec 1 2009;27(34):5838-5847.

42. Carmeliet P, Jain RK. Molecular mechanisms and clinical applications of angiogenesis. *Nature.* May 19 2011;473(7347):298-307.

43. Manley GT, Fujimura M, Ma T, et al. Aquaporin-4 deletion in mice reduces brain edema after acute water intoxication and ischemic stroke. *Nat Med.* Feb 2000;6(2):159-163.

44. Papadopoulos MC, Manley GT, Krishna S, Verkman AS. Aquaporin-4 facilitates reabsorption of excess fluid in vasogenic brain edema. *FASEB J.* Aug 2004;18(11):1291-1293.

45. Thiagarajah JR, Papadopoulos MC, Verkman AS. Noninvasive early detection of brain edema in mice by near-infrared light scattering. *J Neurosci Res.* Apr 15 2005;80(2):293-299.

46. Dvorak HF. Vascular permeability factor/vascular endothelial growth factor: a critical cytokine in tumor angiogenesis and a potential target for diagnosis and therapy. *Journal of Clinical Oncology.* Nov 1 2002;20(21):4368-4380.

47. Fischer C, Jonckx B, Mazzone M, et al. Anti-PlGF inhibits growth of VEGF(R)-inhibitor-resistant tumors without affecting healthy vessels. *Cell.* Nov 2 2007;131(3):463-475.

48. Jain RK. Normalization of tumor vasculature: an emerging concept in antiangiogenic therapy. *Science.* Jan 7 2005;307(5706):58-62.

49. Padera TP, Kuo AH, Hoshida T, et al. Differential response of primary tumor versus lymphatic metastasis to VEGFR-2 and VEGFR-3 kinase inhibitors cediranib and vandetanib. *Mol Cancer Ther.* Aug 2008;7(8):2272-2279.

50. Wedge SR, Kendrew J, Hennequin LF, et al. AZD2171: a highly potent, orally bioavailable, vascular endothelial growth factor receptor-2 tyrosine kinase inhibitor for the treatment of cancer. *Cancer Res.* May 15 2005;65(10):4389-4400.

51. Winkler F, Kozin SV, Tong RT, et al. Kinetics of vascular normalization by VEGFR2 blockade governs brain tumor response to radiation: role of oxygenation, angiopoietin-1, and matrix metalloproteinases. *Cancer Cell.* Dec 2004;6(6):553-563.

52. Chinot OL, Wick W, Mason W, et al. Bevacizumab plus radiotherapy-temozolomide for newly diagnosed glioblastoma. *N Engl J Med.* Feb 20 2014;370(8):709-722.

53. Gilbert MR, Dignam JJ, Armstrong TS, et al. A randomized trial of bevacizumab for newly diagnosed glioblastoma. *N Engl J Med.* Feb 20 2014;370(8):699-708.

54. Shojaei F, Ferrara N. Refractoriness to antivascular endothelial growth factor treatment: role of myeloid cells. *Cancer Res.* Jul 15 2008;68(14):5501-5504.

55. Batchelor TT, Sorensen AG, di Tomaso E, et al. AZD2171, a pan-VEGF receptor tyrosine kinase inhibitor, normalizes tumor vasculature and alleviates edema in glioblastoma patients. *Cancer Cell.* Jan 2007;11(1):83-95.

56. Ebos JM, Lee CR, Christensen JG, Mutsaers AJ, Kerbel RS. Multiple circulating proangiogenic factors induced by sunitinib malate are tumor-independent and correlate with antitumor efficacy. *Proc Natl Acad Sci U S A.* Oct 23 2007;104(43):17069-17074.

57. Shaked Y, Henke E, Roodhart JM, et al. Rapid chemotherapy-induced acute endothelial progenitor cell mobilization: implications for antiangiogenic drugs as chemosensitizing agents. *Cancer Cell.* Sep 9 2008;14(3):263-273.

Chapter 9

Conclusions and future perspectives

Conclusions

Based on the findings presented in this thesis, the following conclusions may be drawn:

Part two:

I The described, novel, animal models facilitate analysis of microenvironmental involvement in the metastatic process.

II Host stromal cell shed from primary tumors as heterotypic fragments, survive within the circulation and proliferate at the distant site, all while increasing metastatic potential of tumor cells.

Part two:

III Consistent with reports from the clinic, in our preclinical model, HER2+ brain metastases are refractory to anti-HER2 targeted therapies.

IV The addition of an anti-VEGFR2 antibody to HER2 targeted therapies significantly improves outcome.

V Antiangiogenic therapy induces a transient vascular normalization and reduces macrophage infiltration at early time points.

VI Transient recovery of vascular function in glioblastoma improves outcome.

VII Anti-VEGF treatment decreases edema by normalizing tumor vasculature, increasing survival in a preclinical model.

Future perspectives

The studies presented in part one of this thesis add new means to the role of the tumors microenvironment, specifically fibroblasts, in metastasis formation. The field of cancer research has made incredible progress over the last 40 years, but in spite of this, relatively little progress has been made in preventing the disease and to treat it. Still most of the anticancer treatments in wide use today are developed prior to 1975, when very little was known about genetic and biochemical mechanisms of cancer pathogenesis.

It has become clear, that the current classification of cancers, is of limited utility. Identification of subgroups of patients, using molecular markers would allow clinicians to stratify cancers and favor tailored therapies and possibly increase drug response rates. Gene expression arrays and subsequent computer analysis using bioinformatics could be further optimized by laser capture microdissection. This technique enables to physically isolate epithelial cells from stromal cells present in a carcinoma sample. This allows separate analyses of the gene expression patterns of these groups, enabling further refinement and potentially greater accuracy in stratification of tumors.

Chapter 10

Nederlandse samenvatting

Meer dan honderd jaar geleden introduceerde Stephen Paget de hypothese dat tumor cellen – de zaadjes – alleen konden groeien op een secundaire plek – de bodem – als er sprake was van een gunstig milieu. Tegenwoordig begrijpen we dat er sprake is van een continue uitwisseling van signalen tussen de tumor en zijn omgeving, zowel op de plek van de oorspronkelijke tumor, alswel in de uitzaaiingen. Gedurende tientallen jaren heeft het kanker onderzoek zich gefocust op kanker cellen en hun genetische veranderingen in de initiële fase van tumor vorming. Deze veranderingen leiden tot een verhoogde celdeling, resistentie voor signalen die de groei remmen en geprogrammeerde celdood en de verhoogde aanmaak van bloedvaten die de groeiende tumor moeten voorzien van voedingsstoffen. Aan het einde van de vorige eeuw werd het duidelijk dat de groei van tumoren en metastasen afhankelijk is van deze genetische veranderingen, maar ook van de micro-omgeving van de kankercellen. Hiermee verschoof het perspectief en werden tumoren gezien als kleine organen, waar abnormale kankercellen groeien in een complexe matrix waarin ze ondersteund worden door lichaamseigen cellen – het stroma. Vandaag de dag is het bekend dat deze stroma cellen, die in sommige tumoren wel 90% van het totale volume innemen, een actieve en essentiele bijdrage leveren aan de tumor massa. Ze worden door de tumor cellen gerekruteerd uit het omliggende weefsel of uit de bloedstroom en worden gebruikt door de tumor voor zijn groei. De rol van deze stroma cellen bij het uitzaaien van tumoren is echter nog onbekend en in dit proefschrift focussen we op dit proces.

Deel I

Het ontwikkelen van een set diermodellen die de verschillende stappen van uitzaaiende tumorcellen nabootsen en waarmee we de stroma cellen kunnen visualiseren.

De meerderheid van de kankerpatiënten overlijdt uiteindelijk aan de gevolgen van de uitzaaiingen (metastasen) van de tumor. Het proces van uitzaaien beslaat een serie van opeenvolgende stappen, welke de kankercellen allemaal moeten voltooien om uiteindelijk op de secundaire plaats te kunnen uitgroeien. Kwaadaardige cellen hebben een ongecontroleerde celgroei, wat leidt tot de ontwikkeling van een tumor. Wanneer tumoren groter worden dan 1-2 mm moeten ze nieuwe bloedvaatjes vormen om zo

voorzien te worden van zuurstof en voeding. Vervolgens worden tumoren invasief, waarbij ze door de normale weefselgrenzen breken en tumorcellen of fragmenten los raken en in de bloedstroom terecht komen en getransporteerd worden naar andere organen. Daar aangekomen, treden ze uit de bloedvaten en groeien ze in een nieuwe omgeving uit tot metastasen. Gedurende deze reis moeten ze het afweersysteem van het lichaam omzeilen.

In de **hoofdstukken 2-4** worden drie nieuwe muismodellen gepresenteerd waarmee de verschillende stappen kunnen nabootsen. In **hoofdstuk 2** beschrijven we een model waarbij we een groot stuk huid van een genetisch gemanipuleerde muis transplanteren naar een normale – wild type – muis. Alle (stroma) cellen in het getransplanteerde stuk huid zijn gelabeld met een groen fluorescent eiwit. De tumor cellen (rood-gelabeld) die we in dit huidtransplantaat lieten groeien rekruteerde vervolgens de groene cellen uit hun omgeving. Spontane metastasen vanuit dit huidtransplantaat naar de longen konden vervolgens met behulp van een geavanceerde 'multiphoton' lasermicroscoop zichtbaar worden gemaakt. In **hoofdstuk 3** presenteren we een diermodel waarin we alle cellen die door de tumor aan de bloedbaan worden afgegeven kunnen analyseren. Hiervoor gebruikten we genetisch gemodificeerde muizen met groen-gelabelde cellen. In de – groene – nieren van deze muizen implanteerden we vervolgens rood gelabelde tumor cellen. Na enkele weken brachten we een canule in het afvoerende bloedvat van de nier in, waardoor we alle cellen en fragmenten die in de circulatie terecht komen op konden vangen en verder konden bestuderen (hoofdstuk 5). **Hoofdstuk 4** beschrijft een nieuw model waarin de interactie tussen tumor en stroma cellen kan worden bestudeerd. Hiervoor isoleerden we stoma cellen (carcinoma-geassocieerde-fibroblasten (CAFs)) uit menselijk borsttumor weefsel die we samen met kankercellen afkomstig van muizen implanteerden in een muismodel. Door middel van het difterie toxine, welke menselijke cellen uitschakelt, maar waarvoor muis cellen ongevoelig zijn, kunnen we vervolgens de rol van stroma tijdens het uitzaaien onderzoeken.

Zijn stroma cellen aanwezig in alle stappen van het metastaseringsproces en beïnvloeden zij de vorming van uitzaaiingen?

Het is bekend dat metastasen een voorkeur hebben om uit te groeien op voorkeurslocaties waar er sprake is van een ontvankelijk milieu. Onderzoek laat zien dat tumor cellen het milieu op de secundaire locatie ook zelf kunnen beïnvloeden, onder andere door het uitscheiden van factoren waarbij er een pre-metastatische niche wordt gecreëerd. In **hoofdstuk 5** laten we zien dat tumor cellen hun eigen stroma cellen kunnen meenemen tijdens het uitzaaien en zo zorgen voor een tijdelijke gunstige micro-omgeving. Met behulp van het eerder beschreven tumor perfusie model vingen we alle cellen die vanuit een niertumor in de bloedbaan kwamen op. Analyse met de microscoop liet zien dat alle grote fragmenten stroma cellen bevatten en dat deze fragmenten minder celdood lieten zien dan tumor cellen alleen. Wanneer we deze fragmenten injecteren in een andere muis, zien we dat de stroma cellen aanwezig zijn met de tumor cellen op de plek van de metastase en daar ook delen. Om deze lichaameigen cellen te karakteriseren gebruikten we het huid transplantatie model. Rode tumorcellen groeiden in de groene huidtransplantaten en rekruteerden groene stroma cellen. Na enkele weken zaaiden deze tumoren uit naar de longen, waar we rood-groene metastasen zagen. Met behulp van immunohistochemische kleuringen konden we deze cellen identificeren als fibroblasten. Nu we wisten dat deze fibroblasten samen met de tumorcellen alle stappen van het metastatische proces doorlopen was het belangrijk om te weten of dit ook van belang is voor de efficiëntie van dit proces. Hiervoor gebruikten we het laatst beschreven model waar we menselijke cellen samen met muis-tumor celle lieten uitzaaien en bij de helft van deze groep de menselijke fibroblasten uitschakelden met difterie toxine. Zoals verwacht ontwikkelden de muizen waarbij de stroma cellen aanwezig waren meer uitzaaiingen en leefden ze korter.

Deel II

Is de bloed-hersenbarrière van invloed op therapieën gericht op HER-2 bij de behandeling van hersenmetastasen van borsttumoren?

De bloed-hersenbarrière (BBB) beschrijft de speciale structuur van bloedvaten in de hersenen. Strakke verbindingen tussen de cellen zorgen ervoor dat moleculen niet van de bloedbaan de hersenen in kunnen lekken, maar door de cellen getransporteerd moeten

worden. Het beschermd de hersenen tegen ongewenste indringers, maar is tevens een groot obstakel voor de aflevering van geneesmiddelen. Wanneer hersenmetastasen groeien maken ze nieuwe 'inferieure' bloedvaten, welke de BBB aantasten, deze schade aan de barrière is echter heterogeen en de toevoer van geneesmiddelen kan hierdoor nog steeds beperkt zijn.

Ongeveer 20-30% van de humane borstkankers bezitten de Human epithelial growth factor receptor 2 (HER-2). Deze specifieke tumoren staan bekend om hun agressiviteit en vermogen om uit te zaaien, wat gepaard gaat met een slechte overlevingskans. Herceptin en lapatinib zijn beiden geneesmiddelen die de werking van de HER-2 receptor uitschakelen, ondanks de goede resultaten met betrekking tot de behandeling van primaire tumoren en metastasen in het lichaam, is de werking bij hersenmetastasen zeer beperkt.

Kan het toevoegen van een angiogenese remmer de behandeling verbeteren?

De vorming van nieuwe bloedvaten (angiogenese) speelt een belangrijke rol in tumor groei en progressie. Angiogenese vindt normaal plaats als een goed gereguleerd proces, bijvoorbeeld tijdens de embryogenese, wondheling en zwangerschap. In tumoren is de angiogenese ongereguleerd, wat resulteert in bloedvaten die qua structuur en functie abnormaal zijn. Angiogenese remmers, zoals bevacizumab, kunnen deze abnormale bloedvaten tijdelijk normalizeren.

Het gebruik van een angiogenese remmer in combinatie met herceptin en chemotherapie heeft een gunstig effect getoond in de behandeling van HER2-positieve borstkanker patiënten met systemische uitzaaiingen in een fase II trial. Patiënten met hersenmetastasen waren echter uitgesloten van deze studie vanwege het vermeende gevaar op hersenbloedingen. Inmiddels blijkt dit risico erg klein. In **hoofdstuk 5**, bestuderen we het effect van een (muis) angiogenese remmer (DC101) in combinatie met herceptin of lapatinib. Waar alle drie de monotherapieën de overleving van muizen met slechts enkele dagen verlengde, zorgde de combinatie van DC101 met herceptin of lapatinib voor een verdrievoudiging van de overleving. Nog opmerkelijker was het effect van een combinatie therapie met herceptin, lapatinib en DC101, welke resulteerde in een toename van de overleving die vijf maal zo groot was als in de controle groep. Deze

resultaten bieden aanknopingspunten voor de ontwikkeling van angiogenese remmers voor de behandeling van patiënten met HER2 positieve borstkanker met hersenmetastasen.

Welke mechanismen dragen bij aan het antitumor effect van een angiogenese remmer in combinatie met HER2 remmers?

In **hoofdstuk 6** onderzoeken we met behulp van immunohistochemische analyses de mechanismen die verantwoordelijk zijn voor de goede resultaten van de triple therapy. Hieruit blijkt dat de anti-vasculaire effecten van deze combinatie tumor necrose induceren en zo de tumor groei remmen en de overleving verlengen.

Kan de verbetering van de functie van de bloedvaten bij de behandeling van glioblastomen de overleving verlengen?

Bij volwassenen is het glioom de meest voorkomende primaire hersentumor. De ruimte innemende werking van zowel de tumor en de zwelling van de hersenen leiden tot een slechte prognose en de 5-jaars overleving is kleiner dan 5%. De huidige therapie bestaat uit chirurgische verwijdering van de tumor, gevolgd door bestraling en chemotherapie, maar levert helaas maar een levenswinst van 2.5 maand op. Recente klinische onderzoeken met angiogeneseremmers bij de behandeling van glioblastomen laten een verbetering van de overleving zien. Het is echter onbekend of dit het gevolg is van een anti-tumor effect of van het verminderen van de zwelling van de hersenen. In **hoofdstuk 7** focussen we op de behandeling van gliomen met een angiogeneseremmer in muizen. Met behulp van een glasplaatje in de schedel van een muis is het mogelijk de tumorgroei tijdens de behandeling te monitoren en zien we dat de behandeling de tumorgroei niet beïnvloedt, maar wel zorgt voor een verlengde overleving door het drastisch verminderen van de zwelling van de hersenen.

Door welke structurele en functionele veranderingen verminderd een angiogeneseremmer de zwelling van de hersenen?

In **hoofdstuk 7** bestuderen we met behulp van de intravitale microscoop de structurele en functionele veranderingen van de bloedvaatjes in de hersenen tijdens de behandeling met angiogeneseremmers en zien we dat de diameter kleiner wordt en er minder vloeistof uit de vaatjes kan lekken.

Chapter 11

Dankwoord

Dit proefschrift is tot stand gekomen met de hulp en steun van velen, waarvoor heel veel dank! Graag wil ik een aantal personen in het bijzonder danken.

Prof Dr. I.H.M. Borel Rinkes, beste Inne,
Via Prof. Chr. van der Werken stond ik lang geleden voor je bureau, om te vragen of ik onderzoek voor je kon doen, in Boston. Nadat ik de eerste stappen in het basale onderzoek in jouw lab tijdens mijn onderzoeksstage had gezet, introduceerde je me in het Steele Lab en daar ging ik! Niet gehinderd door enige ervaring in het opzetten van projecten of kennis van de broodnodige technieken. Vanaf de zijlijn heb je me al die tijd gevolgd en gesteund als dat weer eens nodig was. Bedankt voor het jarenlange vertrouwen, gelukkig heb jij (als enige..) nooit getwijfeld dat dit proefschrift af zou komen. Het is ongelofelijk hoe je tijdens onze afspraken het voor elkaar krijgt binnen zo'n korte tijd de onderste stenen boven te krijgen, zowel inhoudelijk als privé. Je positieve instelling is een voorbeeld, ik hoop dat we dit kunnen voortzetten in de kliniek!

Dr. Dan. G. Duda, dear Dan,
You are definitely my guide in basic research! It has been a pleasure to work with you on some of your innumerable ideas. Your knowledge of the research in our field and beyond is incredible. I think we have developed a set of animal models that will last for many years. I admire your dedication and optimism, it has not always been an easy road to publication, but your enthusiasm has definitely helped along the way. It's great that you are travelling to Utrecht to attend my defense ceremony, thank you!

De leden van de promotiecommissie,
Prof. Dr. van Diest, Prof. dr. Voest, Prof. dr. van Rheenen, Prof. dr. Ruers, Dr. Kranenburg, Dank voor de interesse in mijn onderzoek en het zitting nemen in de oppositie.

Prof. Dr. R.K. Jain, dear Rakesh,
Thank you for the great time in your lab. It is incredible how you run a big lab, with so many different people and still have an eye for every individual, scientifically but definitely also in a personal matter. You've created an environment that is inspirational, challenging, and extremely productive, but still feels like one big family.

Dr. P. Huang, Dear Peigen,

The animal facility that you've created is absolutely amazing. I remember the times that I had to ask you for way too many animals on a short notice. I don't know how you bread all these special strains overnight, but you always managed to get them! Thank you so much for all your help.

Dr. Mitsutomo Kohno, dear Tomo,

We have only worked together for one week, but I think it has been my most productive week in a research lab. You taught me all your surgical skills including the parabiosis model, not the easiest one for a starter! You patience is endless and your animal model heritage a perfect start for a new fellow.

Sylvie Roberge and Julia Kahn,

It's extremely valuable to have some stable factors in a lab that changes personnel so commonly. You taught me many of the basic lab skills, without giving me the feeling that I should have known. Thank you so much for your support with the animal work. Thinking of the endless hours we spend working (and chatting) in the hood makes me smile!

Phyllis McNally,

From the first day I saw you on one of my visits to Boston, it was clear that you run the lab at COX . Thank you for all your advice, directions, and support. But most of all for being there, to lighten up the days with your laughs, lunches, lab parties, and jokes. I will never forget your mean April fools joke, telling Walid and me that we had to move out of our office. It is not easy to get me irritated, but you definitely succeeded there!

COX white table, dear Dai, Tim, Walid, Angera, Johanna, Euiheon, Hiro, Joao, Christina, Vikash, Ryan, Phyllis, Julia, Sylvie, and Peigen

Lunch at the white table was the highlight of everyone's day. I have learned more about the world's traditions here then anywhere else. And who could think of any better place to eat a sandwich then between the centrifuge and the liquid nitrogen tanks!

Marielle Hoefakker en Romy Liesdek,
Bedankt voor jullie jarenlange hulp en ondersteuning en natuurlijk de ontelbare aanbevelingsbrieven die jullie elke keer weer op tijd wisten te sturen! Jullie zijn de lifeline voor onderzoekers in het buitenland.

Ernst Steller en Lotte Hiddingh,
Mijn student onderzoekers, wat was het een mooi avontuur in Boston. Het was heerlijk om van tijd tot tijd weer wat frisse moed en enthousiasme door de projecten te laten waaien! Jullie hebben mij ontzettend geholpen en daarnaast veel gezelligheid gebracht. **Ernst,** je was pas een paar dagen in het lab toen je met een chirurg uit MGH op de bank mocht zitten bij de Patriots en werkelijk iedereens mond openviel. Het was super om samen te werken en je lekker je gang te laten gaan. Ja baas, ik ga het regelen, was een van mijn favoriete uitspraken, voornamelijk omdat er dan veel tijd overbleef voor alle andere, zeer belangrijke zaken buiten het lab. **Lotte,** de juiste persoon op de juiste plek! Wat was het fijn dat jij er was toen mijn projecten zich opeens verplaatsten van het dierenlab in COX, naar het cell biology lab in CNY. Jij wist precies hoe je alle kleuringen en PCRs moest doen en dat met een gedrevenheid die onvoorstelbaar is. Je hebt na Boston je plek gevonden in het Wurdinger lab en promoveert vandaag ook, gefeliciteerd!

De Boston clan, Tom en Femke, Dimphna, Marike en Paul, Stephan, Ties, Stan, Marco en Sarah, de harde kern Nederlanders in Boston
Een stel Italianen in the North End 3 dozen met bitterballen laten bakken tijdens het EK was denk ik wel het hoogtepunt van ons patriotisme. Ondanks dat we natuurlijk allemaal heel veel Amerikaanse vrienden hadden, was er vaak een Nederlands onderonsje. Hockeyen in Acton, Oud en Nieuw in Peru, BBQ en poolparties in Weston, Thanksgiving dinners, NL borrel, koninginnendag van het consulaat en de skitripjes in New Hampshire, ik heb ervan genoten!

Eveline en Wilt Idema,
Een warm thuis ver van huis! Het begon met een bank en een bloemetje voor in ons lege nieuwe huis, maar al snel breidde jullie 'ouderlijke' zorg zich uit, wat hebben wij hiervan genoten. Gezellige lunches, etentjes en een weekend naar de Cape maakten dat wij ons snel thuis voelden in Belmont. Bedankt voor al jullie hulp.

Stafleden en arts-assistenten, chirurgie van het Jeroen Bosch Ziekenhuis, hartelijk dank voor jullie interesse in mijn onderzoek. Ondanks het basale karakter ervan, kon ik toch wel wat enthousiasme bespeuren bij het zoeken naar rode en groene cellen in mijn presentaties. Het is fijn dat jullie mij de tijd en ruimte hebben gegeven dit project af te ronden en tegelijkertijd de dokter in mij weer hebben wakker gemaakt.

Stafleden en arts-assistenten, afdeling Heelkunde van het UMC Utrecht**.** Ik ben er pas net, maar het beloofd een mooie tijd te worden!

JC Spijker,
Dank voor de interesse in mijn onderzoek, maar ook vooral de welkome afleiding daarvan. Ik ben de laatste in het rijtje, tijd voor een feestje!

Plomp 15,
't is het huis waar je in Utrecht in moet wonen! Naast al het dagelijks plezier ook altijd een plek waar werd geluisterd en waar menig levensles is geleerd. Bedankt voor alle gezelligheid die er nu jaren later ook nog steeds is!

Aline Panhan,
In the end, it's you who made this book possible. Taking care of the girls like your own children gave me the time and freedom to finally start writing this thesis. I admire your commitment and dedication to do things right. We wish you lots of love and happiness in your new life with Steven. See you soon!

Mijn paranimfen,
Anne Marie Geerts,
Samen begonnen we jaren geleden met geneeskunde, de een nog fanatieker dan de ander… Studeren en naar feestjes gaan ging soms naadloos in elkaar over, maar na een tijdje kregen we de smaak te pakken en kijk waar we nu staan! Het is heerlijk om jou als vriendin te hebben, iemand die zegt wat ik denk en er altijd maar weer is. Fijn dat je me als paranimf wil ondersteunen.

Willemijn van der Vlugt,
Koffie met een perfect gebakken eitje, dan heb je mij! Na jarenlange pret op de Plomp, ben je daarna ook altijd heel betrokken geweest bij mijn leven. Ik kan me geen trouwere en lievere vriendin wensen en dank je voor al je altijd luisterende oor en wijze raad. Dat je hier je geld mee zou gaan verdienen had misschien niemand 15 jaar geleden voorzien, maar de laatste jaren vallen alle puzzelstukjes op zijn plek! Dank je dat je nu naast me staat als paranimf.

De **Duyvermannen**,
Eindelijk iemand die ook promoveert binnen de familie, en dan is het de koude kant.. Bedankt voor jullie steun in good times and bad times.

Pappa, mamma en Marceline,
Door jullie opvoeding en steun heb ik geleerd om hard te werken, wat geleid heeft tot onder andere dit proefschrift. Bedankt voor alle mogelijkheden die jullie me altijd geboden hebben en natuurlijk jullie hulp met de meisjes, helemaal vanuit Maastricht.

Lieve **Lieve en Britt**,
Mam, schrijf je een boek, waarom? Waar gaat het boek over? Ga je het aan ons voorlezen als het af is? Zit je nou alweer te typen, ik vind jouw boek niet meer leuk..
Eindelijk is het af en is er weer meer tijd voor jullie! Of eruit zal voorgelezen worden betwijfel ik, maar we kunnen in ieder geval de plaatjes kijken.

Curriculum vitae

Annique Pieters was born on July 23rd, 1977 in Maastricht, the Netherlands. In 1995, she graduated from secondary school, the Sint Maartenscollege in Maastricht. After one year of studying French language and culture at the Université Paul Valery, Montpellier, France, and one year of studying Law and Psychology at Maastricht University, she started her medical training at Utrecht University. As a medical student, she was involved in two research projects at the department of Surgery in the Utrecht University Medical Center (Prof. dr. Ch. van de Werken en Prof. dr. I.H.M. Borel Rinkes). After graduating from medical school, she started working for Salude Medical Advise, before she moved to Boston, MA. In the Edwin L. Steele laboratory, (Massachusetts General Hospital and Harvard Medical School) she performed the research as described in this thesis. Her work has been awarded the 'Scholar in training' award at the AACR 101st Annual meeting, Washington DC and the 'poster of distinction award' at the Massachusetts General Hospital's 34th Annual SAC Poster Session. In 2006 she received a Pre-doctoral Research Fellowship from the U.S.A. Department of Defense, Breast Cancer Program. With pleasure she started her surgical training at the Jeroen Bosch Hospital (Dr. K. Bosscha) and the Utrecht University Medical Center (Prof. Dr. M.R. Vriens).

List of publications

Chen Y, Huang Y, Reiberger T, **Duyverman AM**, Huang P, Samuel R, Hiddingh L, Roberge S, Koppel C, Lauwers GY, Zhu AX, Jain RK, Duda DG. Differential effects of sorafenib on liver versus tumor fibrosis mediated by stromal-derived factor 1 alpha/C-X-C receptor type 4 axis and myeloid differentiatio antigen-positive myeloid cell infiltration in mice.
Hepatology 2014 Apr;59(4):1435-47

Kodack DP, Chung E, Yamashita H, Incio J, **Duyverman AM**, Song Y, Farrar CT, Huang Y, Ager E, Kamoun W, Goel S, Snuderl M, Lussiez A, Hiddingh L, Mahmood S, Tannous BA, Eichler AF, Fukumura D, Engelman JA, Jain RK.Combined targeting of HER2 and VEGFR2 for effective treatment of HER2-amplified breast cancer brain metastases.
Proceedings of the National Academy of Sciences 2012 Nov 6;109(45):E3119-27

Duyverman AM, Kohno M, Duda DG, Jain RK, Fukumura D. A transient parabiosis skin transplantation model in mice.
2012 Mar 22;7(4):763-70

Duyverman AM, Steller EJ, Fukumura D, Jain RK, Duda DG.v
Studying primary tumor-associated fibroblast involvement in cancer metastasis in mice.
Nature Protocols 2012 Mar 22;7(4):756-62

Duyverman AM, Kohno M, Roberge S, Fukumura D, Duda DG, Jain RK. An isolated tumor perfusion model in mice.
Nature Protocols 2012 Mar 22;7(4):749-55

Duyverman AM, Duda DG, Kohno M, Snuderl M, Steller EJ, Fukumura D, Jain RK
Malignant cells facilitate lung metastasis by bringing their own soil.
Proceedings of the National Academy of Sciences 2010 Dec 14;107(50):21677-82

Kamoun WS, Ley CD, Farrar CT, **Duyverman AM**, Lahdenranta J, Lacorre DA, Batchelor TT, di Tomaso E, Duda DG, Munn LL, Fukumura D, Sorensen AG, Jain RK.Edema control by cediranib, a vascular endothelial growth factor receptor-targeted kinase inhibitor, prolongs survival despite persistent brain tumor growth in mice.
Journal of Clinical Oncology 2009 May 20;27(15):2542-52

van der Bilt JD, Soeters ME, **Duyverman AM**, Nijkamp MW, Witteveen PO, van Diest PJ, Kranenburg O, Borel Rinkes IH. Perinecrotic hypoxia contributes to ischemia/reperfusion-accelerated outgrowth of colorectal micrometastases.
American Journal of Pathology 2007 Apr;170(4):1379-88

Heikens JT, **Pieters AM.** An uncommon cause of high defecation frequency after an ileal pouch-anal anastomosis.
Techniques in Coloproctology 2006 Jul;10(2):149-50.